

Controlling Wave Propagation Through Nonlinear Engineered Granular Systems

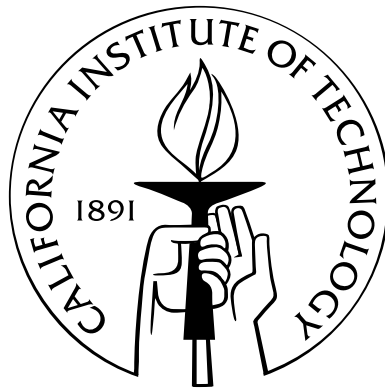
Thesis by

Andrea Leonard

In Partial Fulfillment of the Requirements

for the Degree of

Doctor of Philosophy



California Institute of Technology

Pasadena, California

2013

(Defended April 23, 2013)

Acknowledgements

I would like to first acknowledge and thank my advisor, Chiara Daraio. Her enthusiasm for science and research is infectious, and has been extremely motivating during the ups and downs of my thesis work. I will always be grateful for her openness, guidance, and support, which helped make my time as a graduate student a truly positive experience. I would also like to thank the other members of my thesis committee: Guruswami Ravichandran, Nadia Lapusta, and Dennis Kochmann.

I would like to thank my family. Mom, you are the best.

I thank my collaborators: Fernando Fraternali, Laurent Ponson, Christopher Chong, Panos Kevrekidis, and the MURI group at UIUC, especially John Lambros, Amnaya Aswathi, and Philippe Geubelle. Mythili, I greatly appreciate all your help with the 3D printing projects. I thank all the people in the Aero and Physics machine shops, and Jennifer Stevenson for her patience and help.

Thank you to my group of CE/AM graduate students who helped me survive my first year at Caltech. I would like to thank all of the past and present members of Professor Daraio's lab. I am grateful to have worked with such a diverse, collaborative, and encouraging group of people. A special thank you to all my friends and colleagues at Caltech that have gone through this journey with me and helped me come out sane on the other side. Also, thank you to the new friends I've made during my last few months at ETH.

A final thank you to the DOE SCGF program and the 2010 cohort.

Abstract

We study the fundamental dynamic behavior of a special class of ordered granular systems in order to design new, structured materials with unique physical properties. The dynamic properties of granular systems are dictated by the nonlinear, Hertzian, potential in compression and zero tensile strength resulting from the discrete material structure. Engineering the underlying particle arrangement of granular systems allows for unique dynamic properties, not observed in natural, disordered granular media. While extensive studies on 1D granular crystals have suggested their usefulness for a variety of engineering applications, considerably less attention has been given to higher-dimensional systems. The extension of these studies in higher dimensions could enable the discovery of richer physical phenomena not possible in 1D, such as spatial redirection and anisotropic energy trapping. We present experiments, numerical simulation (based on a discrete particle model), and in some cases theoretical predictions for several engineered granular systems, studying the effects of particle arrangement on the highly nonlinear transient wave propagation to develop means for controlling the wave propagation pathways. The first component of this thesis studies the stress wave propagation resulting from a localized impulsive loading for three different 2D particle lattice structures: square, centered square, and hexagonal granular crystals. We observe a wide range of propagating wave characteristics, with distinct properties inherent to each lattice structure: quasi-1D solitary wave propagation, fully 2D wave propagation with tunable wave front shapes, and 2D pulsed wave propagation. Additionally the effects of weak disorder, inevitably present in real granular systems, are investigated. The second half of this thesis studies the solitary wave propagation through 2D and 3D ordered networks of granular chains, reducing

the effective density compared to granular crystals by selectively placing waveguiding chains to control the acoustic wave transmission. The rapid wave front amplitude decay exhibited by these granular networks makes them highly attractive for impact mitigation applications. The agreement between experiments, numerical simulations, and applicable theoretical predictions validates the wave guiding capabilities of these engineered granular crystals and networks and opens a wide range of possibilities for the realization of increasingly complex granular material design.

Contents

Acknowledgements	ii
Abstract	iii
Contents	v
List of Figures	ix
List of Tables	xxviii
1 Introduction	1
1.1 Motivation and Significance	2
1.1.1 Choice of Granular Framework	3
1.2 Structured (Engineered) Granular Materials	5
1.2.1 1D Systems	5
1.2.1.1 Granular Protectors (and Other Applications)	8
1.2.2 2D & 3D Systems	9
1.2.2.1 Presence of Defects and Weak Disorder	11
1.3 Disordered (Natural) Granular Materials	12
1.4 Goals and Objectives	14
2 Methods	15
2.1 Nature of Stress Waves in Granular Media: Length and Time Scale Considerations	15
2.2 Experiments	16

2.2.1	Assembly of Granular Systems	17
2.2.2	Interior Measurements: Custom Fabricated Accelerometer Sensor Particles	18
2.2.3	Edge Measurements: Dynamic Load Cells	21
2.2.4	Discussion of Alternate Experimental Techniques	21
2.3	Numerical Simulations	22
2.3.1	Discrete Particle Model	23
2.3.1.1	Rotational and Dissipative Considerations	25
2.3.1.2	Weak Disorder Simulations	26
2.3.1.3	Additional Numerical Simulations	27
3	2D Granular Crystals: Square	28
3.1	Problem Description and Approach	28
3.2	Wave Propagation Path	30
3.2.1	Particle Velocity – Wave Speed Scaling Relation	36
3.2.2	Pulse Length	38
3.3	Summary of Results	41
4	2D Granular Crystals: Centered Square	42
4.1	Problem Description and Approach	42
4.2	Wave Propagation Path	45
4.2.1	Extended System Response	46
4.2.2	Experimental Results	48
4.2.3	Effects of Weak Disorder	53
4.2.4	Additional Numerical Study: Effects of Pre-Compression	62
4.3	Summary of Results	63
5	2D Granular Crystals: Hexagonal	66
5.1	Problem Description and Approach	66
5.2	Wave Propagation Path	68
5.2.1	Ternary Collision Approximation and Numerical Study	69

5.2.1.1	30° Angle of Observation	71
5.2.1.2	0° Angle of Observation	73
5.2.2	Experimental Results and Effects of Weak Disorder	73
5.3	Additional Numerical Study: Dimer	76
5.4	Summary of Results	78
6	Ordered Granular Network: 2D	81
6.1	Problem Description and Approach	81
6.2	Theoretical Approach: Quasi-Particle Theory	84
6.3	Wave Propagation Path	88
6.3.1	Central, Largest Leading Pulse	90
6.3.2	Spatial Repartition of Transmitted Leading Pulses	92
6.4	Discussion	95
6.5	Summary of Results	100
7	Ordered Granular Network: 3D	102
7.1	Problem Description and Approach	102
7.2	Theoretical Approach: Quasi-Particle Theory	104
7.3	Wave Propagation Path	107
7.3.1	Distribution of Leading Pulse Amplitudes: Effective Network Properties	109
7.4	Summary of Results	110
8	Conclusions & Future Work	113
8.1	Conclusions	113
8.2	Future Directions	115
	Bibliography	118
	Appendix A TCA Model	
	(and Corresponding Numerical Study)	137
A.1	Model	137

A.2 Ternary Collision Approximation: A Theoretical Approach for 30° Angle of Observation	139
A.3 Numerical Study: Velocity Decay Rate for Variable Striking/Observation Angle Combinations	144
A.3.1 30° Strike:	144
A.3.2 0° Strike:	146

List of Figures

2.1	Experimental configuration	17
2.2	Custom fabricated sensor particles: (Left) Photographs of cut sensor sphere, sensor, and assembled sensor particle. (Right) Schematic diagram of the assembled sensor particle: top view and cross section view. The accelerometer is a 6.35 mm cube and the sphere is 19.05 mm in diameter.	18
2.3	Top: Response at the “defect” particle, central particle in a chain of 20 spheres, when its mass is 100% (Left) and 50% (Right) of the solid sphere mass. Bottom: Relative amplitude of the largest reflection felt at particle the “defect” particle for various mass ratios. The x-axis is a ratio of the mass of the “defect” particle over the mass of a solid stainless steel sphere. The y-axis is the ratio of the amplitude of the largest reflection to the amplitude of the incident solitary wave. The systems relative response is independent of striker velocity.	19
2.4	Force at the wall for a chain of 20 spheres with and without sensor particles. The baseline test configuration (a) consists of a chain of 20 solid stainless steel spheres. Force at the wall when sensor particles replace the (b) 6th, (c) 11th, (d) 16th, (e) 11th and 16th, and (f) 6th, 11th, and 16th solid spheres. The ten impacts for each test configuration are all shown.	19

- 3.1 Schematic diagrams of the test configurations: (Top) view of the setup from the side, showing the position of the striker spheres (dark grey) and (Bottom) view of the setup from the top. The square array was a 20 by 20 packing of 19.05 mm diameter spheres. For the in-plane impacts, the striker sphere impacted the resting striker sphere in contact with edge particles X_1Y_{10} and X_1Y_{11} . For out-of-plane impacts, the striker sphere impacted the resting striker sphere in contact with central particles $X_{10}Y_{10}$, $X_{11}Y_{10}$, $X_{10}Y_{11}$, and $X_{11}Y_{11}$ 29
- 3.2 Density plots corresponding to the amplitude of the particle velocity obtained from numerical simulations as a function of spatial position in the granular crystal. (Left) At 0.15 milliseconds and (Right) at 0.30 milliseconds after the array was impacted in-plane with a striker velocity $V_x = 0.29\text{m/s}$. The grey-scale indicates the particle velocity amplitude in m/s. 31
- 3.3 Experimental and numerical simulation responses of the two central chains in the granular crystal resulting from an in-plane impact. (a) Schematic diagram showing the experimental setup and the positions of the sensor particles (shaded spheres indicate particles excited by the impulse). (b) Signals recorded at the sensor locations. The top panel represents experimental results and the bottom panel the numerical simulations. In both experiments and simulations each particle's acceleration in the x-direction is plotted as a function of time. The experimental y-acceleration was nearly zero for all sensor locations (zero in simulations) and was therefore not plotted. 32

- 3.4 Experimental and numerical simulation responses of the two edge chains in the granular crystal resulting from an in-plane impact. (a) Schematic diagram showing the experimental setup and the positions of the sensor particles (shaded spheres indicate particles excited by the impulse). (b) Signals recorded at the sensor locations. The top panel represents experimental results and the bottom panel the numerical simulations. In both experiments and simulations the particle's acceleration obtained from sensors 2A, 2B, and 2C in the negative y-direction is plotted as a function of time. The experimental x-acceleration was nearly zero for all sensor locations (zero in simulations) and was therefore not plotted. The signal plotted for sensor 2D includes the total magnitude of the x- and y-particle acceleration. 33
- 3.5 Density plots corresponding to the amplitude of the particle velocity obtained from numerical simulations as a function of spatial position in the granular crystal. (Left) At 0.15 milliseconds and (Right) at 0.30 milliseconds after the array was impacted out-of-plane with a striker velocity $V_z = -0.65\text{m/s}$. The grey-scale indicates the particle velocity amplitude in m/s. 34
- 3.6 Experimental and numerical simulation responses of the central chains in the granular crystal resulting from an out-of-plane impact. (a) Schematic diagram showing the experimental setup and the positions of the sensor particles (shaded spheres indicate particles excited by the impulse). (b) Signals recorded at the sensor locations. The top panel represents experimental results and the bottom panel the numerical simulations. In both simulations and experiments the particle's acceleration in the negative y-direction is plotted as a function of time. The experimental x-acceleration was nearly zero for all sensor locations (zero in simulations) and was therefore not plotted. The signal plotted for sensor 3D includes the total magnitude of the x- and y-particle acceleration. 35

- 3.7 Wave speed vs. maximum particle velocity for the central chains when the system is impacted in-plane. The squares denote tests for sensor locations 1B and 1C, while the stars denote tests when sensors are moved to the adjacent chain (1A and the respective neighboring particle of 1C, location $X_{15}Y_{10}$). Results of the linear regression on the log-log data for both experiments and simulations are shown (with 95% confidence intervals). 37
- 3.8 Wave speed vs. maximum particle velocity for the edge chains when the system is impacted in-plane. The squares denote tests for sensor locations 2B and 2C, while the stars denote tests when sensors are moved to the opposite chain (2A and the respective neighboring particle of 2C, location X_1Y_{18}). Results of the linear regression on the log-log data for both experiments and simulations are shown (with 95% confidence intervals). 37
- 3.9 Wave speed vs. maximum particle velocity for the central chains when the system is impacted out-of-plane. The squares denote tests for sensor locations 3B and 3C, while the stars denote tests when sensors are moved to the adjacent chain (3A and the respective neighboring particle of 3C, location $X_{10}Y_3$). Results of the linear regression on the log-log data for both experiments and simulations are shown (with 95% confidence intervals). 38

- 3.10 Wavelength of the solitary wave as a function of distance from the impact (N). The dotted lines represent the theoretical values from Nesterenko's long wavelength approximation and the solid lines represent a smoothed curve through simulation data. Circles represent data from sensor locations 1C and 1D (Figure 3.3) and squares represent data from sensor locations 2B and 2C (Figure 3.4) after the array was impacted in-plane. The crosses represent data from sensor locations 3B and 3C (Figure 3.6) after the array was impacted out-of-plane. (a) Wavelength calculated by fitting the acceleration curves to Nesterenko's waveform. (b) Wavelength calculated by fitting the (integrated) velocity curves to Nesterenko's waveform (Equation 1.3). (c) Wavelength at half maximum amplitude directly calculated from the acceleration profiles. (d) Wavelength at half maximum amplitude directly calculated from the (integrated) velocity data. Error bars extend two standard deviations from the mean values. 40
- 4.1 Schematic diagram of the experimental setup. The striker sphere impacted a resting striker sphere located between the 10th and 11th spherical particles along the edge. Sensors A, B, and C are located at positions X_8Y_{10} , X_8Y_7 , and X_8Y_4 of the 20 by 20 spherical square array, respectively. 43

- 4.2 Schematic diagrams showing the sensor locations in experiments. (a) Sensor configuration 1 had sensors 1A, 1B, 1C, and 1D located at X_8Y_{10} , X_8Y_7 , X_8Y_4 , and X_8Y_{14} of the 20 by 20 sphere array for all material combinations. (b) Sensor configuration 2 had sensors 2A, 2B, 2C, and 2D located at X_8Y_{10} , $X_{12}Y_{10}$, $X_{16}Y_{10}$, and X_8Y_{11} of the 20 by 20 sphere array for the steel^s-ptfe^c, delrin^s-ptfe^c, and steel^s-steel^c crystals. Sensors 2A, 2B, 2C, and 2D were moved to locations X_4Y_{10} , X_8Y_{10} , $X_{12}Y_{10}$, and X_4Y_{11} of the 20 by 20 sphere array (4 spheres closer to the impact), due to small signal amplitudes for the delrin^s-steel^c crystals at locations far from the striker impact. (c) Sensor configuration 3 had sensors 3A, 3B, 3C, and 3D located at X_4Y_8 , X_6Y_6 , X_8Y_4 , and X_8Y_{10} of the 20 by 20 sphere array for all material combinations. For all experiments, the striker sphere impacted the system between the 10th and 11th edge spheres with initial velocity V_x 44
- 4.3 Schematic of extended granular crystal analyzed in the present study. Larger sized granules represent spheres (radius, R) while smaller ones are cylinders (radius, r). Wave propagation studies are performed on an extended set of this packing by giving a symmetric disturbance, setting initial velocities on four spherical granules as shown. 45
- 4.4 (Color online) (Center) Different wave propagation regimes mapped on mass (m_2/m_1) and stiffness (E_2/E_1) ratio space for the cylinder-sphere (2-1) system. (Top) Diagrams depicting examples of different wave fronts achievable in the systems at selected mass and stiffness ratios, indicated with circles in the central figure. (Bottom) Four insets depicting the propagating wave front shapes for the four material systems tested in experiments, indicated with diamond-shaped symbols in the central figure. 47

4.5 Numerical simulation results showing the wave front shape in terms of particle velocity magnitude for each of the experimentally tested material configurations. X- and y-axes represent the particle position. For the steel sphere configurations, Figures (a) and (c) show particle velocities 0.35 ms after the steel striker sphere impact ($V_x = 0.73$ m/s). For the delrin sphere configurations, Figures (b) and (d) show particle velocities at 1.0 ms after the delrin striker sphere impact ($V_x = 0.92$ m/s). Grey scales indicate particle velocity in m/s. 49

4.6 Comparison of individual particle acceleration as a function of time between experiments and simulations for each of the sphere-cylinder material combinations tested: (a) steel-ptfe, (b) delrin-ptfe, (c) steel-steel, and (d) delrin-steel. Acceleration data at sensor locations B and C were shifted up 1500 and 3000 m/s^2 , respectively, for visual clarity. Zero time in simulations was defined as the moment of striker impact. To compare experimental and simulation data, experimental data for each test configuration was shifted so the signal arrival time of sensor A in simulations and experiments coincided. 50

4.7 (Top) Ratio of the maximum acceleration amplitude at sensor locations C and A plotted against the ratio of the sphere-cylinder (Left) stiffness and (Right) masses. For experimental data, the mean and standard deviation, std, (error bars) are plotted for each of the three initial packings assembled for each material configuration. (Bottom) The x-accelerations at sensor locations A, B, and C (positioned as in Figure 4.6) most closely representing +1 std (solid blue) and -1 std (dashed black) for Pack 1 are plotted for each sphere-cylinder material configuration: (a) steel-ptfe, (b) delrin-ptfe, (c) steel-steel, and (d) delrin-steel. Y-ticks indicate 1000 m/s^2 . X-ticks indicate 0.1 ms for (a) and (c) and 1.5 ms for (b) and (d). 52

- 4.8 (Color online) Peak acceleration (m/s^2) in the wave front as a function of X1 (in units of spheres) for each sphere - cylinder material combination: (a) steel^s-ptfe^c, (b) delrin^s-ptfe^c (c) steel^s-steel^c, and (d) delrin^s-steel^c. The results from numerical simulations for the ideal granular crystal are shown by the solid (red) lines. The mean and standard deviation are represented by a dashed lines and dark (blue) shaded regions for the MR-SI (15 realizations each with a single impact) and by dot-dashed lines and light (grey) shaded for the SR-MI (a single realization with 15 impacts). The experimental data is represented by black dots with error bars for the 3 realizations tested with 15 impacts each. 54
- 4.9 (Color online) Peak acceleration (m/s^2) in the wave front as a function of X1 (in units of spheres) for the steel^s-steel^c crystal. The results from numerical simulations for the ideal granular crystal are shown by the solid (red) lines. The mean and standard deviation for 3 single realizations with 15 multiple impacts (SR-MI) are represented by dot-dashed lines and shaded light grey regions. The experimental data is represented by black dots with error bars for the 3 realizations tested with 15 impacts each. 55
- 4.10 (Color online) Relative wave front arrival times along X1 (spheres) with respect to sensor location 1A, for the delrin^s-ptfe^c crystal. The results from numerical simulations for the ideal granular crystal are shown by the solid (red) lines. The mean and standard deviation are represented by a dashed line and dark (blue) shaded region for the MR-SI and by a dot-dashed line and light (grey) shaded region for the SR-MI. For each sensor location along X1, 3 sets of black dots and error bars represent the mean and standard deviation for the 3 single experimental realizations with multiple impacts. 55

- 4.11 Experimental and numerical simulation results for the x- and y-acceleration profiles for sensor configuration 1 (see Fig. 4.2) of the delrin^s-ptfe^c granular crystal. (a) Simulation results for the ideal granular crystal. (b) Experimental results for a single packing (SR) impacted 15 times. (c) Numerical simulation results for 15 different realizations (MR), each impacted once. (d) Numerical simulation results for a single realization (SR), impacted 15 times. For visual clarity, the acceleration data at sensor locations 1B, 1D, and 1C are shifted by 1000, 2000, and 3000 m/s^2 , respectively, from sensor location 1A. The zero time in the simulations denotes the moment of impact, while the zero time in experiments is arbitrary since the recorded data is based off the signal arrival time of sensor 1A. 58
- 4.12 (Color online) Peak acceleration (m/s^2) in the wave front versus X2 (in units of spheres) for each sphere - cylinder material combination: (a) steel^s-ptfe^c, (b) delrin^s-ptfe^c (c) steel^s-steel^c, and (d) delrin^s-steel^c. The results from numerical simulations for the ideal granular crystal are shown by the solid (red) lines. The mean and standard deviation are represented by dashed lines and dark (blue) shaded regions for the MR-SI and by dot-dashed lines and light (grey) shaded regions for the SR-MI. For each sensor location along X2, a set of black dots and error bars represent the mean and standard deviation for the single experimental realization with multiple impacts. 60

- 4.13 (Color online) Peak acceleration (m/s^2) in the wave front as a function of X3 (in units of spheres) for each sphere - cylinder material combination: (a) steel^s-ptfe^c, (b) delrin^s-ptfe^c (c) steel^s-steel^c, and (d) delrin^s-steel^c. The results from numerical simulations for the ideal granular crystal are shown by the solid (red) lines. The mean and standard deviation are represented by dashed lines and dark (blue) shaded regions for the MR-SI and by dot-dashed lines and light (grey) shaded regions for the SR-MI. For each sensor location along X3, a set of black dots and error bars represent the mean and standard deviation for the single experimental realization with multiple impacts. 61
- 4.14 Numerical simulation results qualitatively showing the dependence of the wave front shape on the ratio of the impact force F_{impact} to the static compression F_{static} . Each row represents a single sphere^s – cylinder^c material combinations, for which a unit cell is also picture on the left. 64
- 5.1 Schematic diagram of the experimental setup. The solid stainless steel sphere locations are represented with grey circles. The confining walls are represented by solid black lines. The striker sphere impacts the system as shown, with an initial velocity $V_{striker}$ in the x -direction. The locations of sensor particles are marked with a red circle and outlined in black. The number next to each sensor location indicates the different sensor configurations: 1, 2, and 3 (with 4 sensors present for any given experiment). 67
- 5.2 (a) Orientation of the hexagonal lattice and possible striking and observation angles. The numeric labels correspond to the counting conventions used along the respective observation angles. 68

5.3	<p>(a) Velocity profile for the first ten beads in an initially at rest 1D granular crystal after impact on the left boundary with $A = d = M = 1$. Notice that the maximum velocity attained by each bead is approximately constant after impact (denoting the rapid settling of the chain into a traveling solitary wave). (b) Velocity profile for the first ten beads along the zero degree line (refer to Figure 5.2) of an initially at rest 2D hexagonal granular crystal with $A = d = M = 1$. Notice that the maximum velocity attained by each bead decays (denoting the spreading of the energy to an increasing number of beads). Refer to Appendix A or Equation 5.1 for rescaling relations.</p>	69
5.4	<p>Numerical simulation results showing the wave front shape evolution for the 11-sphere edge system tested in experiments. The array was centrally impacted along the edge by a striker sphere with initial velocity $V_{striker} = 0.40 \text{ m/s}$. The colorbar indicates particle velocity magnitude in m/s.</p>	70
5.5	<p>Numerical simulation results showing the wave front shape evolution for a larger hexagonal packing (91 particles along the left, long edge, and 45 particles along the shorter edges). The array was centrally impacted along the edge by a striker sphere with initial velocity $V_{striker} = 0.40 \text{ m/s}$. The black hexagon indicates the wall locations for the size of the experimental setup. The colorbar indicates particle velocity magnitude in m/s.</p>	70
5.6	<p>(b) The arrival time of the pulse for the experimental parameter values at a 0° strike and 30° observation angle with $V_0 = 0.4 \text{ m/s}$. The blue dots represent numerical simulations, the red circles are the TCA (EQ 5.2), the black triangles denote the exact analytical solution to the TCA (see Appendix A), and the points with error bars at $n = 6$ and $n = 10$ are the experimental values.</p>	72

- 5.7 Wave front shape based on the relative wave front arrival time with respect to the particle marked with a white x. (a) Numerical simulation of ideal system. (b) Average wave front arrival time calculated from experiments. (c) Average wave front arrival time calculated from simulations with weak disorder. Black circles in the left and right panels indicate experimental sensor locations. The colorbar indicates the relative wave front arrival time in milliseconds. 74
- 5.8 Maximum particle velocity with respect to sphere position, n . (a), (c), (e): 0° Strike and 0° Observation. (b), (d), (f): 0° Strike and -30° Observation. Initial velocity: (a), (b) $V_0 = 0.25$ m/s; (c), (d) $V_0 = 0.40$ m/s; and (e), (f) $V_0 = 0.70$ m/s. Shaded grey regions indicate ± 1 standard deviation, σ , and dotted grey lines indicate the average value, μ , from the 20 simulations incorporating weak disorder. The solid red lines represent Equations (5.5) and (5.4). The black dots and error bars represent the mean and standard deviation from experiments ($V_0 = 0.25$, 0.40 , and 0.70 m/s for 0° Strike 0° Observation and $V_0 = 0.40$ m/s for 0° Strike 30° Observation). 75
- 5.9 Schematic diagram of a 2D dimer hexagonal array. The dark and light grey particles indicate the two different materials composing the dimer array. 77
- 5.10 Numerical simulation results showing the wave front shape evolution for the dimer system with 26-spheres along the short edges. The sphere materials are aluminum and stainless steel, light and dark grey, respectively, in Fig 5.9. The array was centrally impacted along the edge by an aluminum striker sphere with initial velocity $V_{striker} = 0.50$ m/s. The colorbar indicates particle velocity magnitude in m/s. 78

5.11	Numerical simulation results showing the wave front amplitude decay for a 0° aluminum striker with $V_{striker} = 0.5 \text{ m/s}$ observing at (a) 30° and (b) 0° . The x-axis bead numbering, n , follows the same scheme as described in Figure 5.2. The red diamonds indicate numerical simulations for a hexagonal monomer of aluminum spheres. The blue asterisks indicate numerical simulations for a dimer with steel and aluminum (same as Fig 5.10).	79
5.12	Numerical simulation results showing the full width at half max (FWHM) of the leading pulse along the 30° observation direction for the aluminum monomer (red diamonds) and aluminum-steel dimer (blue asterisks).	79
6.1	Schematic diagram of the granular network investigated in this study. (Left) The wave transmission coefficients at each of the straight segments is given as a function of elementary transmission coefficients, T_S , T_C and T_M , and corresponds to $N=1$ up to $N=4$ levels structures. (Right) The transmitted force F profile as a function of the normalized distance r from the middle of the network.	82
6.2	Pictures of experimental setup. (a) Solenoid impacting mechanism. (b) Assembled granular network with inset showing the v-shaped cross section of the supporting channel structure. (c) Dynamic force measurements taken at each branch end.	83
6.3	(Top) Schematic diagram of a unit cell configuration depicting the splitting transmission coefficient T_S , the corner transmission coefficient T_C and the recombination transmission coefficient T_M . (Bottom) Comparison of numerical simulations and theoretical predictions for T_C (Left) and T_M (Right) for branch angles α between 30 and 45 degrees. In numerical simulations, the incident and transmitted amplitudes were calculated using the average maximum force from particles 7 through 11 along each segment.	86

- 6.4 Schematic diagram describing the choice of transmission coefficient used to model the transmitted leading pulse amplitude F^t at junctions where two granular chains merge together. F_{LB}^i and F_{UB}^i denote the incident force amplitudes in the lower and upper branch, respectively. 88
- 6.5 Numerical simulations and experimental results of the force profiles at each branch end for the tested $N=1$ through $N=4$ networks. (Left) Schematic diagram of the branch network for each level. The force profiles correspond to particles denoted in black. For each level, the amplitude was normalized by the amplitude of particle*. (Middle) Numerical simulations and (Right) a single experimental test for each of the tested networks ($N=1-4$). The force profiles of each branch end are offset by 1 N for visual clarity. Y-ticks denote 0.5 N and x-ticks denote 0.1 ms. 89
- 6.6 F_{middle}^t (normalized by the input force, F^i) as a function of branch levels, N . (Left) Numerical simulations are represented in black markers and experimental results in blue markers for $N = 1 - 4$ for the tested network with six particles per chain. The linear fit through the simulation data is represented by a dotted black line and the linear fit through the experimental data by a dot-dashed blue line. (Right) Numerical simulations are represented in black markers for $N = 1 - 6$ for the network with 16 particles per chain. The linear fit through the simulation data is represented by a dotted black line and the theoretical predictions by a solid red line. 91

- 6.7 Spatial repartition of the normalized transmitted force F^t/F_{middle}^t as a function of the distance $y = Nr$ to the middle axis of the network. The insets show the force spatial distribution F^t/F_{middle}^t as a function of the normalized distance r . (Left) Numerical simulations are represented in black markers and experimental results in blue markers for $N = 1 - 4$ for networks with six particles per chain. The linear fit through the simulation data is represented by a dotted black line and the linear fit through the experimental data by a dot-dashed blue line. (Right) Numerical simulations are represented in black markers for $N = 1 - 6$ for networks with 16 particles per chain. The linear fit through the simulation data is represented by a dotted black line and the theoretical predictions by a solid red line. 95
- 6.8 Variations of the transmission coefficient T^E in terms of transferred acoustic energy through one stage of the granular chain network for the middle and side exit chains for both theoretical predictions (see Eq. (6.13) and (6.14)) and numerical simulations of the long branch (16 spheres per segment) networks with variable branching angles α . The overall transmitted acoustic energy follows $E^t = E^i (T^E)^N$ 97
- 6.9 (Top) Spatial distribution of the energy of a harmonic wave transmitted through a conventional 2D continuum material. (Bottom) Spatial distribution of acoustic energy in ordered granular networks (granular acoustic metamaterial). 98
- 7.1 (a) Pictures of the $N = 3$ experimental setup. (b) Schematic diagram of granular network geometry, and definition of branch level, N . (c) Transmission coefficients at each of the branch ends for networks with branching level $N = 1, 2$, and 3. (d) Schematic diagram describing the four different transmission coefficients: T_S wave splitting, T_C bending, T_{M3} 3 identical incident pulses combining, and T_{M2} 2 identical pulses combining at incident angle α 104

- 7.2 Comparison of numerical simulations and theoretical predictions for (a) T_S , (b) T_C , (c) T_{M3} and, (d) T_{M2} for branch angles α between α_{min} and 50 degrees. The dashed black line represents the quasi-particle predictions (Equations (7.1) - (7.4)). The blue squares represent the transmission coefficients calculated from numerical simulations including wall particles and the green circles from simulation without walls. . . . 107
- 7.3 Numerical simulations and experimental results of the force profiles at each branch end for the tested N=1 through N=3 networks. (Left) Schematic diagram of the branch network for each level. The force profiles correspond to particles denoted in black. For each level, the amplitude was normalized by the amplitude of particle*. (Middle) Numerical simulations and (Right) a single experimental test for each of the tested networks (N=1-3). The force profiles of each branch end are offset by 1 N for visual clarity. Y-ticks denote 0.5 N and x-ticks denote 0.1 ms . . . 108

7.4 Distribution of leading pulse amplitudes. The marker shapes indicate the branch level: $N1$ =circle, $N2$ =square, $N3$ =diamond, $N4$ =cross, $N5$ =triangle, and $N6$ =plus. **(a)** Theoretical distribution of pulse amplitudes. The normalized amplitudes based on quasi-particle transmission coefficients are represented with black marker outlines, and Equation (7.5) is shown in the dashed red lines and dotted black lines in the inset. **(b)** Normalized central pulse amplitude F_{middle}/F_i with increasing branch level N : theory, experiments, and simulations. The dotted red line represents Equation (7.6), the solid black markers indicate numerical simulations, and the blue dots and error bars represent experiments. The error bars for $N = 1$ and 2 represent 2 standard deviations 2σ , where σ was calculated from the set of 7 initial experimental configurations. The error bars for $N=3$ represent the 95% confidence intervals for the normalized F_{middle} obtained from a linear regression of $\log F_r$ vs r . **(c)** Spatial repartition of leading pulse amplitudes: theory, experiments, and simulations. The colored contour levels of F_r/F_{middle} represent Equation (7.6), and the markers represent the average values from experiments. The inset shows the data before normalization with ξ . The blue markers and error bars represent the mean and standard deviation from experiments, and the solid black markers represent the numerical simulations. **(d)** Total system response. The color bar indicates the transmitted primary pulse amplitudes normalized by the impact force F/F_i . The three insets compare the theoretical predictions, contours, with average values from experiments, markers. 111

A.1 (a) Orientation of the hexagonal lattice and possible striking and observation angles. The numeric labels correspond to the counting conventions used along the respective observation angles. (b) Labeling convention for the ternary collision approximation 139

- A.2 (a) Observed pulse velocity of the propagating structure in the ideal parameter case at various bead numbers n for a 30° strike and 30° observation angle. The pulse velocity is defined as $c_n = 1/T_n$ where T_n is the n th residence time. The blue dots represent the calculated time based on numerical simulations and the red circles are the prediction based on the TCA. The black triangles denote the exact analytical solution to the TCA system (which, however, is only approximate). The initial strike velocity was $V_0 = 0.1$. (b) The arrival time of the pulse for the experimental parameter values at a 0° strike and 30° observation angle with $V_0 = 0.4$ m/s. The blue dots represent numerical simulations, the red circles are the TCA, the black triangles denote the exact analytical solution to the TCA, and the points with error bars at $n = 6$ and $n = 10$ are the experimental values. 143
- A.3 Illustration of the procedure to obtain the scaling law for the decay of the velocity profile. This example is for strike and observation on the 30° line. (a) Magnitude of velocity of beads 0 – 12 versus time in the ideal parameter case with $V_0 = 0.05$. The maxima are fit with a function of the form $V_1 c^{n-1}$, where V_1 is the maximum velocity of the first bead (labeled in the plot). This process is repeated for several values of V_0 to obtain a sequence of decay rates $c(V_0)$. (b) The sequence of decay rates $c(V_0)$ are fairly accurately fit with a linear function (see the text). (c) The relationship between V_0 and V_1 is computed, and can be either linear (like in this case) or quadratic. Finally, putting these relationships together yields a formula for the maximum velocity at a given bead, see, e.g., Eq. (A.9). (d) For a 0° observation, the fitting begins at bead 2, where the relationship between the initial striking velocity V_0 and V_2 is quadratic. 145

- A.4 (a) magnitude of the velocity of beads 0–12 along the 0° line upon being struck at a 0° angle. In this case, the fitting is more accurate starting at the second peak V_2 . (b) The relationship between the initial striking velocity V_0 and V_1 for a 0° strike and 30° observation is quadratic. For this particular case, we see that $V_1 \approx V_0/2$ 147

List of Tables

2.1	Material Properties [1–4]	24
6.1	Comparison of the decay length scales N_0 and ξ_0 for theoretical predictions, long branch network (16 particles per branch) numerical simulations and short branch network (6 particles per branch) experiments and numerical simulations	96

Chapter 1

Introduction

This thesis is a study of the fundamental dynamic behavior of ordered granular systems, with a broader goal to design new, structured (granular) materials with unique physical properties. The term *granular crystal* will be used to define this special category of highly ordered granular materials where the geometry and material properties of each particle are predefined and particles are arranged in a highly ordered or lattice-like configuration. The dynamic behavior of granular crystals is an extremely rich topic, which can be broken up into three regimes based on the level of exhibited nonlinearity (i.e., the relative excitation or dynamic wave amplitude compared to the static compression $F_{dynamic}/F_{static}$) [5]: linear, weakly nonlinear, and highly nonlinear. Within the scope of this thesis, I focus on the highly nonlinear regime (i.e., $F_{dynamic} \gg F_{static}$), varying the underlying particle structure in order to develop means for controlling the wave propagation pathway for impact mitigation applications.

This introduction first gives a brief overview of the emerging field of engineered material design, and discusses the choice of granular systems as the framework for material design in the context of this thesis. Then, a more detailed background of the load transfer pathway and dynamic behavior of granular materials are described, including previously studied effects of particle microstructure on wave propagation and the exploitation of granular crystals for application specific engineered material design.

1.1 Motivation and Significance

Both natural and man-made materials make use of material structure to obtain advantageous mechanical properties. For example, the hierarchical structure of human bone [6] leads to beneficial highly anisotropic strength while maintaining low density. Similarly, laminar fibrous composites, allow for the combination of high stiffness (in preferential directions) and lightweight material design, which is now textbook material [7]. Recently, however, there has been a shift in engineered material design to exploit material structure in order to attain effective material properties beyond what is observed in nature.

The term metamaterial has emerged to describe a new class of materials composed of artificial, or engineered, structural elements designed to achieve advantageous and unusual properties [8]. Metamaterials were first conceived to achieve specific macroscopic electromagnetic (EM) and optical behaviors not readily occurring in nature [9]. As a result, a more strict, or conventional, use of the term metamaterial, is limited to those composed of a periodic arrangement of identical structural elements, in which unique effective properties can be derived for a range of frequencies where the wavelength is comparable to the scale of the underlying structure. More recently, however, researchers have focused on the design of a variety of mechanical metamaterials, with both unique static and dynamic properties [10], broadening the use of the term.

Milton and Cherkaev were the first to theoretically investigate the range of achievable unconventional linear elastic properties [11]. Theoretically, any of these “extreme materials” can be achieved with the use of pentamode building blocks, i.e., artificial three-dimensional structures that have a finite bulk modulus but vanishing shear modulus [12]. Auxetics, defined as those possessing a negative Poisson’s ratio (also unimodes for $\nu = -1$), are a special class of these extreme material, that can be achieved through a variety of different material structures [13, 14]. Several additional realized mechanical metamaterials include, an engineered composite with an elastic modulus greater than either of its material components [15], and ultra-light

metallic lattice structures [16]. While much of the mechanical metamaterial design thus far has been limited to linear elastic deformations, recent interest in buckling induced deformation [17] suggest a move towards a new category of unique material deformation.

Researches have also looked for acoustic counterparts traditional EM metamaterials: linear acoustic metamaterials with negative effective Young's modulus or mass density ([18, 19]). In particular, some of these systems can prevent the propagation of harmonic waves, behaving like super absorbers with a transmission coefficient close to zero in some range of frequencies [20, 21], which can be chosen by tuning the metamaterial microstructure [20, 22]. Beyond vibration absorption, acoustic metamaterial design has focused primary on acoustic cloaking [23].

In this thesis, we propose a granular framework for the basis of new waveguide metamaterial design, which could be used, for example, for impact mitigation. Current structured materials proposed for impact mitigation primarily consist of foams [24], auxetic cellular solids [14], and structured composites [25]. These materials make use of permanent deformation or viscoelastic properties to dissipate the transmitted energy, in many cases limiting the repeated use or effective frequency and temperature range of the materials. The building block of our acoustic metamaterial is the network of inter-particle contacts. Even though the entire granular structure can be composed of a linear elastic material (such as metallic spheres), the resulting wave propagation is highly nonlinear as a result of the nonlinear contact mechanics between grains. In this thesis, we take a new approach to wave mitigation, spatially and temporally controlling the nonlinear wave propagation as opposed to dissipating the acoustic energy.

1.1.1 Choice of Granular Framework

Granular materials consist of a collection of discrete solid particles, such as sand, rice, or ball bearings. The unique mechanical behavior of granular systems is dictated by the nonlinear, Hertzian [26], relation between individual particles in compression and

their lack of tensile strength. For two curved particles in compression, the repulsive force increases with the relative displacement between the particles δ as $F = K\delta^{3/2}$, where the stiffness coefficient K is a function of the particle shapes and material properties (see Section 2.3.1 for exact sphere-sphere and sphere-cylinder relations). These two sources of nonlinearity lead to drastically different dynamic properties compared to a solid media of the same material. Additionally, the propagating wave characteristics are highly dependent on the underlying particle structure: disordered granular media exhibit complicated variable force chain networks (see Section 1.3), while ordered granular systems, or granular crystals, display highly ordered wave structures with distinct properties (see Section 1.2).

These attributes make granular materials particularly attractive as a framework for engineered material design. Variable particle arrangements can be fairly easily assembled, and the strong dependence of force transmission on particle arrangement allows for the design of complex predetermined wave propagation paths. Additionally, the nonlinear force-displacement relation allows for an added level of tunability, by controlling the pre-compression.

As mentioned, the choice of granular crystals allows for a different approach to wave mitigation, spatially and temporally redistributing the acoustic waves from an impact. As will be discussed in Section 1.2.1, the inherent ability of these granular chains to break up large amplitude or long duration excitations into a series of smaller pulses makes them ideally suited for wave mitigation applications, and a number of previous studies have proposed various one-dimensional (1D) granular crystal designs for impact mitigation (Section 1.2.1.1). This thesis focuses on two- and three-dimensional (2D and 3D) granular systems, allowing for spatial wave mitigation not possible in one-dimensional arrays. Additionally, we study the highly nonlinear wave propagation in the elastic regime, which means these systems not only exhibit reversible deformation but also effectively function over all frequencies.

Beyond the applications of these microstructured materials as acoustic shields, granular crystals, especially the ordered networks described in Chapters 6 and 7, serve as a model system to investigate the acoustic properties of natural granular

piles. The dynamic behavior of granular materials is relevant for various applications of geophysics, soil mechanics, materials science, etc., however, much work still needs to be done to fully understand the complex behavior of these systems [27–29]. The pulse splitting, bending, and combining studied in ordered granular networks physically captures all the relevant load transfer mechanisms observed in force chain networks of disordered granular. Therefore, this work may also provide a framework for deriving the effective acoustic behavior of disordered or natural granular matter.

1.2 Structured (Engineered) Granular Materials

Structured, or engineered, granular systems present unique dynamic properties, not observed in natural, disordered granular media. One-dimensional theory and previous numerical and experimental works are discussed to develop an understanding of the waves supported by these systems, namely solitary waves, and how the behavior of these waves at boundaries have been exploited to design one-dimensional granular protectors. While the transient dynamic response of one-dimensional highly nonlinear (uncompressed) granular chains has been extensively studied, few reports have explored wave propagation in higher-dimensional granular crystals. Prior works on highly nonlinear 2D or 3D granular crystals consist of a small collection of numerical simulations and experiments aimed at describing the stress wave behavior. The extension of these studies in higher-dimensional systems could enable the discovery of richer physical phenomena and the design of materials for different engineering applications.

1.2.1 1D Systems

In the elastic limit, a homogeneous chain of particles excited by a single impulse has been extensively studied, and shown to support the formation and propagation of solitary waves [5, 30–39]. The unique solitary waves supported by these particle chains were first described analytically by Nesterenko [30], when he considered a chain

of uniform spheres obeying the Hertz contact law [26]:

$$F = \frac{2E}{3(1-\nu^2)} \sqrt{\frac{R}{2}} \delta^{3/2}. \quad (1.1)$$

Writing the equation of motion for a sphere in an infinite chain, and applying Nesterenko's long wavelength approximation [5, 30], the fundamental wave equation derived for the highly nonlinear response of an uncompressed particle chain is

$$u_{tt} = -c^2 \left\{ (-u_x)^{\frac{3}{2}} + \frac{2R^2}{5} \left[(-u_x)^{\frac{1}{4}} \left((-u_x)^{\frac{5}{4}} \right)_{xx} \right] \right\}_x, \quad (1.2)$$

where u represents the displacement of the center of each sphere from its equilibrium position and $c^2 = \frac{2E}{\pi\rho(1-\nu^2)}$. The propagating wave in the highly nonlinear regime can be described by a single hump of the periodic solution of Equation 1.2 [5, 30]:

$$v = V_{sw} \left(\frac{5V_{sw}^2}{4c^2} \right)^2 \cos^4 \left(\frac{\sqrt{10}}{10R} x \right), \quad (1.3)$$

where v is the particle velocity and V_{sw} is the solitary wave speed. This solitary wave has a fixed wavelength of approximately 5 particle diameters and a wave speed that depends on its amplitude [5, 30, 38]:

$$V_{sw} = \left(\frac{16}{25} \right)^{\frac{1}{5}} c^{\frac{4}{5}} v_m^{\frac{1}{5}} = 0.68 \left(\frac{E}{R\rho^{\frac{3}{2}}(1-\nu^2)} \right)^{\frac{1}{3}} F_m^{\frac{1}{6}}, \quad (1.4)$$

where v_m is the maximum particle velocity and F_m the maximum compressive contact force. The existence of this compact solitary wave was first shown experimentally by Lazaridi and Nesterenko [31] and later confirmed experimentally [32, 35, 38–40] and numerically [34, 36, 41] by others. More recently, Lindenberg et al. have developed an alternate theoretical approach based on a binary collision approximation (BCA) [42–46]. The BCA relies on the assumption that at a given time, a significant portion of the energy of the traveling structure is centered over two lattice sites where the resulting equations can then be solved exactly.

While many studies have focused on the simple case of sphere chains, both Nesterenko's long wavelength approximation and Lindenberg's BCA model predict propagating solitary waves for any particle chain with a power-law force-displacement relation $F = K\delta^n$ [5], with exact properties that depend on the power n . More recently, nonlinear solitary waves have been observed in chains of ellipsoidal particles [47, 48], cylindrical particles at variable relative angles [49], hollow spherical particles [50], o-rings [51], and in dimer chains [52–54].

In order to use these granular systems as building blocks for new material structures, it is key to understand how these solitary waves interact with each other [55–59], defects [60, 61], granular interfaces [40, 62, 63] and boundaries [64], and how they respond to long duration impacts or shocks [65–69].

While true solitons can interact with each other and emerge unchanged (except for a phase change) [70], interaction of the solitary waves supported by these granular chains results in the emergence of very small amplitude secondary solitary waves [55–58]. However, numerical simulations show that the amplitude of these secondary effects are very small compared to the primary pulses ($\approx 0.5\%$ of the total kinetic energy [55]), and they have only recently been observed experimentally [59]. While propagating solitary waves do not strongly interact with each other, the presence of boundaries or granular interfaces greatly alters the propagation of incident pulses.

Nesterenko et al. were the first to investigate this interfacial behavior [40]. They experimentally tested the propagation of a solitary wave at the interface of two uncompressed stainless steel chains of different diameters. When the solitary wave arrives from the side of the larger diameter chain, the incident wave is broken into a transmitted solitary wave train (SWT) in the lighter chain and no reflected pulse was observed. However, when the incident wave approaches from the smaller diameter side, a single transmitted and reflected wave were observed on either side of the interface. While these initial results were observed for sphere chains with identical material properties and variable size, similar results can be obtained by maintaining a given diameter and varying material properties [63], or some combination of the two. The formation of these SWTs [67, 68] and anomalous reflections [63] can be attributed to gaps opening

within the granular chain and to successive collisions occurring between the interfacial grains. A similar logic can be applied to understand the response of uncompressed granular chains to long duration or shock-like impacts, in which large amplitude excitations are broken up into SWTs, or a series of pulses with successively decreasing amplitude [65–69]. Several works have exploited the properties of these solitary waves at granular boundaries in order to design one-dimensional impulse mitigating devices [71, 72].

1.2.1.1 Granular Protectors (and Other Applications)

Several different approaches have been taken to exploit the impulse and shock mitigation properties of one-dimensional granular chains [66, 71–82], all of which are based on the described behavior of solitary waves at granular interfaces. Tapered chains, or particle chains of systematically decreasing size, have been studied analytically based on Wu’s independent collision model [73] and the BCA approach by Lindenberg et al. [46], as well as numerically [66, 75–77], and experimentally [74, 78] by others. The driving idea behind these tapered chains is that the traveling energy packets from the impulse or shock are forced to break down into smaller ones at each large-small sphere interface, resulting in a series of lesser amplitude impulses spread over time reaching the other end of the chain. Expanding on the simple tapered chains, decorated tapered chains have been shown to act as even more efficient energy dispersing devices [45, 46, 72]. Another approach to utilizing granular chains as impulse or shock mitigating devices is based on the idea of a granular container, first suggested by Hong [75]. The underlying mitigation method is still to break down the impulse energy into a series of weaker pulses spread out in time. However, it is achieved by containing the impulse in one or more sections of the chain where the energy is slowly leaked out instead of uniformly breaking down the impulse in the chain length [71, 79].

In addition to the design of 1D granular protectors, the solitary wave properties in granular chains have been exploited for a number of other applications. For example, solitary wave reflections could be used for the detection of buried impurities [83] and for testing orthopedic implants and bone integrity [84, 85]. An array

of one-dimensional chains has been proposed for the design of an acoustic lens [86]. Recently, a curved granular chain systems was engineered with amplitude-dependent acoustic filtering properties [87, 88]. Additional proposed applications include sound scramblers [38], actuating devices [89].

It is important to reiterate that the properties discussed here are for the highly nonlinear regime, meaning when the granular chains are uncompressed or when the traveling wave amplitude is much greater than the displacement imposed by some pre-compression. While the focus of this thesis is on the highly nonlinear regime, it is worth mentioning the observed response of granular chains in the linear or weakly nonlinear regime, which leads to a number of interesting applications. Compressed, or linearized, granular chains are known to exhibit band gaps in response to broadband excitations [90], with exact upper cutoff frequencies that can be tuned by the level of pre-compression [91, 92]. Additionally, engineered compressed crystals incorporating defects have been used to localize energy [93] and to design an acoustic diode [94]. Combining the knowledge of granular crystals over a range of physical regimes, i.e., linear through highly nonlinear, could lead to the design of multifunctional devices by varying the level of pre-compression.

1.2.2 2D & 3D Systems

Studies on the dynamic behavior of uncompressed 1D granular chains are far more extensive than that of highly nonlinear 2D or 3D granular crystals. For a simple cubic packing, Nesterenko suggested that waves should propagate similarly to the one-dimensional case when the packing is excited parallel to the array of chains [5], but there is no analogous theory for the wave structures propagating through general ordered, uncompressed 2-3D granular crystals. A primary focus of this thesis is to expand the present knowledge of particle arrangement and stress wave characteristics on the dynamic load transfer pathways in ordered highly nonlinear granular systems.

A significant proportion of the studies on the wave propagation in 2 or 3D granular crystals have focused on the linear or weakly nonlinear response, i.e., the case where

excitation displacements are small or comparable to static loadings [29, 95–102]. In this regime, similar trends were observed for the effective wave speed dependence on static pressure as with disordered granular pilings (1.3); $c \sim P^{1/4}$ at low and $c \sim P^{1/6}$ at high static pressures, respectively [95, 103]. In the highly nonlinear regime of interest, it has been suggested that the force propagation speed follows the predicted Hertzian behavior for both a square and hexagonal spherical particle bed [104].

Previous studies of the static load transfer path in 2D granular crystals showed that ordered granular arrays allow the load to be transmitted primarily along lattice vectors [105–108], in stark comparison to the force chain networks exhibited by disordered particle arrangements (Section 1.3). The dynamic response of 2D granular crystals has also been shown to possess differing, ordered wave propagation paths based on the underlying particle arrangement [47, 109–120]. Shukla et al. were the first to begin investigating the dependence of wave propagation in uncompressed 2D systems on particle arrangement [47, 109–115, 121, 122]. These studies focused either on discrete element simulations [113, 115, 121, 122], or experiments utilizing photoelastic disks [47, 109–112]. Experiments were performed for variable 2D disk arrangements including cubic and hexagonal circular disks spacings [110–112], clearly showing the dependence of the load transfer path on the normal contact angles inherent to the lattice arrangements. Further experiments on cubic and variable hexagonal arrangements of elliptical disks concluded that contact normals and the vectors connecting particle centers of mass (labeled orientation vectors) influence wave propagation characteristics, such as load transfer path and load attenuation [114]. Specifically, higher wave speeds and less attenuation were observed when these orientation vectors and contact normals tended to the direction of wave propagation [114].

More recently, Nishida et al. used DEM simulations to model the dynamic response of a 2D hexagonal packing of spheres [123, 124]. They excited the hexagonal particle bed by a high velocity spherical projectile, and were able to obtain good agreement with experiments when comparing force history profiles along the opposite edge of the specimen. It was determined that the transmitted force could be reduced by increasing the number of layers in the system, or by introducing a dissimilar material

layer [124]. Since the commencement of this thesis project, collaborators/colleagues have also investigated several physical phenomenon in 2D granular crystals, including the redistribution of energy in a square lattice with one or more interstitials [125, 126].

Following the early studies by Shukla et al. [111], recent attention has been given to understand the solitary wave propagation through ordered branching structures [117, 118, 127, 128]. Daraio et al. experimentally and numerically investigated pulse splitting bending and recombination in a y-shaped granular network [117]. Subsequently, Ngo et al. employed the quasi-particle description of Nesterenko’s solitary waves [5, 68] to derive transmission coefficients for y-shaped pulse splitting with variable branch materials and branching angles [118, 127]. Also, their experiments and numerical simulations were shown to be in good agreement with these predicted transmission coefficients. Recently, Qiong et al. [128] have used the BCA model to describe the pulse propagation through the network geometry studied by Dario et al. These studies both provide insight into the dynamic force transmission through disordered media and also serve as a basis for the design of more complex wave guiding systems.

1.2.2.1 Presence of Defects and Weak Disorder

When moving to two or three dimensions, it becomes more difficult to assemble “perfect” granular crystals for experimental studies, due to the interplay between slight variation in particle size and location. The presence of disorder deriving from particle imperfections in real granular arrays is inevitable and results in experimental variability of the load transfer path. A variety of causes could account for the disorder present in real granular assemblies, such as tolerances in the particle size and shape imperfections. Even slight variations in particle sizes can result in the presence of gaps or local compressive forces in the initial contact lattice. It has also been suggested that irregularities in particle surface profiles could lead to deviations from Hertzian behavior and reorganization of particles between successive experiments [129]. Other sources of disorder stem from the redundancy in particle contacts in densely packed arrays and from the presence of friction [105, 107, 108].

The particle imperfections, or small defects, act as weak scattering points [62,

106, 130, 131]. While the majority of load is still transferred along the preferential load path, slight misalignments divert some of the force to neighboring particles [106]. For example, several studies have looked at the effects of weak disorder on the static load transfer path of a triangular or hexagonal array of particles subject to a point load [105–108]. The presence of disorder causes the ideal sharply peaked response to broaden; the further away one looks from the loading point, the less pronounced the ideal load path since the disorder compounds [105–108]. Mueggenburg et al. experimentally observed the same trends for both quasi-static and dynamic loading conditions for a 3D hcp and fcc granular array [106].

Only a few studies considered the effects of weak polydispersity on the dynamic load transfer path in granular crystals [95, 96, 98, 100, 130, 131]. However, these studies again focus on the effects of disorder on the weakly nonlinear behavior of a hexagonal packing of spheres [95, 98, 100]. In the highly nonlinear regime, previous dynamic studies primarily focused on the effects of relatively large imperfections, such as voids [123, 132], significant mass or size deviations [61, 123, 124, 133], and cracks [60]. The presence of large defects causes the scattering behavior to become more pronounced, significantly altering the system response from the undamaged case. By further increasing disorder in the form of significant size and material distributions or disordered particle placements, force chain networks arise and we lose the predetermined load transfer path of interest.

1.3 Disordered (Natural) Granular Materials

This thesis focuses on the unique wave structures achieved through engineered granular systems, which can be better understood through a comparison of our engineered system response to that of natural granular media. The study of natural disordered granular materials is a growing field of study in a range of disciplines, including materials science, physics, and engineering, covering an extremely wide range of topics [27–29]. This section will briefly discuss the body of work most relevant to this thesis, that is, the force transmission pathway and sound propagation through densely

packed disordered granular pilings.

A number of studies investigating statically loaded disordered granular media have shown that an applied force is transmitted along several dominant paths or *force chains* [27, 105, 108, 134–145]. The force chains represent the preferred loading paths based on the individual contact network of each pack, and particles in between these chains remain essentially unloaded. Most of these studies aim at describing the distribution of normal forces at a given depth from the applied load. In several cases, experiments were performed with either carbon paper [139, 146], or with photo elastic disks to visualize and measure the distribution of forces [105, 108, 134, 135, 141, 145]. In general, the description of transmitted normal forces fall into two categories: the “strong” forces, or the distribution of forces above the mean value, and the “weak” forces, or those below the mean force. Most studies agree that the occurrence of “strong” forces follows an exponential distribution [135, 137, 139, 140]. However, different studies propose either a uniform [139, 140, 146] or a power-law [136, 137, 140] distribution of “weak” forces.

The dynamic load transfer within disorder packs appears to follow the same force chains established by static loading [147, 148], however far less studies have investigated the role of dynamic force chains [147–149]. The presence of these dynamic force chains can also be seen for large impacts on granular media where significant particle rearrangement occurs near the penetrating object (see, for example, [150, 151]). Recently, Bassett et al. found that network diagnostics could be useful in determining relationships between transmitted wave characteristics and force chain networks within these granular systems [152].

Several studies have investigated the acoustic transmission and effective sound speed in disordered granular pilings [29, 97, 129, 132, 148, 153–160]. The transmitted acoustic signal through disordered granular media can be categorized into two regimes: (i) a coherent pulse, which arrives first after traveling through the effective medium or contact network, and under certain conditions (ii) a secondary, multiply scattered or coda-like signal [97, 157, 158, 160]. The Hertz theory leads to a power-law scaling between an effective elastic modulus and the static pressure, $E \sim P^{1/3}$, and therefore

the effective sound speed should scale as $c \sim P^{1/6}$ [129]. However, experimental studies frequently show a $1/4$ scaling at low pressures, with a transition to the predicted $1/6$ relation as the static load is increased [97, 129, 156, 157, 159]. Early studies by Goddard et al. theorized that deviations from Hertzian behavior were caused by either conical asphericities or by successive force chain buckling [129]. However, more recent studies seem to suggest that the observed $1/4$ scaling is primarily a result of progressively activated contacts with wave propagation under low static pressures, which does not occur for highly compressed systems where all relevant inter-particle contacts are established prior to the excitation [97, 156, 159].

1.4 Goals and Objectives

The **goals** of this work are to design new materials with novel physical properties. More specifically, this work will contribute to the design of acoustic shielding or impact mitigating materials capable of redirecting and trapping acoustic excitations. These goals can be achieved by developing a fundamental understanding of the dynamic behavior of granular crystals, and how the wave characteristics depend on the underlying particle structure.

The **objectives** of this work are to describe the fundamental wave characteristics in: (i) 2D uniform granular crystals (ii) ordered granular networks of interconnected particle chains. For 2D uniform granular crystals, variable packing structures will be investigated to determine the effects of particle arrangement on the highly nonlinear transient wave properties. Additionally, the pulse splitting, bending, and combining through ordered granular networks of variable branching geometry will be studied. Understanding the fundamental force transmission through the described granular crystals will open a wide range of possibilities for the realization of increasingly complex structured granular material design.

Chapter 2

Methods

The primary focus of this work is the experimental testing of the dynamic behavior of ordered granular materials. Additionally, numerical simulations were performed in order to compare with experimental results and to aid in the design phase. This chapter describes the general experimental setup and procedure as well as the discrete particle model used to numerically simulate the dynamic response of the granular systems. Additional specific details will be given in later chapters where necessary.

2.1 Nature of Stress Waves in Granular Media: Length and Time Scale Considerations

The stress wave propagation through granular systems is a multi-scale phenomenon. An intermediate length scale can be defined by the individual particle sizes comprising the macroscopic granular material, such as the radius R of a collection of spherical particles. However, the energy transfer between particles occurs over a much smaller inter-particle contact area of radius a . From the Hertzian potential described in Chapter 1, the contact area of radius a can be described by $a^3 = 3FR(1-\nu^2)/2E$, within the elastic regime. For example, for two 19.05 mm ($3/4$ inch) - diameter stainless steel spheres, such as the ones commonly used in these experiments, under a $F = 50$ N compressive force, $a/R \approx 0.02$, which relates to a radial compression of $\delta < 5\mu\text{m}$. Defining an effective strain as the compression δ with respect to the particle diameter d , a 50 N compressive force results in $\delta/d \approx 2e^{-4}$. In the dynamic regime, a traveling

stress wave with force amplitude 50 N, corresponds to a contact time of ≈ 0.2 ms between this stainless steel sphere pair. The comparatively “soft” particle contacts with respect to the bulk material stiffness of each particle causes excitations to travel much slower than the bulk material sound speed. Again, for the stainless steel sphere example, a solitary wave (with a 50 N amplitude) in a one-dimensional particle chain will travel at approximately 500 m/s, compared to the bulk sound speed $c \approx 5000$ m/s for stainless steel.

2.2 Experiments

Based on the nature of the traveling stress waves, we chose to use either custom fabricated sensor particles to measure individual particle motion within the system, or dynamic load cells to measure the response along the edge of the granular system. The use of these sensors allows for instantaneous and accurate measurements of the response of individual particles in the granular crystals. As discussed in Chapter 1 and Section 2.1, the timescale of the transient wave motion depends on the size and material properties of the particles composing the granular system. Using relatively large particles in experiments has two main advantages: (1) it allows for larger impact forces, while remaining in the elastic regime, which require less sensitive measurements and (2) it reduces the frequency content of the traveling wave pulses, which is better suited for the piezoelectric sensors used, i.e., remains below the resonant frequency of the piezo-sensors. However, since the wavelength is set by the particle size (recall the solitary wave length is always ≈ 5 particle diameters), the physical phenomenon observed in experiments will scale with the systems size, for all length scales where the Hertzian assumptions are valid.

A diagram of the complete experimental assembly is shown in Figure 2.1. The piezoelectric sensors required a signal conditioner (PCB 481A02) before being connected with the data acquisition board (NI BNC-2110 and NI PCI-6123 with simultaneous sampling rate up to 500 kS/s). The data acquisition was controlled through MATLAB, where the recorded voltage measurements for each experiment were trig-

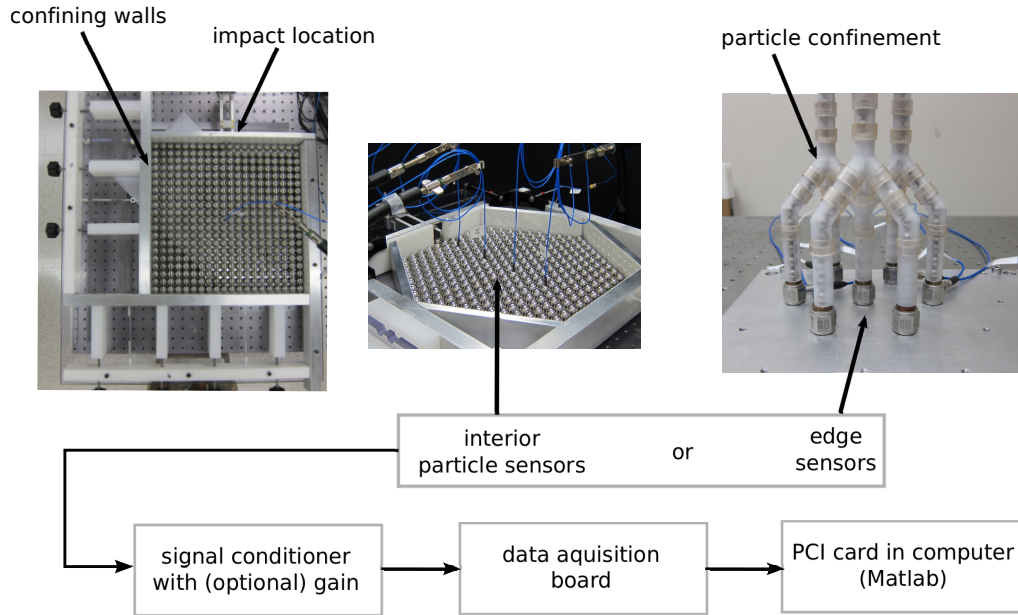


Figure 2.1: Experimental configuration

gered by selecting a trigger sensor and continued for a predetermined time frame.

2.2.1 Assembly of Granular Systems

Experiments on two-dimensional granular arrays required hand assembly of the individual grains composing the crystal structure. The particle assemblies did not use a matrix and instead relied on a confining box composed of a flat polycarbonate bottom and adjustable confining walls, in order to maintain the predefined particle structure. As seen in Figure 2.1 Left and Middle, the a wall confinement was either square or hexagonal in order to accommodate different particle arrangements. Since this work is concerned with only the primary traveling excitation, a “soft” wall material, delrin (see Table 2.1), was chosen in order to delay reflections from the system edges. The entire system could be tilted in order to achieve better particle alignment.

For more complex granular assemblies, such as those in Chapters 6 and 7, supporting channel structures were fabricated with the Connex 500 3D printing system [4], see also Figure 2.1 Right. The supporting structures were fabricated using the VeroClear material provided by Connex in the digital material printing mode.

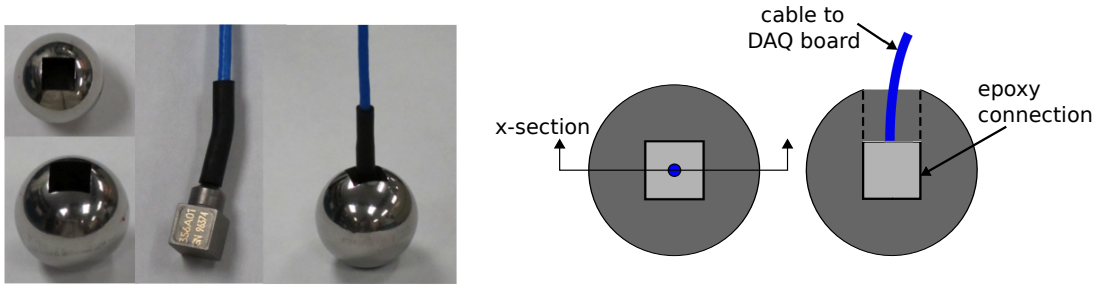


Figure 2.2: Custom fabricated sensor particles: (Left) Photographs of cut sensor sphere, sensor, and assembled sensor particle. (Right) Schematic diagram of the assembled sensor particle: top view and cross section view. The accelerometer is a 6.35 mm cube and the sphere is 19.05 mm in diameter.

2.2.2 Interior Measurements: Custom Fabricated Accelerometer Sensor Particles

Sensor particles used in previous studies to measure the motion of individual particles in granular systems, were only one-dimensional and required cutting and reassembling of solid particles [38, 39, 61, 64]. In this work, we designed and validated the use of new custom fabricated sensor particles that allow for multidirectional measurements and also preserve the outer profile of the particles. These sensor particles consisted of a sphere with a central hole drilled in order to embed a pre-calibrated miniature tri-axial accelerometer (PCB 356A01 with sensitivity $0.51 \text{ mV}/\text{m}/\text{s}^2$).

The use of accelerometers embedded inside selected particles did not alter the Hertzian contact between the sensor particles and their neighboring elements. However, the average mass of the solid stainless steel spheres was 28.79 g, whereas the average mass of the assembled sensor particles was 26.52 g (approximately 92% of the solid sphere mass). Experimental and numerical simulation studies of mass defects in a one-dimensional, uncompressed chain of spheres have shown the presence of a localized mode as a result of traveling solitary waves interacting with a light mass intruder [61]. We performed systematic numerical simulations and experiments to determine the effect of the mass difference and the influence of the sensor particles on the propagation of the impulses in a one-dimensional model system.

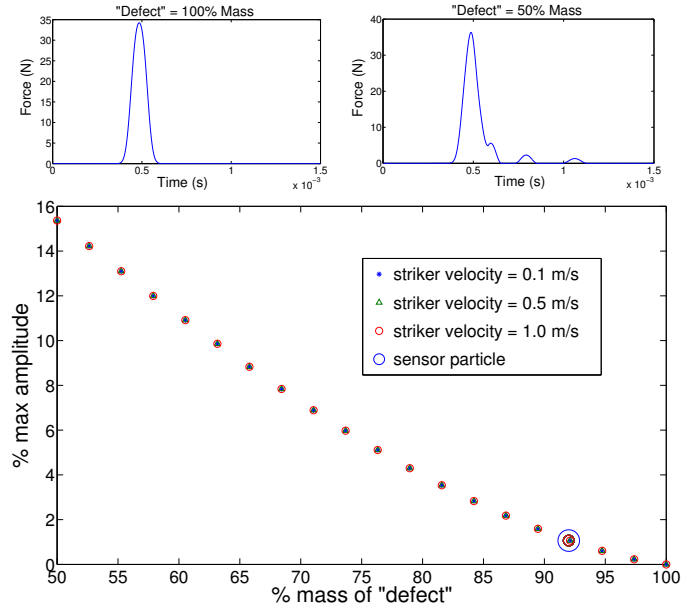


Figure 2.3: Top: Response at the “defect” particle, central particle in a chain of 20 spheres, when its mass is 100% (Left) and 50% (Right) of the solid sphere mass. Bottom: Relative amplitude of the largest reflection felt at particle the “defect” particle for various mass ratios. The x-axis is a ratio of the mass of the “defect” particle over the mass of a solid stainless steel sphere. The y-axis is the ratio of the amplitude of the largest reflection to the amplitude of the incident solitary wave. The systems relative response is independent of striker velocity.

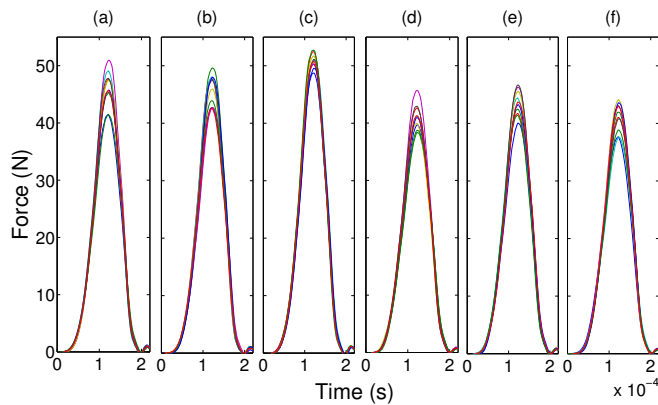


Figure 2.4: Force at the wall for a chain of 20 spheres with and without sensor particles. The baseline test configuration (a) consists of a chain of 20 solid stainless steel spheres. Force at the wall when sensor particles replace the (b) 6th, (c) 11th, (d) 16th, (e) 11th and 16th, and (f) 6th, 11th, and 16th solid spheres. The ten impacts for each test configuration are all shown.

Numerical simulations (refer to Section 2.3.1 below) were performed on a horizontal chain of 20 stainless steel particles impacted by an identical striker particle and bounded by a soft (delrin) wall at the far end. The mass of the 10th particle, or “defect” particle, was then varied from 50% to 100% of the solid (19.05 mm diameter) stainless steel sphere mass, while keeping the radius constant. As the mass of the “defect” particle was decreased, a series of reflected waves around the light mass defect begin to emerge and grow in amplitude. Figure 2.3 shows the percent amplitude of the largest reflection (compared to the incident solitary wave) at the tenth particle for various masses. It was determined that for an 8% mass reduction, as the one present in our experimental system with stainless steel sensor particles, the amplitude of the largest reflection was less than 1.2% of the incident solitary wave amplitude. Since this reflection amplitude is potentially near the noise level observed in experiments (depending on the magnitude of excitation) it is reasonable to consider this phenomenon as having a negligible effect.

To confirm this hypothesis, we performed an experimental study to determine the effect of the sensor particles replacing solid spheres. A nearly horizontal one-dimensional chain of 20 stainless steel spheres was assembled between two polycarbonate guide rails. A slight tilt (less than 5 degrees) was induced to ensure contact between all spheres. The chain was impacted by a striker particle, identical to those in the chain. The striker sphere was impacted by a solenoid to give it a repeatable initial velocity. At the far end of the chain, a dynamic load cell (PCB 208C02 with sensitivity 11241 mV/kN) was placed in between a heavy mass aluminum block and the last particle. The baseline response (the case of no sensor particles) at the end of the chain was then compared with the force at the wall when sensor particles replaced the (a) 6th, (b) 11th, (c) 16th, (d) 11th and 16th, and (e) 6th, 11th, and 16th solid spheres. The experiment was repeated ten times for each configuration (see Figure 2.4). No measurable variation in wavelength was seen and no clear trend was observed in the variation of wave amplitude at the wall when sensor particles were introduced in the system. In conclusion, there was no clear indication that the sensor particles measurably altered the response of the system, validating their use for

additional studies.

2.2.3 Edge Measurements: Dynamic Load Cells

In some cases, dynamic force measurement were taken along the edge of the granular system with piezoelectric dynamic force sensors (PCB 208C01 and PCB 208C02, with sensitivity 11.2 mV/N and 112.4 mV/N), with stainless steel impact caps. Previous studies have also validated the use of edge measurements for analyzing the behavior within granular media [31, 32, 35, 95, 124]. For increasingly complex particle assemblies, the use of edge sensors in place of the interior sensor particles provided several advantageous. When testing granular systems with increasing number of particles, smaller particles are required to make the granular system physically feasible to assemble and test, and the accelerometers limit the minimum particle size. Additionally, for three-dimensional systems, the cables connecting sensor particles to the data acquisition interfere with the complex particle confinement for interior measurements.

Previous studies have shown that the force amplitude at a wall, or rigid sensor, is higher than the solitary wave amplitude traveling through the chain of particles [5, 64]. We used the theoretical prediction described by [64], to relate the force amplitude of the edge particle-sensor interaction to the force between particles within the granular chains. For the case of identical wall and particle materials, $F_{\text{chain}} = F_{\text{sensor}}/1.7$.

2.2.4 Discussion of Alternate Experimental Techniques

Digital image correlation (DIC), laser vibrometry, and photoelasticity were also investigated as potential measurement techniques. These methods were initially appealing because of their non-contact nature. However, the nature of the traveling stress waves through the granular systems of interest rendered these techniques disadvantageous for recording the transient wave motion.

The difficulties using DIC were based on the camera resolution. Since the particle displacements are on the order of several microns (refer to Section 2.1), the high-speed camera had to be used in conjunction with a microscope to successfully capture

the motion. Therefore, only a single particle motion could be tracked during each experiment or impact, requiring repeated impacts with variable camera locations, which heavily relies on the repeatability of experiments. This repeatability issue in combination with the time intensive data analysis of each experiment were reason to not further consider the use of DIC for data collection.

The laser vibrometry had similar spatial resolution or repeatability issues as with the DIC, since only a single particle motion can be tracked at a time. Additionally, multiple lasers are required to measure multidirectional responses. While multidirectional laser scanning systems are currently available, the scanning speed is insufficient to capture the transient motion from a single impact, thus these scanning systems are more applicable for experimental investigation of continuously excited systems.

Several previous studies of the static and dynamic load transfer in granular assemblies have made use of photoelastic particles [47, 108, 111, 114, 145, 147]. However, this method again requires significant post-processing in order to obtain two-dimensional measurements. More importantly, the use of photo elasticity is best suited for material samples with a constant thickness, such as elliptical or round cylinders [111, 145] in the case of granular media. The light refraction due to the curvature of the spheres prevents light from passing directly through the sphere edges, which is the locations of stress concentrations, and thus the location of the fringes. Using cylindrical particles changes the fundamental contact law between the grains, from the highly nonlinear, Hertzian, one of interest; two (parallel) cylinders in compression create in a line contact instead of a point contact, resulting in a nearly linear force-displacement relation [26, 161].

2.3 Numerical Simulations

Following the work of Cundall and Strack [162], discrete particle models have been extensively used to numerically simulate the dynamic behavior of granular materials (see the review by Sen [163] for examples). This approach models particles as point

masses connected by nonlinear springs. It is assumed that disturbances only travel to the nearest neighbor in a single time step, thus the equation of motion for each particle can be independently solved at each time step.

2.3.1 Discrete Particle Model

The three-dimensional numerical simulations performed for this work are based on a conservative discrete particle model where the linear elastic Hertzian potential is used for the nonlinear springs [26]. The repulsive force F_{ij} between neighboring spheres i and j evolves as a power law $\delta_{ij}^{3/2}$ of their penetration distance. We used a 4th order Runge Kutta scheme to integrate the following system of equations, consisting of:

$$m_i \ddot{\mathbf{u}}_i = \sum_{j=1}^P \mathbf{F}_{ij} = \sum_{j=1}^P K_{ij} |\delta_{ij}|^{3/2} \hat{\delta}_{ij}, \quad (2.1)$$

$$\delta_{ij} = ((R_i + R_j) - |\mathbf{r}_{ij}|) \hat{\mathbf{r}}_{ij} \quad \text{where } \mathbf{r}_{ij} = [(x_j - x_i) \ (y_j - y_i) \ (z_j - z_i)] \quad (2.2)$$

for each particle i . In these equations, m is the particle mass, $\mathbf{u}_i = [u_{ix} \ u_{iy} \ u_{iz}]$ represents the particle x , y , and z displacement from equilibrium and P is the number of neighboring particles. K_{ij} is the contact stiffness between two particles i and j and δ_{ij} is the penetration distance between two particles. To capture the tensionless behavior, δ_{ij} takes a zero magnitude when particles i and j are not in contact. The stiffness coefficient for two spherical particles (i and j) in compression can be described by:

$$K_{sphere_i, sphere_j} = \frac{4}{3} A_{i,j}^{-1} \left(\frac{R_i R_j}{R_i + R_j} \right)^{\frac{1}{2}} \quad (2.3)$$

where R is the radius of each sphere and $A_{i,j} = \left(\frac{1-\nu_i^2}{E_i} + \frac{1-\nu_j^2}{E_j} \right)$. In the case of a sphere and cylinder in compression, the same $3/2$ power law remains valid, but with a slightly

Material	Mass Density ρ (kg/m^3)	Young's Modulus E (GPa)	Poisson's Ratio ν
Stainless Steel (type 316)	8000	193	0.30
(type 440C)	7800	200	0.28
Aluminum	2700	68.9	0.33
Delrin	1400	3.1	0.35
Polytetrafluoroethylene (PTFE)	2200	0.5	0.46
Polycarbonate	1200	2.3	0.37
VeroClear	1045	2.5	0.35

Table 2.1: Material Properties [1–4]

modified stiffness coefficient:

$$K_{sphere_i,cylinder_j} = \frac{2}{3}\pi A_{i,j}^{-1} (2eR_i)^{\frac{1}{2}} K^{\frac{2}{3}} \quad (2.4)$$

where e and K are tabulated functions of the sphere and cylinder radii, R_i and R_j , and can be found in [161]. Walls were modeled as immovable spherical particles with an infinite radius. To excite the system, a single particle, corresponding to the impacting or striker particle in experiments, was given an initial velocity.

While the numerical simulations allow for the inclusion of gravity, the effects were negligible for the systems studied here [164] and gravitational forces were generally omitted. As described in [5], for example, the integration time step was chosen to strike a balance between computational accuracy and required simulation time. The material properties used in subsequent numerical simulation are given in Table 2.1.

The acceleration output from the sensor particles can be directly compared with the acceleration of the center of mass of each particle obtained from the numerical simulations. In subsequent chapters, the average force on particle i is calculated as:

$$F_i = \left(\left(\frac{\sum_j |\mathbf{F}_{ij} \cdot \hat{\mathbf{x}}|}{2} \right)^2 + \left(\frac{\sum_j |\mathbf{F}_{ij} \cdot \hat{\mathbf{y}}|}{2} \right)^2 + \left(\frac{\sum_j |\mathbf{F}_{ij} \cdot \hat{\mathbf{z}}|}{2} \right)^2 \right)^{1/2} \quad (2.5)$$

in numerical simulations to compare with the F_{chain} force (calculated from F_{sensor})

measured in experiments.

2.3.1.1 Rotational and Dissipative Considerations

In addition to the normal, Hertzian, contact interaction between particles, Mindlin derived a corresponding tangential force-displacement relationship in the presence of friction [165, 166]. The incorporation of this history dependent tangential contact law significantly increases the complexity of the discrete particle framework [121, 167]. For one-dimensional particle chains, it is reasonable to neglect the rotational motion since lateral forces do not arise based on the single line of contact between the particle centers of mass. By extension, the effects of rotation on the overall dynamic behavior in densely packed ordered higher-dimensional systems is minimal, and results in a slight dissipation of the leading pulse amplitude [121]. Rotational effects, however, may play a larger role in the dynamic behavior of vibrated, compressed (i.e., linear or weakly nonlinear) granular crystals [90, 99, 100, 102, 168]. For the ordered, densely packed, and highly nonlinear granular systems studied here, we have chosen to neglect the rotational motion in order to simplify the numerical simulations.

A number of different models have been used to capture the dissipation observed in experiments, as a result of friction, viscoelasticity, viscous drag [42, 64, 163, 169–172]. However, these models rely on experimentally fitted parameters, making them less attractive for general use. Additionally, multiple wave reflection within particles could result in significant amplitude decay [173]. Recently the amplitude loss observed in experiments has been attributed to energy trapped in vibrational modes of individual particles [174], only requiring the particle material and geometry for input. Previous studies included an elastic-perfectly plastic material response for homogeneous particle assemblies [175], and more recently, efforts are being made to understand the elasto-plastic response of non-homogeneous sphere pairs [176]. This work, however, is focused on the linear elastic regime, and all experiments and corresponding numerical simulations were performed with impact velocities low enough to avoid plastic deformation [26, 35]. In general, the source and effects of dissipation in granular systems proves to be an ongoing topic of research, which is considered outside the scope of

this work. We assume that the effects of dissipation do not substantially alter the basic wave propagation pathways, but primarily decrease the wave amplitude.

2.3.1.2 Weak Disorder Simulations

In several chapters, numerical simulations incorporating weak disorder were also performed to determine the effects of slight particle imperfections and misalignments on the wave propagation pathway compared to the ideal, or non-random, particle array. To describe the variation in particle diameters numerically, a normal random distribution was chosen around the mean value specified by the manufacturer. We assumed tolerance values corresponded to 6 standard deviations, which is a common statistical interpretation for mechanical tolerances [177].

To compute the initial configuration for each realization (each initial contact lattice), a set of normally distributed random diameters for cylindrical and spherical granules was randomly assigned to the particles of the non-random crystal. Mismatching radii placed on perfect lattice sites cause some contacts to separate and others to compress. To achieve an equilibrated starting configuration, the initial resting positions of the particles in the weakly disordered lattice was found in two steps. First the particles were given an even lattice spacing assuming $d = d + tol$, to avoid large repulsive forces between overlapping particles. To bring the particles in contact, a 5N force was applied to each of the edge particles and an artificial damping (of the form [170]) was used to settle the random particle motion. Secondly, the wall positions were found based on the slightly compressed settled configuration, gravity was introduced accordance with the experimental tilt, the 5N force was removed, and the particles were again settled through a similar, but weaker damping process. Once the initial positions were obtained, the settled array was impacted with a striker sphere. For the subsequent discussion, we will use the terms “ideal” and “weakly disordered” to distinguish between numerical simulations where the spheres are all assigned the same diameter, and those just described.

2.3.1.3 Additional Numerical Simulations

In some sections, the numerical simulations were carried out by collaborators, using either the granular module [178] of the LAMMPS molecular dynamics (MD) package [179] (A. Aswathi [120]), or an analogous procedure to the one described above (C. Chong). In both cases, the outputs from their numerical simulations were compared with test cases of the numerical simulations described above, ensuring equivalent dynamic responses for the granular systems.

Chapter 3

2D Granular Crystals: Square

We study the dynamic response of a two-dimensional (2D) square packing of uncompressed stainless steel spheres excited by impulsive loadings. Experiments employ miniature tri-axial accelerometers, to determine the stress wave properties in the array resulting from both an in-plane and out-of-plane impact. Results from our numerical simulations, are in good agreement with the experimental results. We observed that the impulsive excitations were resolved into solitary waves traveling only through initially excited chains, as predicted by Nesterenko [5]. The observed solitary waves were determined to have similar (Hertzian) properties to the extensively studied solitary waves supported by an uncompressed, uniform, one-dimensional chain of spheres. The highly directional response of this system could be used as a basis to design granular crystals with predetermined wave propagation paths capable of mitigating stress wave energy.

3.1 Problem Description and Approach

The granular crystals studied in this chapter consisted of a 20 by 20 square packing of stainless steel spheres, confined but not compressed by the setup described in Chapter 2. In order to achieve a uniform contact lattice, a slight tilt ($< 5^\circ$) was applied to both the X - and Y -directions. Two different impact conditions were considered: (1) in-plane, where the array was impacted between the two middle particles along the edge, and (2) out-of-plane, where the array was impacted between the four spheres

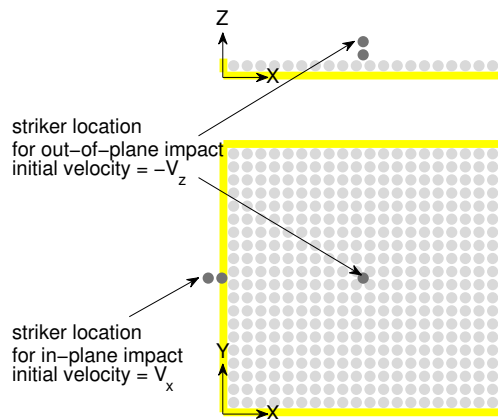


Figure 3.1: Schematic diagrams of the test configurations: (Top) view of the setup from the side, showing the position of the striker spheres (dark grey) and (Bottom) view of the setup from the top. The square array was a 20 by 20 packing of 19.05 mm diameter spheres. For the in-plane impacts, the striker sphere impacted the resting striker sphere in contact with edge particles X_1Y_{10} and X_1Y_{11} . For out-of-plane impacts, the striker sphere impacted the resting striker sphere in contact with central particles $X_{10}Y_{10}$, $X_{11}Y_{10}$, $X_{10}Y_{11}$, and $X_{11}Y_{11}$.

at the center of the array (see Figure 3.1). The system was excited impulsively by a stainless steel striker sphere, identical to the particles composing the crystal, impacting a resting striker sphere in direct contact with the array. The presence of the resting striker sphere allowed us to achieve a more repeatable, uniform impact compared to the striker sphere directly impacting the array. For the in-plane impacts, a solenoid was used to impact the striker sphere, giving it a repeatable initial velocity. The striker's velocity was measured with an optical interrupter just before impacting the system. For the out-of-plane impacts, the striker sphere was dropped from some known height (through guide rails), and its initial velocity was calculated from the drop height.

Custom fabricated sensor particles (Section 2.2.2) replaced solid spheres at selected locations in the system to measure individual particle motion. The acceleration output from the sensor particles was directly compared with the acceleration of the center of mass of each particle obtained from the numerical simulations. The recorded experimental measurements were triggered when the excitation reached the

first sensor particle. In numerical simulations the zero time represents the moment of striker impact. In order to compare experimental data with numerical simulations the experimental zero time was obtained using the measured wave speed and the known distance of the first sensor from the impact. Additional experiments were then performed for a variety of impact velocities in order to determine the amplitude - wave speed relationship and the wavelengths of the traveling pulses. We used experimentally measured impact velocities as input in the simulations. The material properties used in numerical simulations the calculations can be found in Table 2.1.

3.2 Wave Propagation Path

When the square array was impacted in-plane, we observed solitary waves traveling through four chains: one through each of the two central chains and one through each of the two edge chains (Figure 3.2). Numerical simulations revealed that of the total energy input into the system (by the striker sphere initial velocity), 71.5% went into the solitary waves traveling in the two central chains along the impact direction, and 24.5% into the waves traveling transversely through the edge chains. The remaining energy was lost in the rebounding of the striker spheres and the particles nearest the impact. Experiments were repeated 15 times for each sensor configuration, with an average striker velocity of $V_x = 0.29$ m/s. Figure 3.3 describes the motion of the particles in the two central chains and Figure 3.4 describes the motion of the particles in the two edge chains resulting from the in-plane impact.

To capture the waves traveling through the central chains after the in-plane impact, sensors 1A and 1B were located six particles from the impact in each of the two central chains. Additional sensors were placed in one of the central chains at ten and fifteen particles from the impact (sensors 1C and 1D in Figure 3.3a). Figure 3.3b compares the experimental acceleration recorded at these sensor locations with those obtained from numerical simulations. Due to the systems symmetry, we expected an identical response for sensors 1A and 1B in the central chains. However, slight variations in signal arrival times and amplitudes were observed in experiments. These

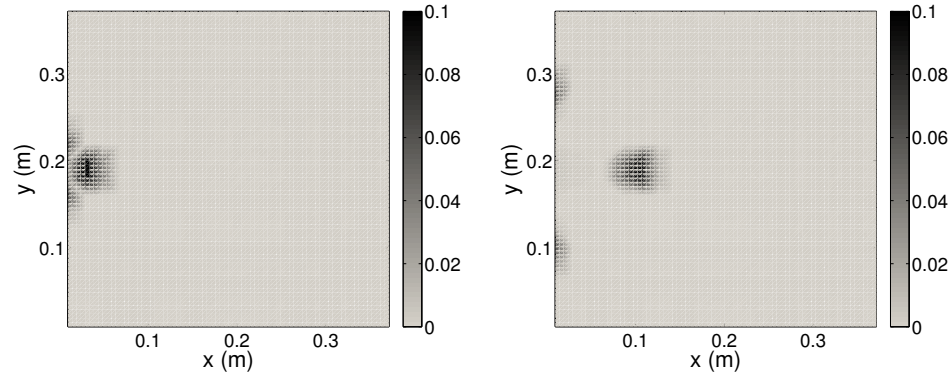


Figure 3.2: Density plots corresponding to the amplitude of the particle velocity obtained from numerical simulations as a function of spatial position in the granular crystal. (Left) At 0.15 milliseconds and (Right) at 0.30 milliseconds after the array was impacted in-plane with a striker velocity $V_x = 0.29\text{m/s}$. The grey-scale indicates the particle velocity amplitude in m/s.

variations were most likely an effect of imperfect striker impacts. If the striker does not impact each of the two edge spheres simultaneously (because of slight misalignment) the result should be a slight time delay and uneven force transmission between adjacent chains, similar to what was observed in experiments. In the central chain, the difference in time of arrival of peak particle acceleration ($t_{peak}(1B) - t_{peak}(1A)$) was $-21(\pm 68)$ microseconds and the percent difference in peak acceleration of sensor 1A with respect to sensor 1B was $4\%(\pm 10\%)$. The experimental results shown in Figure 3.3b best represent the average response of the system from the 15 repeated experiments (i.e., this signal most closely represent the mean values for both peak arrival time and percent amplitude of the mentioned sensor pairs).

To capture the waves traveling transversely through the two edge chains after the in-plane impact, sensors 2A and 2B were placed five particles from the impact in each of the two edge chains and another sensor was placed in one of the edge chains at eight particles from the impact (2C in Figure 3.4a). Additionally, we placed a sensor particle several diameters away from the waves traveling through both the central and edge chains (sensor 2D in Figure 3.4b) to determine if existing imperfections in the granular crystal allowed for deviations from the expected wave propagation paths. For the edge chains, the difference in time of arrival of peak particle acceleration

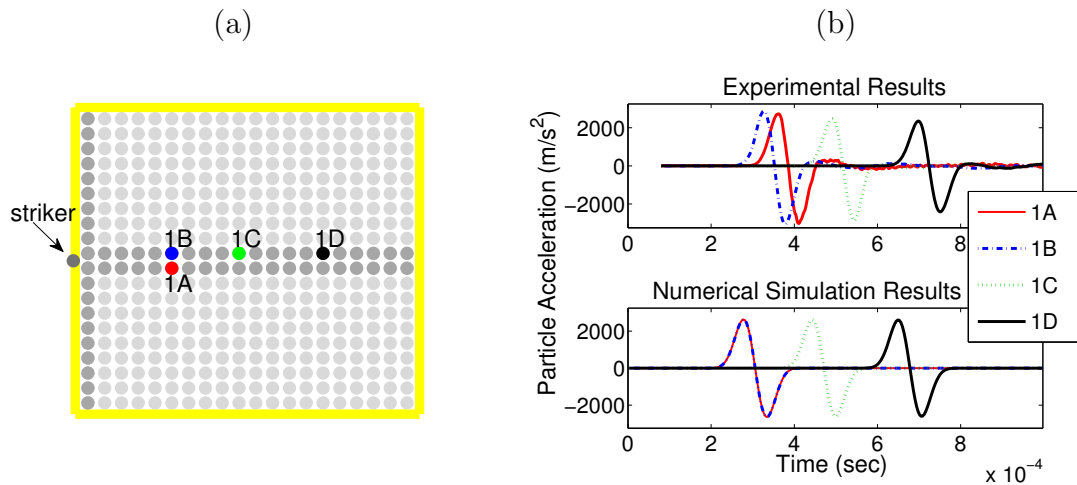


Figure 3.3: Experimental and numerical simulation responses of the two central chains in the granular crystal resulting from an in-plane impact. (a) Schematic diagram showing the experimental setup and the positions of the sensor particles (shaded spheres indicate particles excited by the impulse). (b) Signals recorded at the sensor locations. The top panel represents experimental results and the bottom panel the numerical simulations. In both experiments and simulations each particle's acceleration in the x-direction is plotted as a function of time. The experimental y-acceleration was nearly zero for all sensor locations (zero in simulations) and was therefore not plotted.

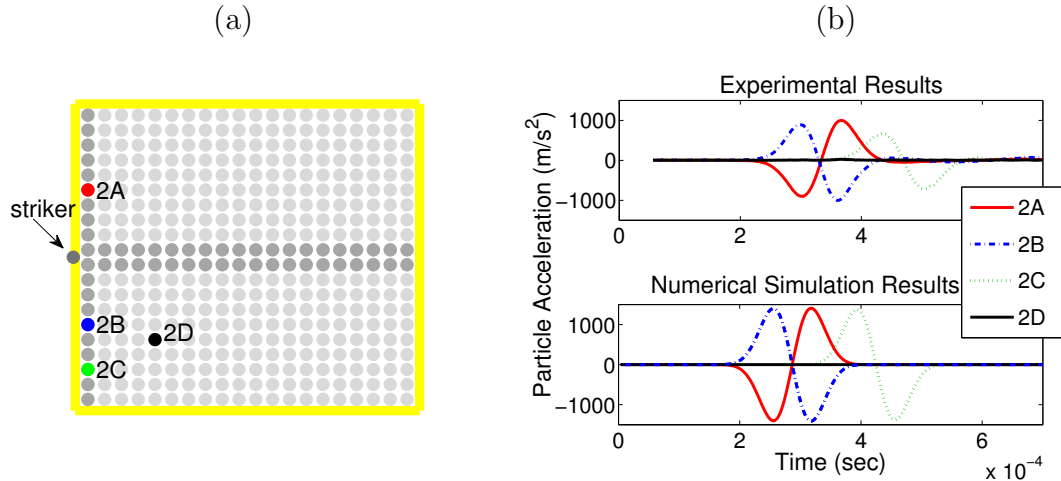


Figure 3.4: Experimental and numerical simulation responses of the two edge chains in the granular crystal resulting from an in-plane impact. (a) Schematic diagram showing the experimental setup and the positions of the sensor particles (shaded spheres indicate particles excited by the impulse). (b) Signals recorded at the sensor locations. The top panel represents experimental results and the bottom panel the numerical simulations. In both experiments and simulations the particle's acceleration obtained from sensors 2A, 2B, and 2C in the negative y -direction is plotted as a function of time. The experimental x -acceleration was nearly zero for all sensor locations (zero in simulations) and was therefore not plotted. The signal plotted for sensor 2D includes the total magnitude of the x - and y -particle acceleration.

$(t_{peak}(2B) - t_{peak}(2A))$ was $-0.50(\pm 6.5)$ microseconds and the percent difference in peak acceleration of sensor 2A with respect to sensor 2B was $-7\%(\pm 18\%)$. The experimental results shown in Figure 3.4b best represent the average response of the system from the 15 repeated experiments in terms of the relative arrival times and amplitudes at sensor locations 2A and 2B. We observed, as expected, that the sensor away from the traveling waves (sensor 2D) was not measurably excited by the impact (Figure 3.4).

Experiments and numerical simulations were performed also for crystals excited by out-of-plane impacts. Results from this analysis are reported in Figures 3.5 and 3.6. In this configuration, we observed identical solitary waves traveling through the 8 central chains of the granular crystal, forming cross-shaped propagation beams (Figure 3.5). Numerical simulations revealed that of the total energy input into the system (by the striker sphere initial velocity), 44.3% went into the solitary waves

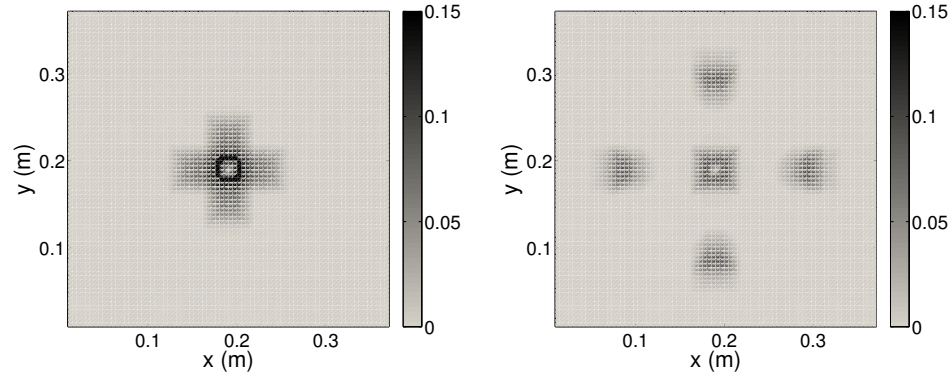


Figure 3.5: Density plots corresponding to the amplitude of the particle velocity obtained from numerical simulations as a function of spatial position in the granular crystal. (Left) At 0.15 milliseconds and (Right) at 0.30 milliseconds after the array was impacted out-of-plane with a striker velocity $V_z = -0.65\text{m/s}$. The grey-scale indicates the particle velocity amplitude in m/s.

traveling in the eight central chains, 8.0% was lost in the rebounding of the striker particles, 47.7% was lost in the rebound of the four initially impacted central spheres. Sensors 3A and 3B were placed six particles from the out-of-plane impact in two of the central chains and sensor 3C was located eight particles from the impact in one of the central chains (Figure 3.6a). To determine if existing experimental imperfections in the granular crystal allowed for deviations from the expected wave propagation paths, we positioned an additional sensor (sensor 3D in Figure 3.6a) five particles away from the central chains of the crystal. Experiments were repeated 15 times, with an average striker velocity of $V_z = -0.65\text{m/s}$. The particle acceleration measured by the sensors and their motion was compared with numerical simulations (Figure 3.6).

Slight variations in solitary wave amplitudes and arrival times were again observed between adjacent spheres in experiments. The difference in time of arrival of peak particle acceleration ($t_{peak}(3B) - t_{peak}(3A)$) was on average $25(\pm 54)$ microseconds and the percent difference in peak acceleration of sensor 3A with respect to sensor 3B was $1\%(\pm 42\%)$. The experiments plotted in Figure 3.6 most closely represent the average response of the system. As with the in-plane impact, we observed that the sensor away from the traveling waves was not measurably affected by the waves

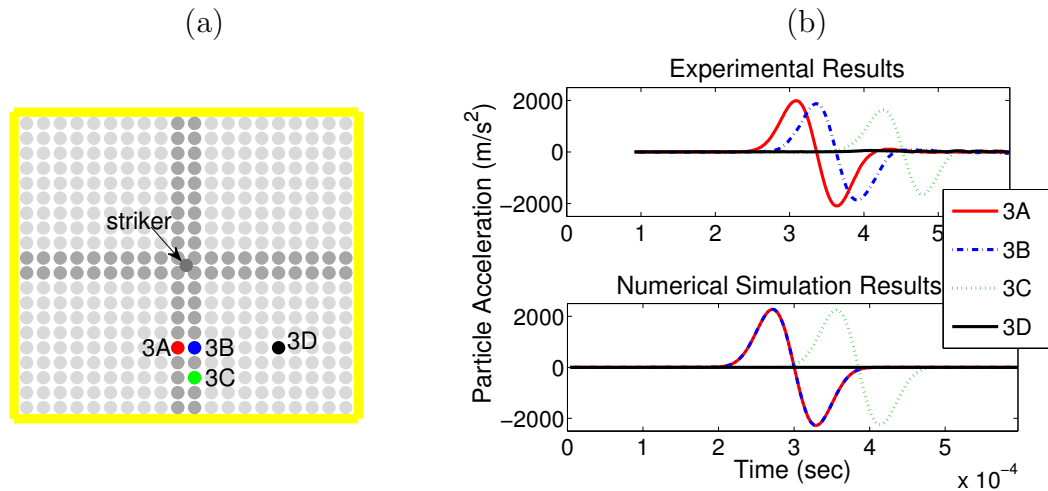


Figure 3.6: Experimental and numerical simulation responses of the central chains in the granular crystal resulting from an out-of-plane impact. (a) Schematic diagram showing the experimental setup and the positions of the sensor particles (shaded spheres indicate particles excited by the impulse). (b) Signals recorded at the sensor locations. The top panel represents experimental results and the bottom panel the numerical simulations. In both simulations and experiments the particle's acceleration in the negative y-direction is plotted as a function of time. The experimental x-acceleration was nearly zero for all sensor locations (zero in simulations) and was therefore not plotted. The signal plotted for sensor 3D includes the total magnitude of the x- and y-particle acceleration.

traveling in the central chains. The lack of particle motion at sensors 2D (Figure 3.4) and 3D (Figure 3.6) and the good agreement with simulation and experimental results indicate that any existing deviations from the granular crystal's ideal contact lattice were not significant enough to leak energy from excited chains or to prevent the observed solitary waves from forming. This is in agreement with experimental studies on square packings of circular and elliptical disks by Shukla et al., where deviations from the highly directional response are visually observed to be minimal [110–112, 114].

The presence of dissipation is evident in the experimental results. This leads to an observable discrepancy in the wave amplitude between the signal recorded in experiments and in numerical simulations (that do not include dissipative losses). In highly nonlinear systems, the wave propagation speed is a function of the wave amplitude. As a consequence, the noticeable travel time difference observed between

the pulses recorded experimentally and the ones obtained from numerical simulations can be also attributed to the signal attenuation due to dissipation. We observed significantly more dissipation in the waves traveling through the edge chains (Figure 3.4) compared with those traveling through central chains in the granular crystal (Figures 3.3 and 3.6). This difference could be attributed to the fact that edge particles are in contact with two walls (side and bottom), compared to only one wall (bottom) for internal particles, introducing more friction and increasing the rate of amplitude decay.

3.2.1 Particle Velocity – Wave Speed Scaling Relation

A scaling relation between the particle velocity and the propagating wave speed was determined by separately inspecting the waves traveling through each of the chains involved in the signal propagation. The results were compared with the scaling relationship available from the 1D highly nonlinear wave theory (refer to Section 1.2.1). To determine the experimental particle velocity, we numerically integrated the measured particle acceleration. The peak value of the particle velocity was then plotted against the calculated wave speed for a variety of striker velocities (see the points in Figures 3.7-3.9). We compared the experimental values with data computed with our discrete element model, performing simulations for different striker velocities.

The experimental peak particle velocities (Figures 3.7, 3.8, and 3.9) were calculated by averaging the peak values from the sensor pairs. The plotted experimental wave speed was calculated from the time of flight between the two sensors' peak velocities (t) and the distance between the sensor particles' centers (d). Error bars in the wave speed direction were calculated based on bead tolerances (± 0.01 mm, δd) and the sampling rate (2 microseconds between data points, δt). Since wave speed, V_s , is d/t , we can write $\frac{dV_s}{V_s} = \frac{\frac{\partial V_s}{\partial t} dt + \frac{\partial V_s}{\partial d} dd}{d/t}$ or letting $dx \rightarrow \Delta x$, we get error bars extending in each direction with length $\Delta V_s = \left(\frac{\Delta t}{t} + \frac{\Delta d}{d}\right) \cdot V_s$. In the maximum particle velocity direction, error bars were calculated based on uncertainty in the sensors' calibration factors (3%, δK) and sensor misalignment (it was conservatively assumed that sensors

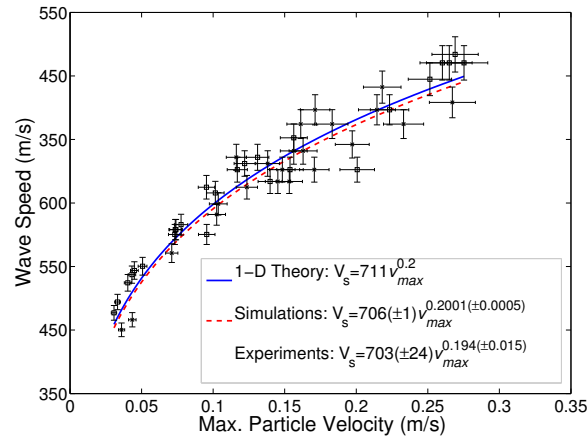


Figure 3.7: Wave speed vs. maximum particle velocity for the central chains when the system is impacted in-plane. The squares denote tests for sensor locations 1B and 1C, while the stars denote tests when sensors are moved to the adjacent chain (1A and the respective neighboring particle of 1C, location $X_{15}Y_{10}$). Results of the linear regression on the log-log data for both experiments and simulations are shown (with 95% confidence intervals).

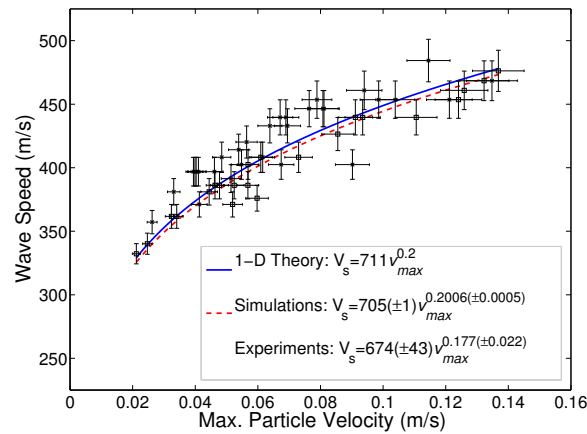


Figure 3.8: Wave speed vs. maximum particle velocity for the edge chains when the system is impacted in-plane. The squares denote tests for sensor locations 2B and 2C, while the stars denote tests when sensors are moved to the opposite chain (2A and the respective neighboring particle of 2C, location X_1Y_{18}). Results of the linear regression on the log-log data for both experiments and simulations are shown (with 95% confidence intervals).

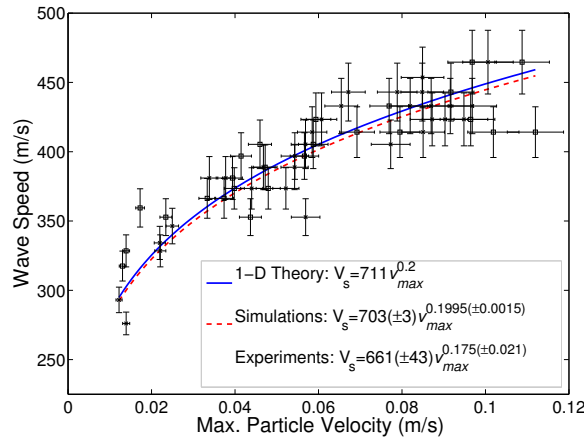


Figure 3.9: Wave speed vs. maximum particle velocity for the central chains when the system is impacted out-of-plane. The squares denote tests for sensor locations 3B and 3C, while the stars denote tests when sensors are moved to the adjacent chain (3A and the respective neighboring particle of 3C, location $X_{10}Y_3$). Results of the linear regression on the log-log data for both experiments and simulations are shown (with 95% confidence intervals).

could be aligned, by hand, within 10 degrees of the true x-, y-, and z-directions, δV). Similarly, since acceleration, a , is V/K , we can again get the integrated velocity error bar length in each direction from $\Delta a = (\frac{\Delta V}{V} + \frac{\Delta K}{K}) \cdot a$. Here V represents the measured voltage from accelerometers and K the calibration factor. The error bars did not take into account phenomenon such as the presence of gaps in the granular crystal, which could explain data points residing far from the theoretical and simulation lines.

A linear regression was performed for both numerical simulations and experimental data points (on a log-log scale) to determine the amplitude-wave speed relationship for traveling waves due to both the in-plane and out-of-plane impacts (Figures 3.7, 3.8, and 3.9). We observed that the wave behavior in this simple two-dimensional system generally follows the same $V_s \propto v_{max}^{1/5}$ relationship that was derived for one-dimensional systems.

3.2.2 Pulse Length

The wavelength of the observed solitary waves was calculated by separately inspecting the waves traveling through each of the chains described above. In experiments, we

calculated the solitary wave length following two approaches. The values obtained were then compared with one-dimensional theoretical values. In the first approach we fit the experimental signals to the theoretical 1D waveforms (refer to Section 1.2.1). In the second approach, we directly calculated the wavelength at half maximum amplitude (full width at half maximum values).

From Nesterenko's one-dimensional theory the particle velocity profile in a highly nonlinear chain of spheres approximately follows Equation 1.3, thus the acceleration profile follows $a = V_s \left(\frac{5V_s^2}{2c^2}\right)^2 \frac{\sqrt{10}}{10R} \cos^3\left(\frac{\sqrt{10}}{10R}x\right) \sin\left(\frac{\sqrt{10}}{10R}x\right)$. The normalized experimental acceleration data was fit (in a nonlinear least squares sense) to the waveform, $a = \cos^3\left(\frac{2\pi(t-t_o)}{\lambda}\right) \sin\left(\frac{2\pi(t-t_o)}{\lambda}\right)$, with fitting parameters t_o and λ , and the solitary wavelength was then calculated as $\lambda/2$. For comparison, the integrated velocity profiles were also fit to the more familiar $v = \cos^4\left(\frac{2\pi(t-t_o)}{\lambda}\right)$ waveform, and the wavelength was again calculated as $\lambda/2$. The comparison with one-dimensional theory, numerical simulations, and experiments of the fitted wavelength can be seen in Figure 3.10 (a) and (b). The comparison of wavelength at half maximum amplitude for one-dimensional theory, numerical simulations, and experiments can be seen in Figure 3.10 (c) and (d), where the full width at half maximum values of the acceleration and velocity waveforms are plotted as a function of distance from impact, respectively.

In general, the experimental wavelengths are in reasonable agreement with the numerical simulations. There is a clear discrepancy between the theoretical wavelength (based on the wave shape given by Equation 1.2), and the stabilized waveform from numerical simulations. However, a similar decrease (approximately 13%) in the full width at half maximum values can also be seen when comparing Chatterjee's [34] asymptotic solution for the shape of the solitary wave with Nesterenko's theory (Equation 1.3). In simulations, it appears that the wave reaches a stable waveform after traveling through roughly five or six particles from the impact location. In experiments, the pulse temporal length is observed to increase with increasing distance from the point of impact. This effect can be related to the presence of dissipation.

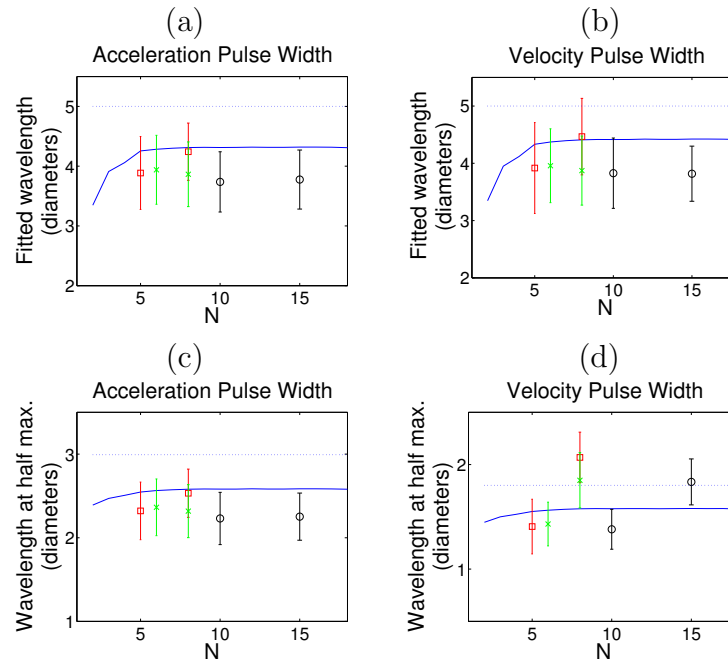


Figure 3.10: Wavelength of the solitary wave as a function of distance from the impact (N). The dotted lines represent the theoretical values from Nesterenko's long wavelength approximation and the solid lines represent a smoothed curve through simulation data. Circles represent data from sensor locations 1C and 1D (Figure 3.3) and squares represent data from sensor locations 2B and 2C (Figure 3.4) after the array was impacted in-plane. The crosses represent data from sensor locations 3B and 3C (Figure 3.6) after the array was impacted out-of-plane. (a) Wavelength calculated by fitting the acceleration curves to Nesterenko's waveform. (b) Wavelength calculated by fitting the (integrated) velocity curves to Nesterenko's waveform (Equation 1.3). (c) Wavelength at half maximum amplitude directly calculated from the acceleration profiles. (d) Wavelength at half maximum amplitude directly calculated from the (integrated) velocity data. Error bars extend two standard deviations from the mean values.

3.3 Summary of Results

We demonstrated good agreement between experimental results and numerical simulation results based on the Hertzian discrete particle model. We observed that when the two-dimensional square packing of steel spheres was impacted in-plane (between two edge particles) or out-of-plane (simultaneously impacting four central particles), the impulsive excitation was resolved into solitary waves traveling only down initially excited chains. We observed that deviations from the granular crystal's ideal contact lattice were not significant enough to prevent the formation and propagation of solitary waves, with no or minor energy lost in the excitation of adjacent chains of particles. The observed solitary waves appeared to have comparable (Hertzian) properties to the extensively studied solitary waves traveling in an uncompressed, one-dimensional chain of spheres.

Chapter 4

2D Granular Crystals: Centered Square

We investigate the propagation of elastic stress waves in an uncompressed, centered square array of spherical and cylindrical particles. We show, via experiments and numerical simulations, that systematic variations of the mass and stiffness ratios of the spherical and cylindrical particles lead to large variations in the characteristics of the propagating stress wave fronts traveling through the system. Additionally, we investigate the effects of statistical variation in the particle diameters and compare the effects of the resulting disorder in experiments and numerical simulations, finding good agreement. The ability to control the stress wave front properties in these granular systems may allow for the development of new wave-tailoring materials including systems capable of redirecting impact energy.

4.1 Problem Description and Approach

The centered square granular crystals studied in this work consisted of a square packing of spherical particles with central particles (i.e., intruders) residing in the inter-particle spaces within the square array, effectively forming an offset square packing. To simplify the experimental assembly, cylindrical particles were used as intruders. The cylindrical particles were oriented such that their longitudinal axes were perpendicular to the plane of the 2D bed. The radii of cylindrical particles (given as $r = (\sqrt{2} - 1)R$) is fixed so they touch the surrounding spheres (radii R) and their

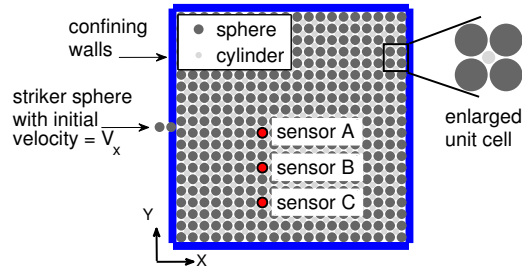


Figure 4.1: Schematic diagram of the experimental setup. The striker sphere impacted a resting striker sphere located between the 10th and 11th spherical particles along the edge. Sensors A, B, and C are located at positions X_8Y_{10} , X_8Y_7 , and X_8Y_4 of the 20 by 20 spherical square array, respectively.

height is chosen to be equal to the diameter of the spherical particles.

For experiments, and corresponding numerical simulations, the centered square granular crystals consisted of a 20 by 20 square packing of spherical particles, with intruder particles forming an interior 19 by 19 square lattice (see Figure 4.1). We performed experiments for four different sphere-cylinder material combinations: (a) steel^s-ptfe^c (b) delrin^s-ptfe^c, (c) steel^s-steel^c, and (d) delrin^s-steel^c, where the s and c superscripts denote sphere and cylinder materials, respectively. The spherical particles (from [1]) were 19.05 mm in diameter. The steel spheres had a diameter tolerance of $\pm 0.0127\text{mm}$ (0.0667%) and the delrin spheres had a diameter tolerance of $\pm 0.0254\text{mm}$ (0.1333%). The cylinders were machined to fit exactly in the interstitial spaces, with a specified diameter and tolerance of $7.8908 \pm 0.0127\text{mm}$ (0.1609%).

The 20 by 20 sphere array was excited by a striker sphere centrally impacting the granular crystal, in-plane between the 10th and 11th edge spheres. Since the mass of the impactor can influence the response of the system (causing more than one impact in the case of a heavy striker [67, 68]), the striker particles were chosen to be identical to the spherical particles in the granular crystal, either delrin or steel based on the material combination being tested. The striker sphere was given an initially velocity with a solenoid mechanism and the striker velocity was measured just before impacting the system. The average striker velocity was $V_x = 0.92\text{ m/s}$ for the delrin sphere and $V_x = 0.73\text{ m/s}$ for the steel sphere.

In order to capture the wave propagation at variable locations within the system, we collected data for three different sensor configurations (Fig. 4.2) for each material combination. To capture the variability between successive experiments, we repeated each experiment 15 times before modifying the sensor configurations. Additionally, each material configuration was unpacked, reassembled, and retested three times for sensor configuration 1 (see Fig. 4.2), totaling 45 experiments (for each sphere-cylinder material combination) for sensor configuration 1. This unpacking and reassembling allowed us to also capture the variability caused by differences in the initial contact lattices of the granular crystals.

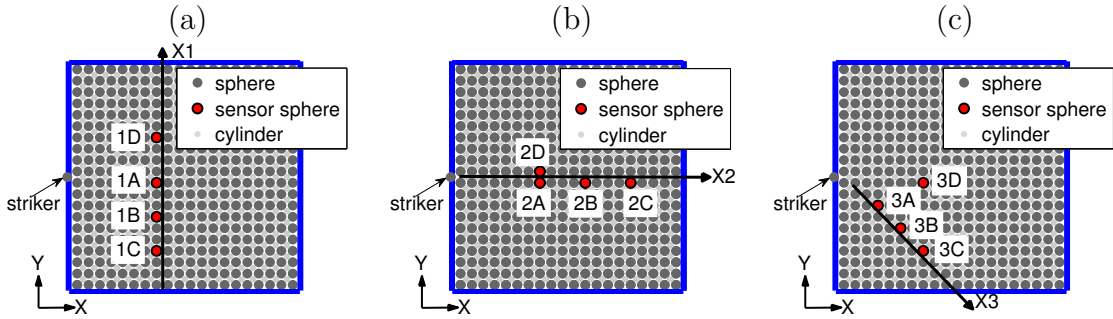


Figure 4.2: Schematic diagrams showing the sensor locations in experiments. (a) Sensor configuration 1 had sensors 1A, 1B, 1C, and 1D located at X_8Y_{10} , X_8Y_7 , X_8Y_4 , and X_8Y_{14} of the 20 by 20 sphere array for all material combinations. (b) Sensor configuration 2 had sensors 2A, 2B, 2C, and 2D located at X_8Y_{10} , $X_{12}Y_{10}$, $X_{16}Y_{10}$, and X_8Y_{11} of the 20 by 20 sphere array for the steel^s-ptfe^c, delrin^s-ptfe^c, and steel^s-steel^c crystals. Sensors 2A, 2B, 2C, and 2D were moved to locations X_4Y_{10} , X_8Y_{10} , $X_{12}Y_{10}$, and X_4Y_{11} of the 20 by 20 sphere array (4 spheres closer to the impact), due to small signal amplitudes for the delrin^s-steel^c crystals at locations far from the striker impact. (c) Sensor configuration 3 had sensors 3A, 3B, 3C, and 3D located at X_4Y_8 , X_6Y_6 , X_8Y_4 , and X_8Y_{10} of the 20 by 20 sphere array for all material combinations. For all experiments, the striker sphere impacted the system between the 10th and 11th edge spheres with initial velocity V_x .

In numerical simulations, the effects of disorder were investigated in two ways: the first one consisted of preparing multiple random realizations of the granular crystal and impacting each individual realization once (MR-SI, multiple realizations with single impacts). The second approach involved impacting a single realization multiple times (SR-MI, single realization with multiple impacts). For each study of MR, 15

realizations were prepared. Additionally, for several SR (chosen from the 15 MR) the initial configuration was impacted 15 times, allowing the system to come to rest between impacts. The acceleration time response of individual particles was monitored and compared with experimental results.

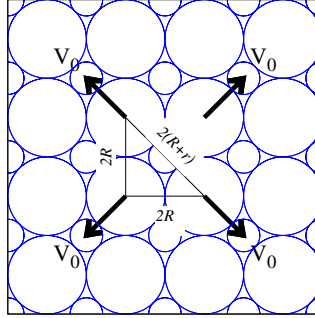


Figure 4.3: Schematic of extended granular crystal analyzed in the present study. Larger sized granules represent spheres (radius, R) while smaller ones are cylinders (radius, r). Wave propagation studies are performed on an extended set of this packing by giving a symmetric disturbance, setting initial velocities on four spherical granules as shown.

Additionally, numerical simulations were also performed (by collaborators using LAMMPS) on an extended pack of the centered square lattice which incorporates approximately 10,000 of both spherical particles and interstitial cylindrical intruders. For this extended system, we examined a wide space of cylinder-sphere mass and stiffness ratios in order to observe the different regimes of wave propagation. The extended system is perturbed symmetrically by giving equal initial velocities to four spheres (Fig. 4.3), and the different regimes of wave propagation are analyzed by monitoring the total compressive force (Equation 2.5).

4.2 Wave Propagation Path

In the absence of cylindrical intruders, Chapter 3 showed that the square array supported the formation and propagation of solitary waves along only initially excited chains. The addition of cylindrical intruders in the simple square packing transforms the system's response from quasi-one-dimensional to a truly two-dimensional

response. The introduction of additional contact points between the particles enables lateral energy redistribution. The lateral stress propagation properties depend on the mass and elastic properties of the intruder particles, as compared to the spherical particles. Variations of the particles' properties lead to variations in the stress propagation front within the system. For selected configurations, the wave front shape was highly directional, or triangular, in which most of the energy was directed centrally, in line with the impact direction (similar to the case without intruders). For other material configurations, the wave front shape was significantly spread along oblique directions, redirecting the impact energy towards the system's edges (see Figures 4.4 and 4.5).

4.2.1 Extended System Response

The present sphere-cylinder granular system supports a variety of propagating wave fronts which are tunable through the choice of mass and elastic moduli (stiffness) ratios as shown in Fig. 4.4. There are two clearly distinguished wave front regimes: (1) lattice-directed or directional propagation and (2) dispersed or 2D propagation. Within the dispersed propagation category, we further distinguish two types of transient wave propagation: (2a) pulsed and (2b) transitional. The directional wave propagation is characterized by pulses traveling along the lattice directions (Fig. 4.4i), similar to the case of a square array of spheres without interstitial cylinders. This directional behavior is characteristic of systems having a low stiffness ratio and high mass ratio. The 2D pulsed regime is characterized by a convex wave front, with either a square or circular propagating wave front shape (Fig. 4.4iv). This propagation regime occurs for mass ratios less than 0.1 and stiffness ratios greater than 0.5. Systems with wave fronts in the 2D transitional regime propagate without the presence of a distinct leading pulse and were observed to support a wide range of wave front shapes (Fig. 4.4 ii and iii).

The present results are consistent with the findings of previous reports on spherical-spherical systems [120]. The particle configurations tested experimentally are high-

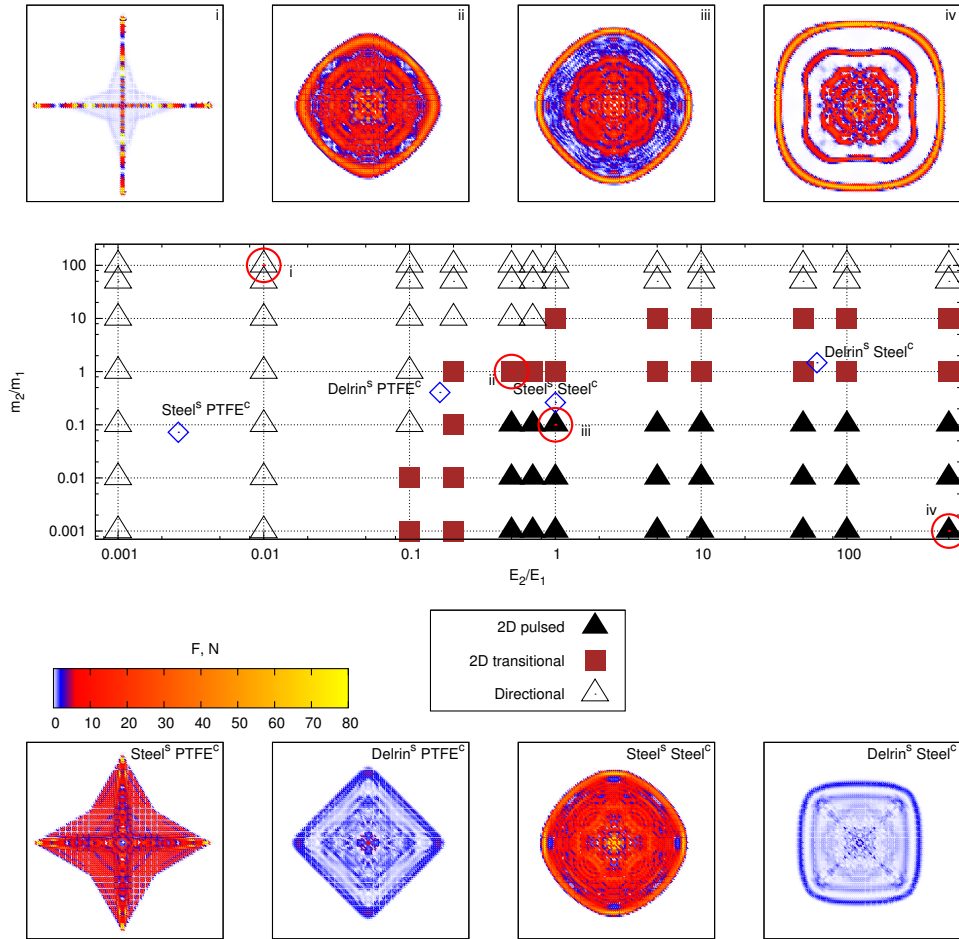


Figure 4.4: (Color online) (Center) Different wave propagation regimes mapped on mass (m_2/m_1) and stiffness (E_2/E_1) ratio space for the cylinder-sphere (2-1) system. (Top) Diagrams depicting examples of different wave fronts achievable in the systems at selected mass and stiffness ratios, indicated with circles in the central figure. (Bottom) Four insets depicting the propagating wave front shapes for the four material systems tested in experiments, indicated with diamond-shaped symbols in the central figure.

lighted by diamond-shaped symbols in Fig. 4.4, and their wave front shapes in the extended system are shown in the bottom panels of Fig. 4.4. The very low stiffness ratio inherent in the steel^s-ptfe^c system causes the wave propagation to be mostly directional. While the other experimental systems (delrin^s-ptfe^c, steel^s-steel^c, and delrin^s-steel^c) all lie in the transition regime, the shape of the propagating front is significantly different for each material combination. As will be discussed in 4.2.2, the trends observed in experiments were found to be in good agreement with numerical simulations on non-random granular crystals.

4.2.2 Experimental Results

Experiments and corresponding numerical simulations were performed: (a) steel^s-ptfe^c (b) delrin^s-ptfe^c, (c) steel^s-steel^c, and (d) delrin^s-steel^c in order to capture a wide range of propagating wave front shapes. The numerical simulations compared with experiments in this section always assumed a perfect contact lattice. The numerical results showed significant differences in the wave front shape, in terms of particle velocity magnitude, between each of the tested material configurations (Figure 4.5). When the tested system consisted of stiff, heavy spheres and light, softer intruders, we observed highly directional wave propagation (Figure 4.5a). When the tested system consisted of slightly stiffer spheres than cylinders with similar masses, we again observed a wave front in which most of the energy was directed centrally in line with the impact, but with a more uniform triangular shape (Figure 4.5b). The configuration of spheres and cylindrical intruders of identical materials resulted in a relatively uniform, circular wave front propagating through the granular system (Figure 4.5c). Lastly, when we tested the system composed of light, soft spheres with heavier, stiff intruders we were able to divert a significant portion of the impact energy towards the system's edges, away from the central particles (Figure 4.5d).

We can describe the differences in the propagating wave front in terms of relative arrival times and relative stress wave amplitudes within the granular systems. The relative arrival times of the wave front at locations parallel to the y-axis (or X1 axis in

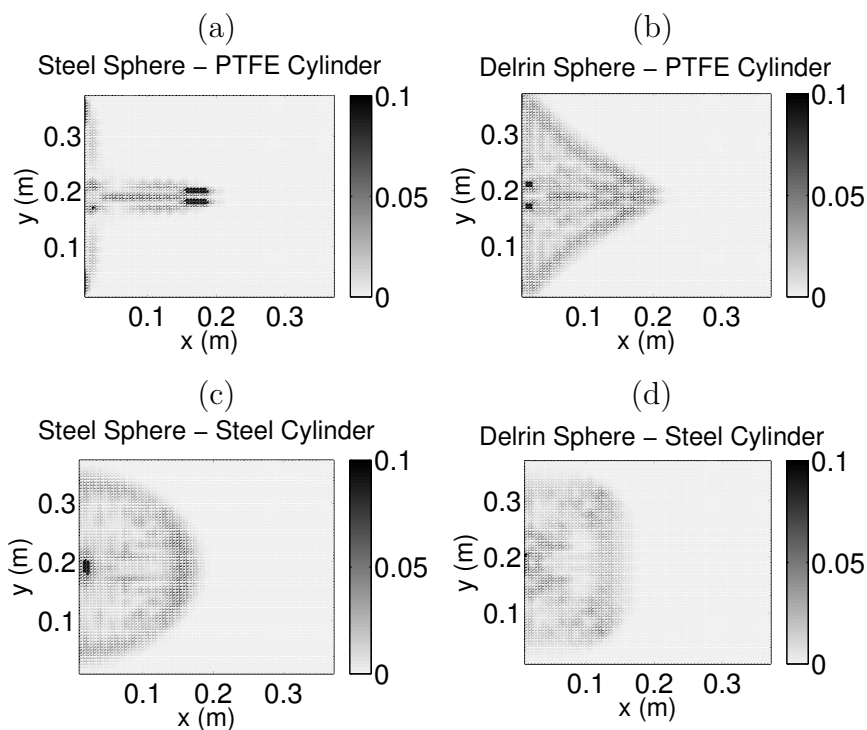


Figure 4.5: Numerical simulation results showing the wave front shape in terms of particle velocity magnitude for each of the experimentally tested material configurations. X- and y-axes represent the particle position. For the steel sphere configurations, Figures (a) and (c) show particle velocities 0.35 ms after the steel striker sphere impact ($V_x = 0.73$ m/s). For the delrin sphere configurations, Figures (b) and (d) show particle velocities at 1.0 ms after the delrin striker sphere impact ($V_x = 0.92$ m/s). Grey scales indicate particle velocity in m/s.

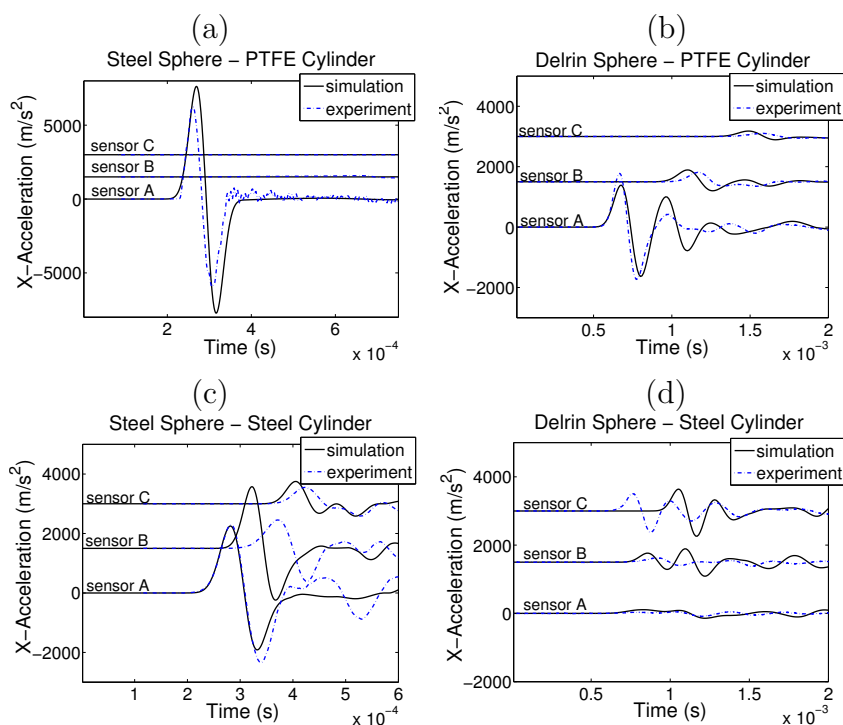


Figure 4.6: Comparison of individual particle acceleration as a function of time between experiments and simulations for each of the sphere-cylinder material combinations tested: (a) steel-ptfe, (b) delrin-ptfe, (c) steel-steel, and (d) delrin-steel. Acceleration data at sensor locations B and C were shifted up 1500 and 3000 m/s^2 , respectively, for visual clarity. Zero time in simulations was defined as the moment of striker impact. To compare experimental and simulation data, experimental data for each test configuration was shifted so the signal arrival time of sensor A in simulations and experiments coincided.

Figure 4.2a) can be used to describe the wave front shape. Additionally, the relative amplitudes along the same line can be used to describe the distribution of energy in the wave front. However, a unique property of nonlinear granular systems is that these two quantities are not independent. For more complex two-dimensional systems, the exact analytical relation between wave speed and amplitude is not known, however, recent numerical observed a similar power-law scaling as with 1D chains [120]. In our experiments and numerical simulations we also observe that directions of higher wave amplitude correspond to directions of faster wave propagation.

The characteristics describing the different wave shapes observed in numerical simulations are in good agreement with the experimental data (Figure 4.6). The experimental data in Figure 4.6 represents the typical response of each system (i.e., is representative of the mean values plotted in Figure 4.7 (Top) for a single packing). We present here only the x-acceleration, however, we observed that the comparison between experiments and numerical simulations of both x- and y-acceleration displayed consistent trends. For the system composed of steel spheres and ptfе intruders, we observed most of the impact energy being centrally directed, in line with the impact, and we detected negligible signals away from the central particles, in excellent agreement with numerical simulations (Figure 4.6a). In the system consisting of delrin spheres and ptfе intruders (Figure 4.6b), we observed a considerably higher amplitude signal arriving first at the central sensor, as opposed to the signal detected towards the system's edges. These differences in amplitude and arrival times measured between sensors qualitatively agree with the numerical results showing the formation of a triangular wave front shape. For the case of identical sphere and intruder particle materials (Figure 4.6c), we observed comparable amplitudes at central sensors, A and B (see Figure 4.1), with slightly lower amplitude at the sensor closer to the system's edge. We also observed relative signal arrival times consistent with the numerically observed more uniform, rounded wave front. Finally, by using delrin spheres and steel intruders, we observed the largest amplitude signal furthest from the central particles (Figure 4.6d) indicating substantial impact energy redirection, consistent with the numerical simulations.

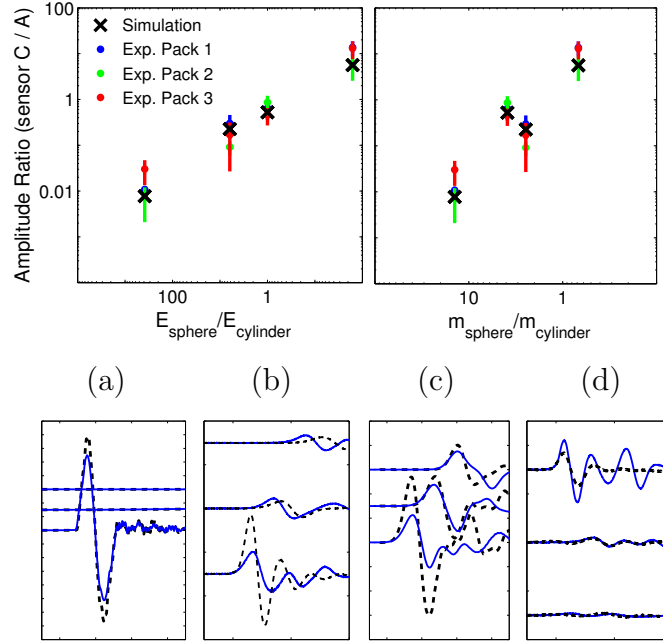


Figure 4.7: (Top) Ratio of the maximum acceleration amplitude at sensor locations C and A plotted against the ratio of the sphere-cylinder (Left) stiffness and (Right) masses. For experimental data, the mean and standard deviation, std, (error bars) are plotted for each of the three initial packings assembled for each material configuration. (Bottom) The x-accelerations at sensor locations A, B, and C (positioned as in Figure 4.6) most closely representing +1 std (solid blue) and -1 std (dashed black) for Pack 1 are plotted for each sphere-cylinder material configuration: (a) steel-ptfe, (b) delrin-ptfe, (c) steel-steel, and (d) delrin-steel. Y-ticks indicate 1000 m/s^2 . X-ticks indicate 0.1 ms for (a) and (c) and 1.5 ms for (b) and (d).

In the lattices that incorporate stiffer intruders, deviations were apparent between the experimental and numerically calculated signal amplitudes and arrival times (Figure 4.6c,d). The presence of dissipation, evident in the experimental results, may account for the noticeable time delays observed between the pulses recorded experimentally and the ones obtained from numerical simulations. A notable discrepancy between experiments and numerical simulations exist in the relative signal arrival times in the case of delrin spheres and steel cylinders (Figure 4.6d); the experiments seem to suggest an exaggerated impact energy redirection.

Figure 4.7 compares the response from experiments and numerical simulations for the four tested material combinations. We calculated the ratio of the maximum

amplitude at sensor location C with respect to location A (Figure 4.1), capturing the main features of the wave fronts. An amplitude ratio greater than one, as observed with the delrin spheres and steel intruders, indicates a wave front consistent with the impact energy being diverted away from the central line of impact. A ratio near one, as observed for the steel spheres and steel intruders, indicates a uniform, circular wave front. Similarly, as the ratio decreases below one we observed more amplitude being centrally directed within the system. While there is notable variation between experiments, the agreement between the mean response in experiments and numerical simulations is quite good. To visualize the variation in wave front shapes between successive experiments, the experiments most closely representing the standard deviations are also plotted for a packing of each test configuration (Figure 4.7 Bottom). We plotted the wave front amplitude ratio against both the sphere-cylinder material stiffness ratio and mass ratio (Figure 4.7 Top). A decreasing trend was observed for both stiffness and mass ratios as the wavefront began to follow a more pointed triangular form. However, only the stiffness ratio had a monotonically decreasing relationship with the shape of the particle velocity wave front. This suggests that the material stiffness had a more significant effect on the wave front shape than the mass ratios for the material combinations tested.

4.2.3 Effects of Weak Disorder

We now study how the presence of disorder in experiments and numerical simulations affects the response of the system, and compare the response with that of ideal granular crystals. Here, we use the term ideal granular crystals to refer to assemblies with identical particles placed along even grid spacings. In this study, weakly disordered crystals were modeled by incorporating small random deviations in the particle diameters, resulting in initial contact lattice imperfections (refer to Section 2.3.1.2). For numerical simulations, the effects of disorder were investigated in two ways: the first one consisted of preparing multiple random realizations of the granular crystal and impacting each individual realization once (MR-SI, multiple realizations

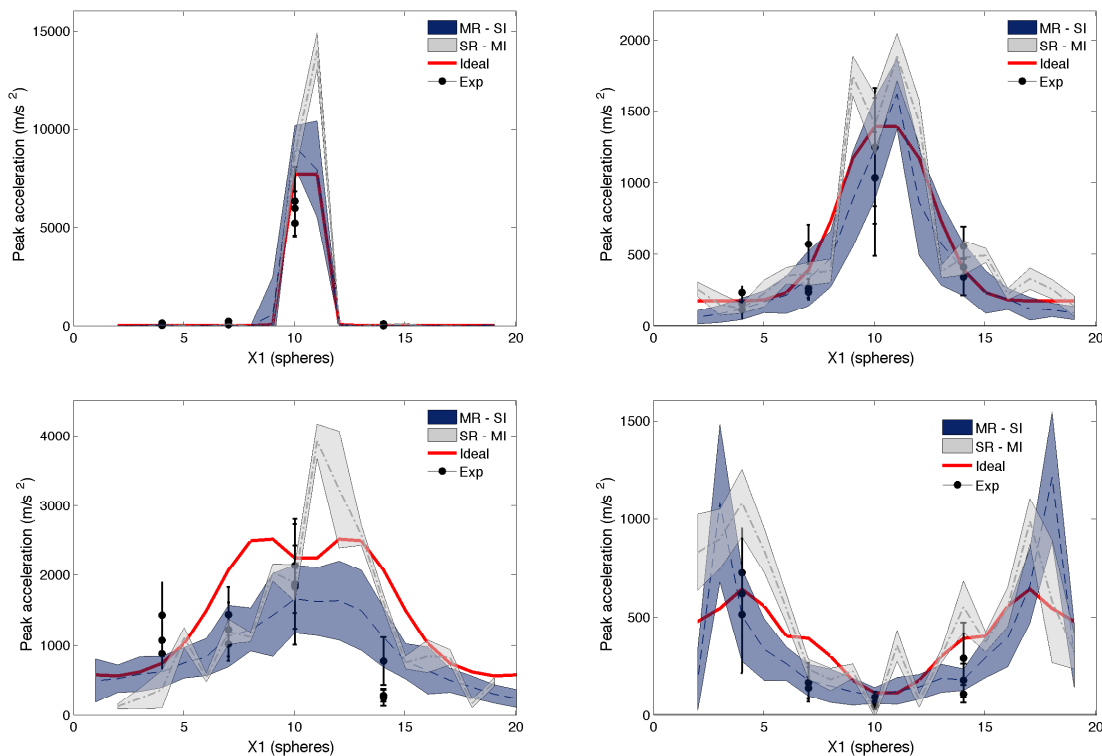


Figure 4.8: (Color online) Peak acceleration (m/s^2) in the wave front as a function of X1 (in units of spheres) for each sphere - cylinder material combination: (a) steel^s-ptfe^c, (b) delrin^s-ptfe^c (c) steel^s-steel^c, and (d) delrin^s-steel^c. The results from numerical simulations for the ideal granular crystal are shown by the solid (red) lines. The mean and standard deviation are represented by a dashed lines and dark (blue) shaded regions for the MR-SI (15 realizations each with a single impact) and by dot-dashed lines and light (grey) shaded for the SR-MI (a single realization with 15 impacts). The experimental data is represented by black dots with error bars for the 3 realizations tested with 15 impacts each.

with single impacts). The second approach involved impacting a single realization multiple times (SR-MI, single realization with multiple impacts). For each study of MR, 15 realizations were prepared. Additionally, for several SR (chosen from the 15 MR) the initial configuration was impacted 15 times, allowing the system to come to rest between impacts. The acceleration time response of individual particles was monitored and compared with experimental results.

For the chosen sensor configurations, the shape of each wave front can best be captured by looking at the relative amplitudes and arrival times of the signals along

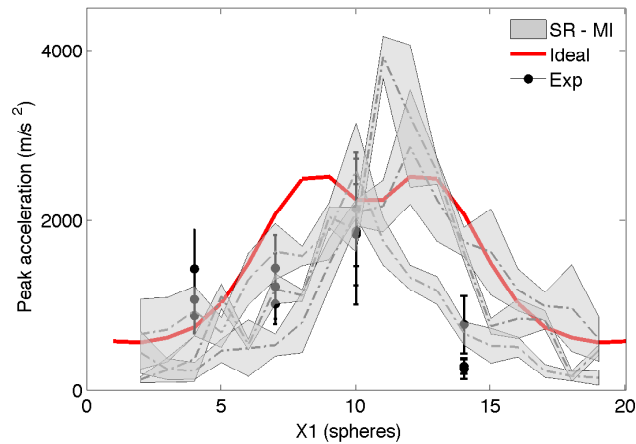


Figure 4.9: (Color online) Peak acceleration (m/s^2) in the wave front as a function of X1 (in units of spheres) for the steel^s-steel^c crystal. The results from numerical simulations for the ideal granular crystal are shown by the solid (red) lines. The mean and standard deviation for 3 single realizations with 15 multiple impacts (SR-MI) are represented by dot-dashed lines and shaded light grey regions. The experimental data is represented by black dots with error bars for the 3 realizations tested with 15 impacts each.

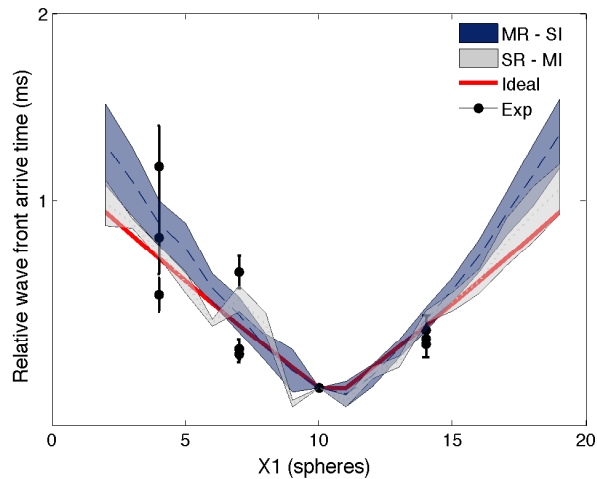


Figure 4.10: (Color online) Relative wave front arrival times along X1 (spheres) with respect to sensor location 1A, for the delrin^s-ptfe^c crystal. The results from numerical simulations for the ideal granular crystal are shown by the solid (red) lines. The mean and standard deviation are represented by a dashed line and dark (blue) shaded region for the MR-SI and by a dot-dashed line and light (grey) shaded region for the SR-MI. For each sensor location along X1, 3 sets of black dots and error bars represent the mean and standard deviation for the 3 single experimental realizations with multiple impacts.

an axis perpendicular to the impact, e.g., the X1 direction (see Fig. 4.2). The peak accelerations in the wave front along the X1 direction are shown in Fig. 4.8 for the four material systems under consideration. In the case of the steel^s-ptfe^c crystal (Fig. 4.8a), the two central rows of spherical particles have a significantly higher amplitude than the remaining particles extending to the crystals edge, clearly signifying the highly directional shape observed in the ideal system (Fig. 4.4). For the delrin^s-ptfe^c crystal (Fig. 4.8b), we see a similar trend, with significantly larger amplitude at the central particles, but with a more gradual decrease in amplitude as the sphere locations approach the edges, corresponding to a triangular wave front shape. The peak acceleration distribution for the steel^s-steel^c crystal (Fig. 4.8c) is smoother, with comparable amplitudes along X1, corresponding to the circular wave front predicted for the ideal system. Finally, for the delrin^s-steel^c crystal (Fig. 4.8d), the largest amplitudes are now located close to the crystal edges and the smallest amplitudes at the center of the domain, indicating the squared, re-directive wave front shape observed in the ideal crystal numerical simulations (Fig. 4.4).

The effects of the weak disorder on the wave front shapes of the four tested material systems are also illustrated in Fig. 4.8. The wave shapes depicted by average values of peak acceleration along X1 obtained from MR-SI (multiple realizations with single impacts) on each system are consistent with those predicted for the respective ideal crystals. Additionally, the average peak acceleration at sensor locations in the 3 experimental realizations of each system generally lie within the distributions predicted through MR-SI. Previous 1D studies have shown that the presence of weak disorder results in attenuation of the leading pulse [130, 131]. We observe a similar trend in the numerical simulations, in which the average wave front amplitude predicted through MR of weakly disordered systems is slightly lower than that of the ideal, non-random, system.

While the overall trends for individual particle responses from MR closely resembles the ideal system, any single realization (SR) may produce larger deviations from the ideal system response. This is illustrated in Fig. 4.8, in which a randomly selected SR (one of the MR) is shown in for each sphere-cylinder system. The distribution of

wave front amplitude for an SR depends on the underlying initial contact lattice and does not vary significantly over multiple impacts (MI), which may cause slight particle rearrangements. The wave front amplitude distributions along X1 for 3 SR-MI of the steel^s-steel^c system are shown in Fig. 4.9. The variability in wave front amplitude distribution between SR is evident and arises from slight particle misalignments which are unique to the individual contact lattice of an SR.

Another way to characterize the effects of disorder on the wave front shapes is to consider the relative arrival times between sphere locations along X1 (Fig. 4.10). Here, we present only the arrival times for the delrin^s-ptfe^c crystal, since the results show similar information as the peak acceleration plots (Fig. 4.8). As the spheres are located further from the central particles, the arrival times increase linearly with distance from the impact location, consistent with a triangular wave front. Similar to the distribution of wave amplitudes, we note that the variability, or standard deviation in arrival times, associated with MR is greater than that emerging from MI. Additionally, for both SR and MR, the scatter observed in the results is more pronounced near the sides of the primary wavefront. This is expected since the waves must travel through more particle contacts, and hence encounter more interfaces than the middle portion. We find good agreement between the numerical results and the signal variability measured experimentally.

Next, we present in Fig. 4.11 the acceleration-time curves measured by our sensors at each particle location. These local measurements allow for a more direct comparison of the signal variability due to the presence of disorder in the system. We compare the numerical results obtained for a lattice with no disorder (Fig. 4.11a), with experimental results (Fig. 4.11b), and results obtained numerically for the MR-SI (Fig. 4.11c) and SR - MI (Fig. 4.11d) cases. Similar to the experimental data, the numerical results show slight deviations from the ideal response for each realization. The individual particle responses corresponding to any one impact in experiments and numerical simulations are quantitatively different, but qualitatively similar. The variation in wave front amplitude, initial pulse shape, and signal arrival times in numerical results are similar to those obtained experimentally for the delrin^s-ptfe^c

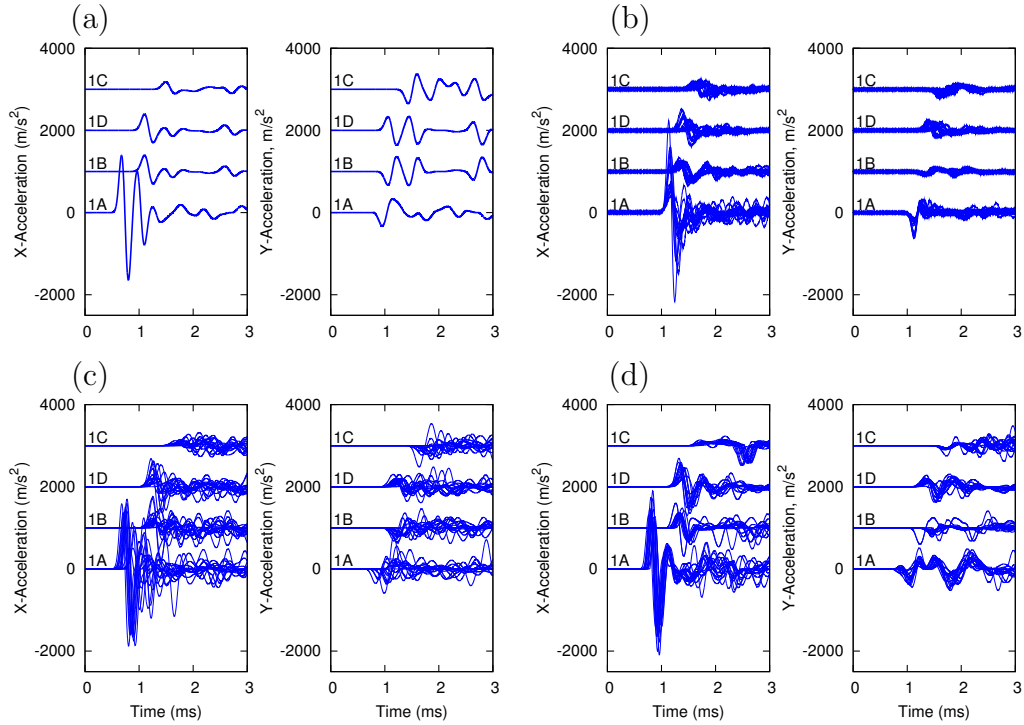


Figure 4.11: Experimental and numerical simulation results for the x- and y-acceleration profiles for sensor configuration 1 (see Fig. 4.2) of the delrin^s-ptfe^c granular crystal. (a) Simulation results for the ideal granular crystal. (b) Experimental results for a single packing (SR) impacted 15 times. (c) Numerical simulation results for 15 different realizations (MR), each impacted once. (d) Numerical simulation results for a single realization (SR), impacted 15 times. For visual clarity, the acceleration data at sensor locations 1B, 1D, and 1C are shifted by 1000, 2000, and 3000 m/s^2 , respectively, from sensor location 1A. The zero time in the simulations denotes the moment of impact, while the zero time in experiments is arbitrary since the recorded data is based off the signal arrival time of sensor 1A.

crystal (Fig. 4.11), as well as for the other three sphere-cylinder systems (not shown).

The individual acceleration profiles also show that variability in the tails of the signals is more pronounced than that in the initially arriving pulse. This effect is linked to the combination of small compressive forces and gaps present in the system as a result of disorder. The larger amplitude oscillations in the tails of the signals are also responsible for the more pronounced amplitude decay of the leading pulse, evident in the disordered systems.

In order to study the effects of disorder on the wave front propagation along different radial directions within the crystal, we measure the wave front peak acceleration distributions along the X2 (in line with the impact) and X3 (along a 45 degree angle to the impact) directions (refer to Fig. 4.2). We observe more variability between the amplitudes along X1 compared to those along X2 and X3. Sensors A, B, and C along X2 and X3 measure the peak acceleration along a line of particle contacts originating at the excitation, while sensors A, B, and C along X1 capture the relationship between the peak acceleration distributions along several radial directions from the impact.

In all cases, we observe good agreement between experiments and numerical results obtained including initial contact lattice disorder due to the particle tolerances. In experiments, additional sources of disorder could arise from imperfect orientations and surface textures of the confining walls. Also, minor variability in striker speed and impact locations can be present in the experiments. Variable striker speeds are expected to equally affect the measurements at all sensor locations, while off-center striker impacts are expected to result in asymmetries in the system response. We performed additional numerical simulations incorporating a uniform random distribution of particle diameters. A uniform probability distribution leads to more frequent and larger gaps in the initial contact lattice, i.e., increased disorder. In numerical simulations, we observed significantly larger wave amplitude variability, corresponding to less distinguishable wave front shapes between material combinations, for a uniform random distribution compared to the normal distribution of particle diameters. The level of disorder present in experiments was effectively captured by the numerical

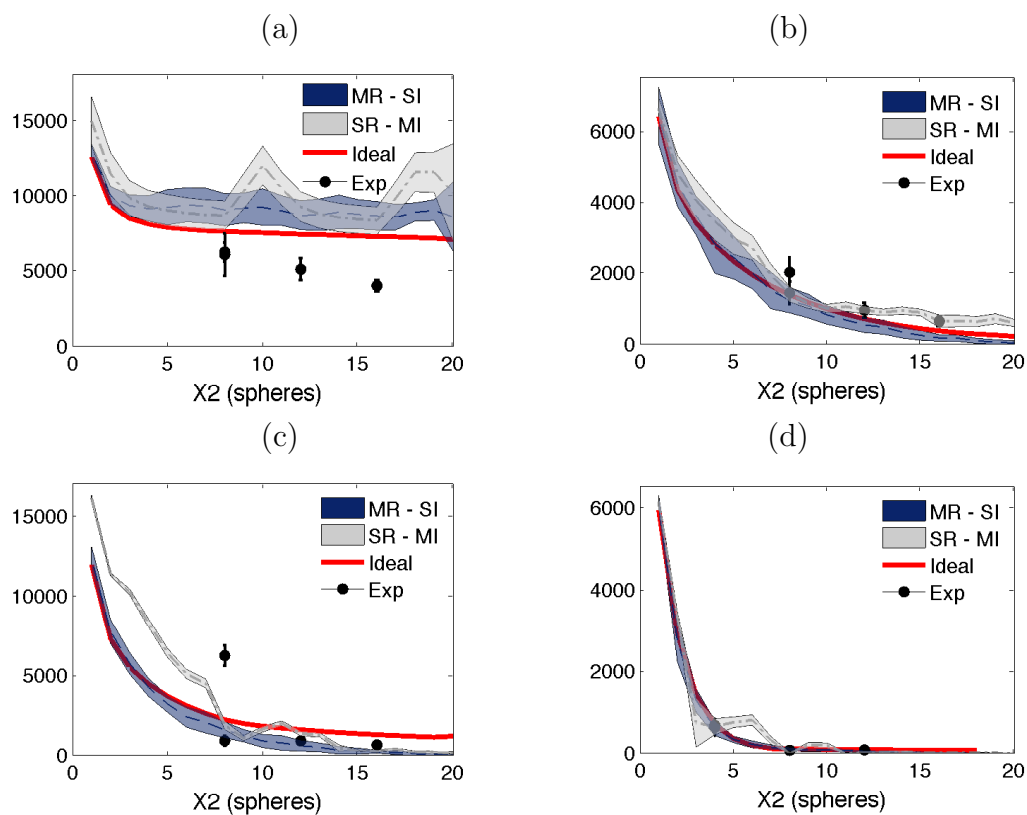


Figure 4.12: (Color online) Peak acceleration (m/s^2) in the wave front versus X_2 (in units of spheres) for each sphere - cylinder material combination: (a) steel^s-ptfe^c, (b) delrin^s-ptfe^c (c) steel^s-steel^c, and (d) delrin^s-steel^c. The results from numerical simulations for the ideal granular crystal are shown by the solid (red) lines. The mean and standard deviation are represented by dashed lines and dark (blue) shaded regions for the MR-SI and by dot-dashed lines and light (grey) shaded regions for the SR-MI. For each sensor location along X_2 , a set of black dots and error bars represent the mean and standard deviation for the single experimental realization with multiple impacts.

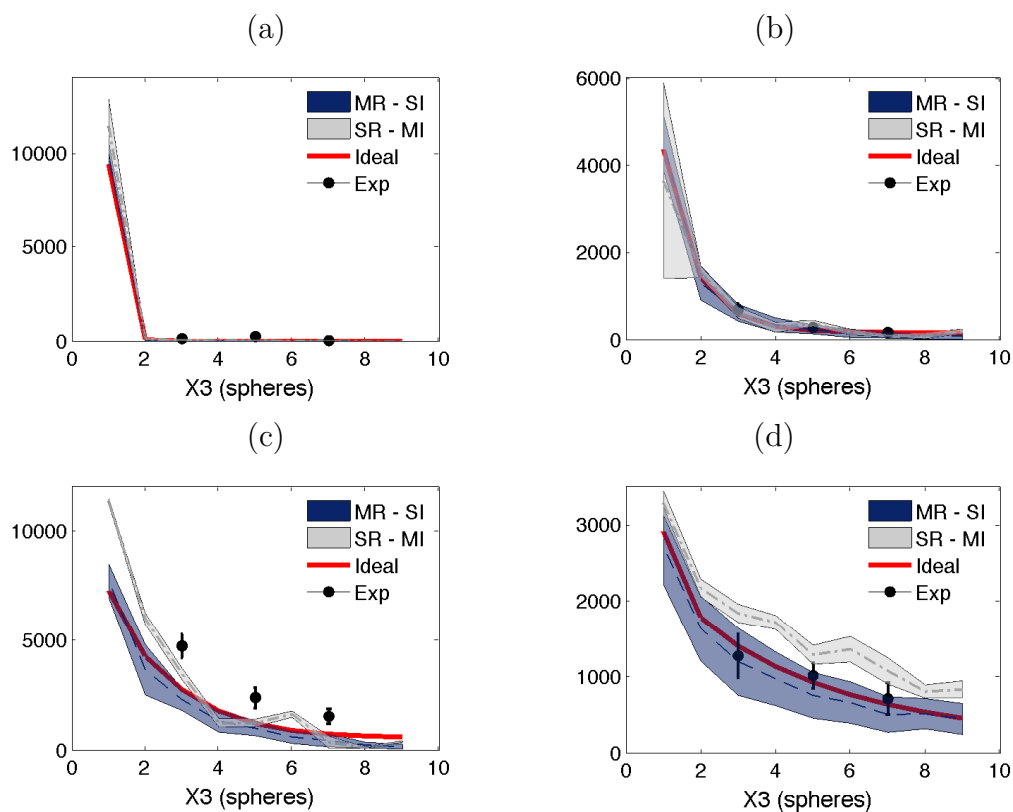


Figure 4.13: (Color online) Peak acceleration (m/s^2) in the wave front as a function of $X3$ (in units of spheres) for each sphere - cylinder material combination: (a) steel^s-ptfe^c, (b) delrin^s-ptfe^c (c) steel^s-steel^c, and (d) delrin^s-steel^c. The results from numerical simulations for the ideal granular crystal are shown by the solid (red) lines. The mean and standard deviation are represented by dashed lines and dark (blue) shaded regions for the MR-SI and by dot-dashed lines and light (grey) shaded regions for the SR-MI. For each sensor location along $X3$, a set of black dots and error bars represent the mean and standard deviation for the single experimental realization with multiple impacts.

simulations incorporating the normal distribution of particle diameters based on the specified precision ball bearing tolerances. Additionally, some discrepancies between trends observed in experiments and numerical simulations can be attributed to dissipation which are not accounted for in our numerical simulations. The presence of dissipation in experiments results in signal attenuation and time delays (Figs. 4.8, 4.10, 4.12 and 4.13).

The average particle responses from MR (both experimental and numerical) are consistent with the wave front shapes predicted by numerical simulations of ideal granular crystals. For the steel^s-ptfe^c and delrin^s-ptfe^c granular crystals, the average particle responses from MR are in good agreement with the directional and triangular wave front shapes, respectively, (Figs. 4.8a and 4.8b). Similarly, for the steel^s-steel^c and delrin^s-steel^c systems, the average particle responses from MR are comparable with those predicted by the ideal system. However, the average response of the steel^s-steel^c weakly disordered systems produces a slightly more uniform distribution of peak acceleration in the wave front compared to the ideal system response (Fig. 4.8c). Additionally, in both numerical simulations and experiments, the weakly disordered delrin^s-steel^c system results in the diverted impact energy, or squared wave front shape to be more pronounced compared to that of the ideal crystal (Fig. 4.8d).

4.2.4 Additional Numerical Study: Effects of Pre-Compression

We performed additional numerical simulations with higher and lower impact velocities and observed that the wave front shape in the highly nonlinear regime is independent of excitation amplitude (within the elastic limit). However, the properties of the traveling waves depend on the relative amplitude of the excitation (F_{impact}) to the initial displacement, or pre-compression.

For the four material combinations tested in experiments, we performed additional numerical simulations on the presented granular systems with after incorporating pre-compression. In these numerical simulations, the initial configuration of the compressed system was attained by adjusting the location of the confining walls (and

settling subsequent random particle motion similar to 2.3.1.2). The prescribed wall locations, resulted in a static force $F_{static} \approx 50 \text{ N}$. The resting compressed particle arrangement were then impacted with the same striker sphere. The striker sphere impact velocity was varied in order to probe the system response in a variety of regimes: linear ($F_{impact}/F_{static} \ll 1$), weakly nonlinear ($F_{impact}/F_{static} \approx 1$), and highly nonlinear ($F_{impact}/F_{static} \gg 1$). The results of these numerical simulations are shown in Figure 4.14. We found that in all cases, the general wave front shape is consistent with those described by the uncompressed, or highly nonlinear regime. However, as the system response moves towards the linear regime (i.e., as $V_{striker}$ was decreased, leading to $F_{impact}/F_{static} \ll 1$), the effects of dispersion become prominent. In the weakly nonlinear and linear regime, more of the energy is observed to be distributed into the trailing waves as opposed to more energy being carried in the wave front in the highly nonlinear regime studied.

4.3 Summary of Results

We demonstrated the ability to systematically alter the shape of the stress wave front traveling through a two-dimensional granular system subject to impulse loading. By varying the mass and stiffness ratios of the particles in the array, we showed extensive variation in the wave front shape resulting in substantial impact energy redirection. Experimental results confirmed the variation in wave shape observed in numerical simulations in terms of the wave front amplitude distribution.

Additional numerical simulations on weakly disordered systems incorporated particle diameter tolerances. We independently assessed the variability arising from differences in initial contact lattices and from particle rearrangements between successive impacts by performing tests for multiple realizations with single impacts (MR-SI) and single realizations with multiple impacts (SR-MI). The agreements between the acceleration profiles in experiments and numerical simulations suggest that the main source of variability present in real systems derives from particle size imperfections which create a weakly disordered initial contact lattice. In both experiments and numerical

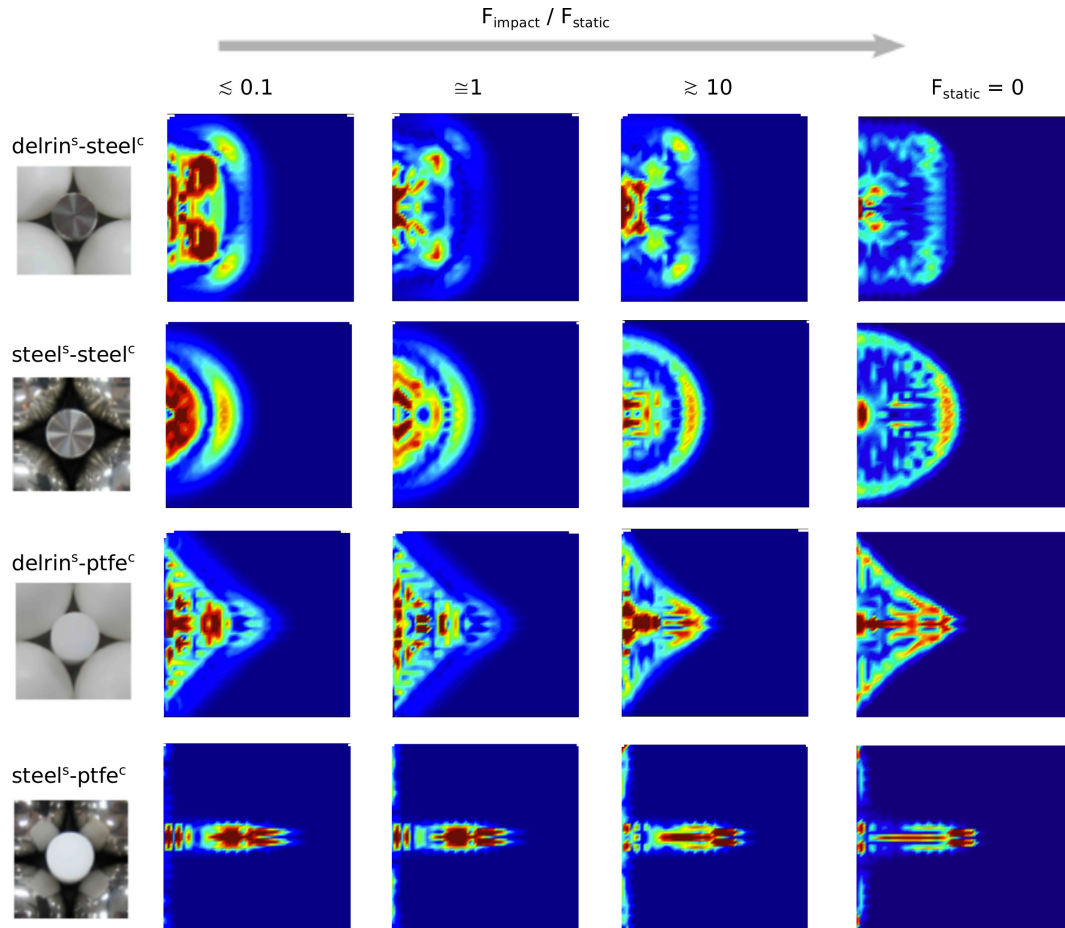


Figure 4.14: Numerical simulation results qualitatively showing the dependence of the wave front shape on the ratio of the impact force F_{impact} to the static compression F_{static} . Each row represents a single sphere^s – cylinder^c material combinations, for which a unit cell is also picture on the left.

simulations, larger discrepancies existed between the average response of SR-MI and those of the ideal granular crystal, compared to the average response of the MR-SI. However, while discrepancies exist between individual tests, the average properties of the wave fronts for each of the four material configurations tested were consistent with those predicted by numerical simulations on ideal granular crystals, confirming the ability to systematically alter the properties in real 2D arrays. This work is a first step in designing granular crystals with predetermined wave propagation paths.

Chapter 5

2D Granular Crystals: Hexagonal

We describe the dynamic response of a two-dimensional hexagonal packing of uncompressed spheres excited by localized impulsive loadings. After the initial impact strikes the system, a characteristic wave structure emerges and decays as it propagates through the lattice. We study how energy is spread throughout a hexagonally packed granular crystal lattice upon being struck at different “strike angles” and being observed at different “observation angles”. In a simple special case, we are also able to compare our experiments and numerical simulations with theoretical predictions based on a ternary collision approximation. Additionally, we discuss the effects of weak disorder on the directional amplitude decay rates.

5.1 Problem Description and Approach

We performed experiments on a 2D hexagonal array of particles consisting of 11 spheres along each edge of the lattice (see Fig 5.1). The spheres were stainless steel (type 316), with diameter $d = 19.05 \text{ mm}$ [1]. The hexagonal particle lattice was confined, but not compressed, by the setup described in Section 2.2.1, with a hole at the impact location along one edge. To aid in the lattice particle alignment, a slight tilt ($< 5^\circ$) was imposed in the x-direction of the experimental setup. To excite the system, a striker sphere, identical to the spheres composing the 2D hexagonal granular crystal, impacted the central particle along one edge. The striker sphere rolled through a channel down the inclined experimental setup and its initial velocity was

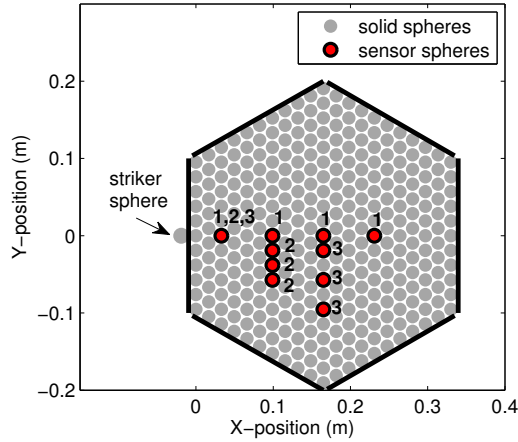


Figure 5.1: Schematic diagram of the experimental setup. The solid stainless steel sphere locations are represented with grey circles. The confining walls are represented by solid black lines. The striker sphere impacts the system as shown, with an initial velocity $V_{striker}$ in the x -direction. The locations of sensor particles are marked with a red circle and outlined in black. The number next to each sensor location indicates the different sensor configurations: 1, 2, and 3 (with 4 sensors present for any given experiment).

calculated from the drop height. To capture the system response, 3 different sensor configurations were used: (1) along the 0° observation direction, (2) perpendicular and near to the impact, and (3) perpendicular to and further from the impact (see Fig 5.1). The sensor in the lattice location closest to the impact was present in all three sensor configurations.

In order to capture the variability caused by differences in initial contact lattices, 20 different particle packings were assembled and experimentally tested (for each sensor configuration, 1-3) with an initial striker velocity of $V_{striker} = 0.40 \text{ m/s}$. Each of the 20 initial assemblies was impacted repeatedly to calculate average wave front amplitude and arrival time values, which could differ due to slight variations in impact conditions, such as exact alignment and speed of the striker particle, and minor particle rearrangements. Additionally, experiments for 20 different initial particle packings with sensor configuration 1 were performed for striker velocities, $V_{striker} = 0.25 \text{ m/s}$ and $V_{striker} = 0.70 \text{ m/s}$.

The impact conditions of the experimental assembly were chosen for experimental

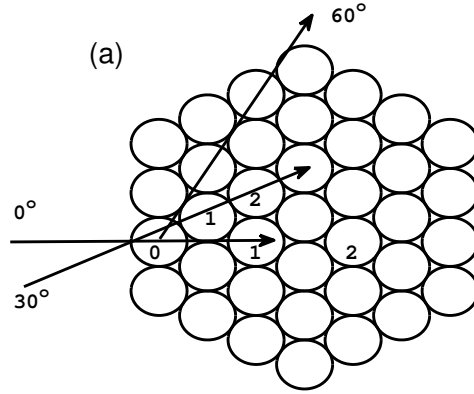


Figure 5.2: (a) Orientation of the hexagonal lattice and possible striking and observation angles. The numeric labels correspond to the counting conventions used along the respective observation angles.

ease and consistency. For the theoretical considerations described below, the initial velocity V_0 was assigned to the $n = 0$ bead, that is, the bead impacted by the striker sphere in experiments (see also Fig 5.2). However, numerical simulations, comparing the system response for an array with $V_{striker} = V_0$ and $V_{n=0} = V_0$, showed that the difference was negligible for the studied system.

5.2 Wave Propagation Path

In 2D configurations, one can study traveling structures by observing a row of beads along different radial directions from the impact bead. Figure 5.2 defines the angles of observation for the hexagonal crystal investigated in this chapter. Recall for a square packing, that quasi-one-dimensional traveling solitary waves emerge upon striking the lattice, and are essentially described by the one-dimensional theory (CH 3). However, even in a simple 2D homogeneous packing, such as the hexagonal crystal, this quasi-one-dimensional motion is not possible, since each adjacent row and column will be affected upon being struck, regardless of the striking angle. After initially impacting a single bead, the energy will gradually be spread over progressively more and more lattice sites. Since the energy continues to spread to an increasing number of beads, the (energy and) velocity profile will gradually decrease, and thus a perfect traveling

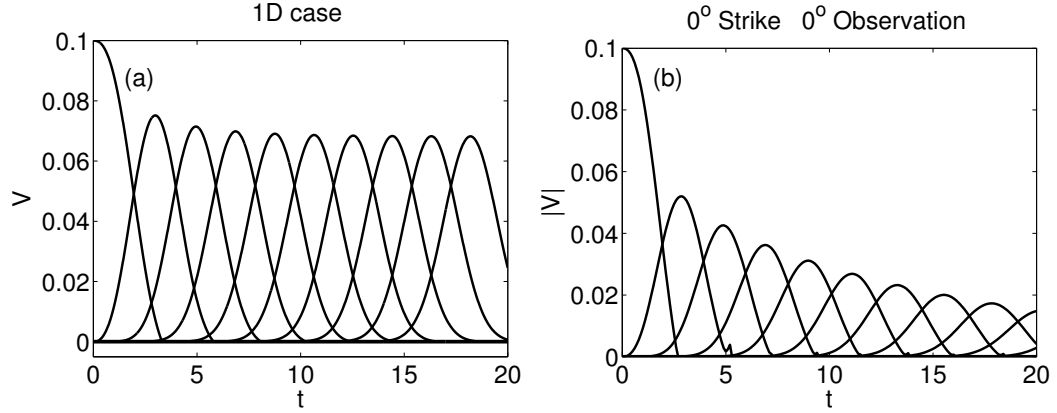


Figure 5.3: (a) Velocity profile for the first ten beads in an initially at rest 1D granular crystal after impact on the left boundary with $A = d = M = 1$. Notice that the maximum velocity attained by each bead is approximately constant after impact (denoting the rapid settling of the chain into a traveling solitary wave). (b) Velocity profile for the first ten beads along the zero degree line (refer to Figure 5.2) of an initially at rest 2D hexagonal granular crystal with $A = d = M = 1$. Notice that the maximum velocity attained by each bead decays (denoting the spreading of the energy to an increasing number of beads). Refer to Appendix A or Equation 5.1 for rescaling relations.

solitary wave will be impossible to support. Figure 5.3 compares the solitary wave motion in a 1D chain with the pulse velocity profile along the 0° observation direction of the hexagonal crystal.

The numerical simulation results for the configuration corresponding to the experimental setup are shown in Figure 5.4. Additionally, numerical simulations were performed for a larger array consisting of 45-spheres along the bounding hexagonal edge, compared to the 11-sphere per edge system tested in experiments. Figure 5.5 shows the evolution of the wavefront shape over the larger 2D hexagonal system.

5.2.1 Ternary Collision Approximation and Numerical Study

As part of this project, collaborators extended the binary collision approximation (BCA) developed for 1D chains [42–46], into a ternary collision approximation (TCA), to analytically predict the wave propagation within the hexagonal crystal. Additionally, since the TCA ignores the (weak) dependence of the decay rate on impact

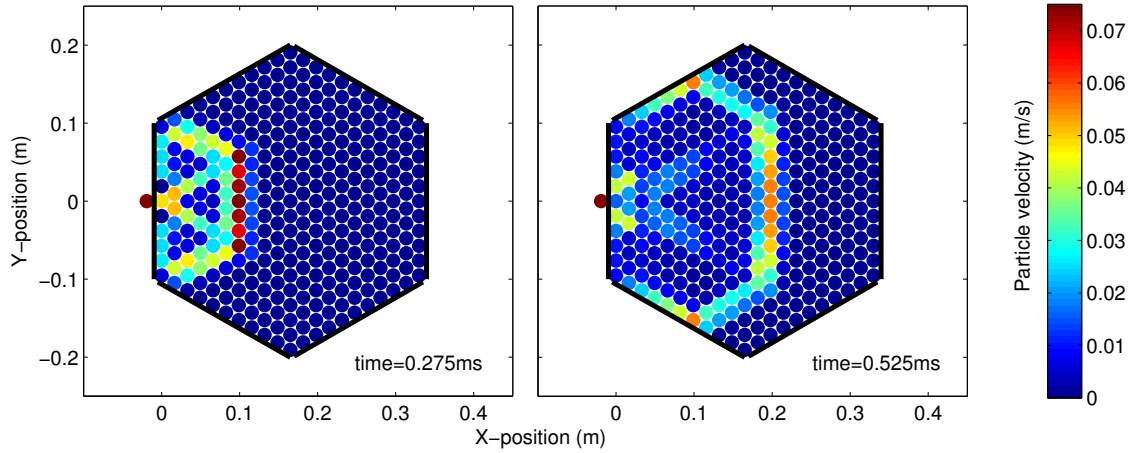


Figure 5.4: Numerical simulation results showing the wave front shape evolution for the 11-sphere edge system tested in experiments. The array was centrally impacted along the edge by a striker sphere with initial velocity $V_{striker} = 0.40 \text{ m/s}$. The colorbar indicates particle velocity magnitude in m/s .

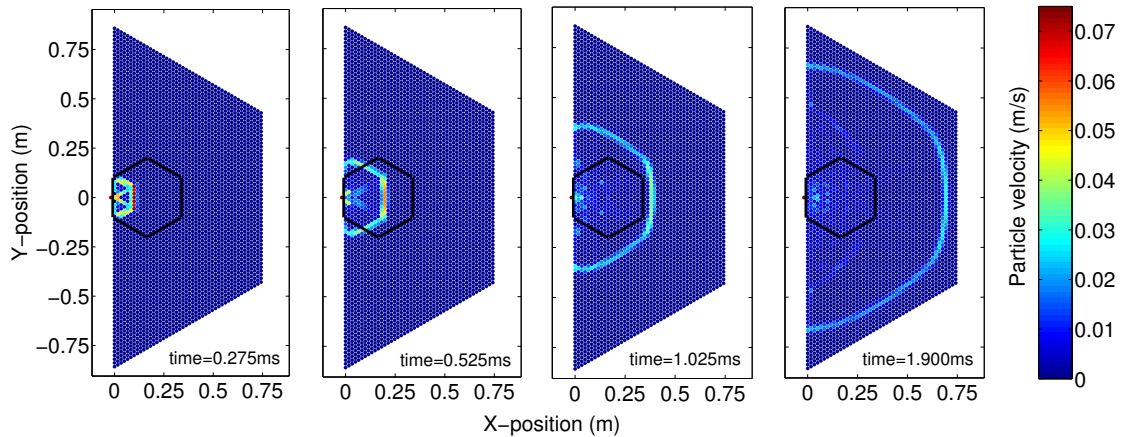


Figure 5.5: Numerical simulation results showing the wave front shape evolution for a larger hexagonal packing (91 particles along the left, long edge, and 45 particles along the shorter edges). The array was centrally impacted along the edge by a striker sphere with initial velocity $V_{striker} = 0.40 \text{ m/s}$. The black hexagon indicates the wall locations for the size of the experimental setup. The colorbar indicates particle velocity magnitude in m/s .

velocity, and is restricted to an observation angle of 30° , they also performed a numerical study, in which relations for the leading pulse decay are described for 0° and 30° impact and observation angles. In this chapter, we present only the results of these studies and compare them with our experiments (and numerical simulations). Note, in the results presented below, in order to obtain the scaling law for arbitrary parameter values:

$$\begin{aligned} &\text{replace each occurrence of } V \text{ with } V \frac{\sqrt{M/A}}{d^{5/4}}, \\ &\text{where } A = \frac{4E\sqrt{R}}{3(1-\nu^2)}, \quad M = \frac{4}{3}\pi R^3 \rho, \quad \text{and } d = 2R. \end{aligned} \tag{5.1}$$

Please refer for Appendix A for a detailed description of the TCA model and the corresponding numerical study.

5.2.1.1 30° Angle of Observation

It is more straightforward to develop the theory for a striking and observation angle of 30° since the pattern does not alternate along this line of observation, in contrast to what is the case for a 0° striking and observation, see Fig. 5.2. The TCA approximation (see Appendix A) predicts the velocity of the n^{th} bead along the 30° observation to be

$$V_n = V_0 c^n, \tag{5.2}$$

where V_0 is the (30° strike) impact velocity. In the rescaled system we found $c \approx 0.8452$. To amend the TCA to a 0° strike (but still observing along the 30° line) we need to understand how the energy is transferred among the first two beads that are in contact with the impact bead (see Fig. 5.2). Due to symmetry considerations, it is reasonable to conjecture that the velocity contribution along the 30° (resp. -30°) will be half of the impact velocity. This would be the case if kinetic energy and momentum were conserved.

From the numerical study on the rescaled system, the particle velocity along the

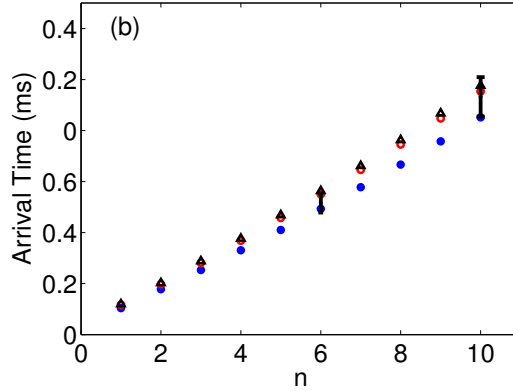


Figure 5.6: (b) The arrival time of the pulse for the experimental parameter values at a 0° strike and 30° observation angle with $V_0 = 0.4$ m/s. The blue dots represent numerical simulations, the red circles are the TCA (EQ 5.2), the black triangles denote the exact analytical solution to the TCA (see Appendix A), and the points with error bars at $n = 6$ and $n = 10$ are the experimental values.

30° angle of observation subject to a 30° strike angle is expected to follow:

$$V_n = V_0 (\alpha V_0 + \beta)(mV_0 + b)^{n-1}, \quad n > 0, \quad (5.3)$$

with $m \approx 0.257$ and $b \approx 0.832$. Similarly, for a 0° strike angle, the particle velocity along the 30° angle of observation will follow:

$$V_n = V_0 (\alpha V_0^2 + \beta V_0 + \gamma)(mV_0 + b)^{n-1}, \quad n > 0 \quad (5.4)$$

with $m \approx 0.1484$, $b \approx 0.8393$ and $\alpha \approx -0.1182$, $\beta \approx 0.0203$, $\gamma \approx 0.5192$.

At the 0° strike and 30° observation angle we have experimental data available for comparison, see the right panel of Fig. 5.6. Due to the limited number of sensors available, a more direct comparison between the TCA and experiments is achieved for arrival time data (which is the sum of the relevant residence times, App A). We should also note that the experiments use the arrival time at the first sensor position in Fig. 5.1 to define $t = 0$. Thus, in order to compare the experimental values to the TCA and numerical simulations we estimate the arrival time at the first sensor using the numerical simulation.

5.2.1.2 0° Angle of Observation

Due to the alternating bead pattern along the 0° angle of observation, the TCA model was not carried out in this direction. Instead we present only the results from the numerical simulations.

When observing along the zero degree line it turns out that fitting is more accurate when starting at bead 2. After a 30° strike, we have then that

$$V_n = V_0 (\alpha V_0^2 + \beta V_0 + \gamma)(mV_0 + b)^{n-2}, \quad n > 1 \quad (5.5)$$

with $m \approx .3039$, $b \approx .8756$ and $\alpha \approx -0.4788$, $\beta \approx -0.0256$, $\gamma \approx 0.1936$. Similarly, following a 0° strike, the equation takes the same form as EQ 5.5, but now with $m \approx 0.1766$, $b \approx 0.8878$ and $\alpha \approx -0.2643$, $\beta \approx -.0969$, $\gamma \approx .2152$.

5.2.2 Experimental Results and Effects of Weak Disorder

Based on the numerical simulations of the ideal hexagonal lattice (Figs 5.4 and 5.5), the wavefront shape can be initially described by a hexagonal pattern which transitions into a more circular shape. Figure 5.7 compares the initial wavefront shape observed in the ideal numerical simulations with those observed in the experiments and numerical simulations incorporating weak disorder. The average wave front arrival times from both experiments and numerical simulations incorporating weak disorder clearly show the initial hexagonal wave front propagating through the structure. The average arrival times in experiments are slightly later than those predicted from the ideal numerical simulations. Physically, this can be understood since the dissipation present in experiments results in a decreased wave amplitude, consequently slowing the wave front speed. Additionally, imperfections in the experimental contact lattices also result in redirection of wave amplitude and delays in the signal arrival time. As Figure 5.7 indicates, the relative arrival times in the weakly disorder simulations are notably later than both the predicted values from the ideal simulations as well as the experiments. This is a bit surprising considering that the simulations do not incor-

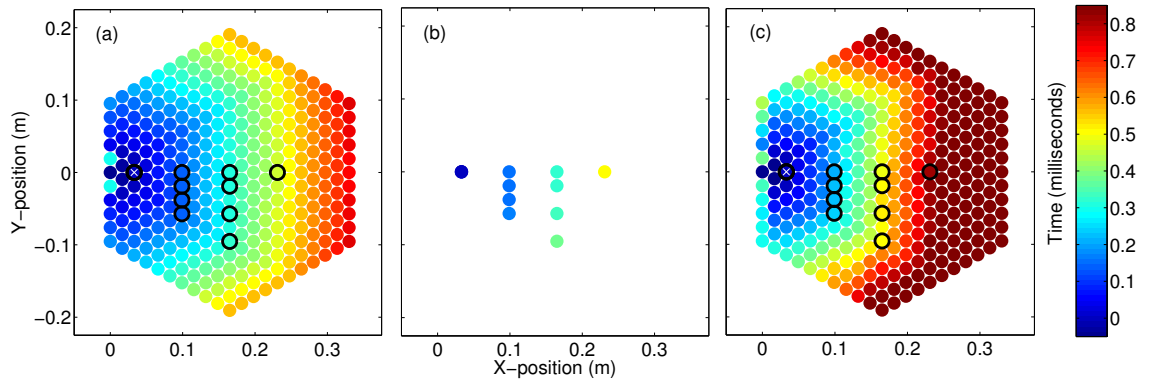


Figure 5.7: Wave front shape based on the relative wave front arrival time with respect to the particle marked with a white x. (a) Numerical simulation of ideal system. (b) Average wave front arrival time calculated from experiments. (c) Average wave front arrival time calculated from simulations with weak disorder. Black circles in the left and right panels indicate experimental sensor locations. The colorbar indicates the relative wave front arrival time in milliseconds.

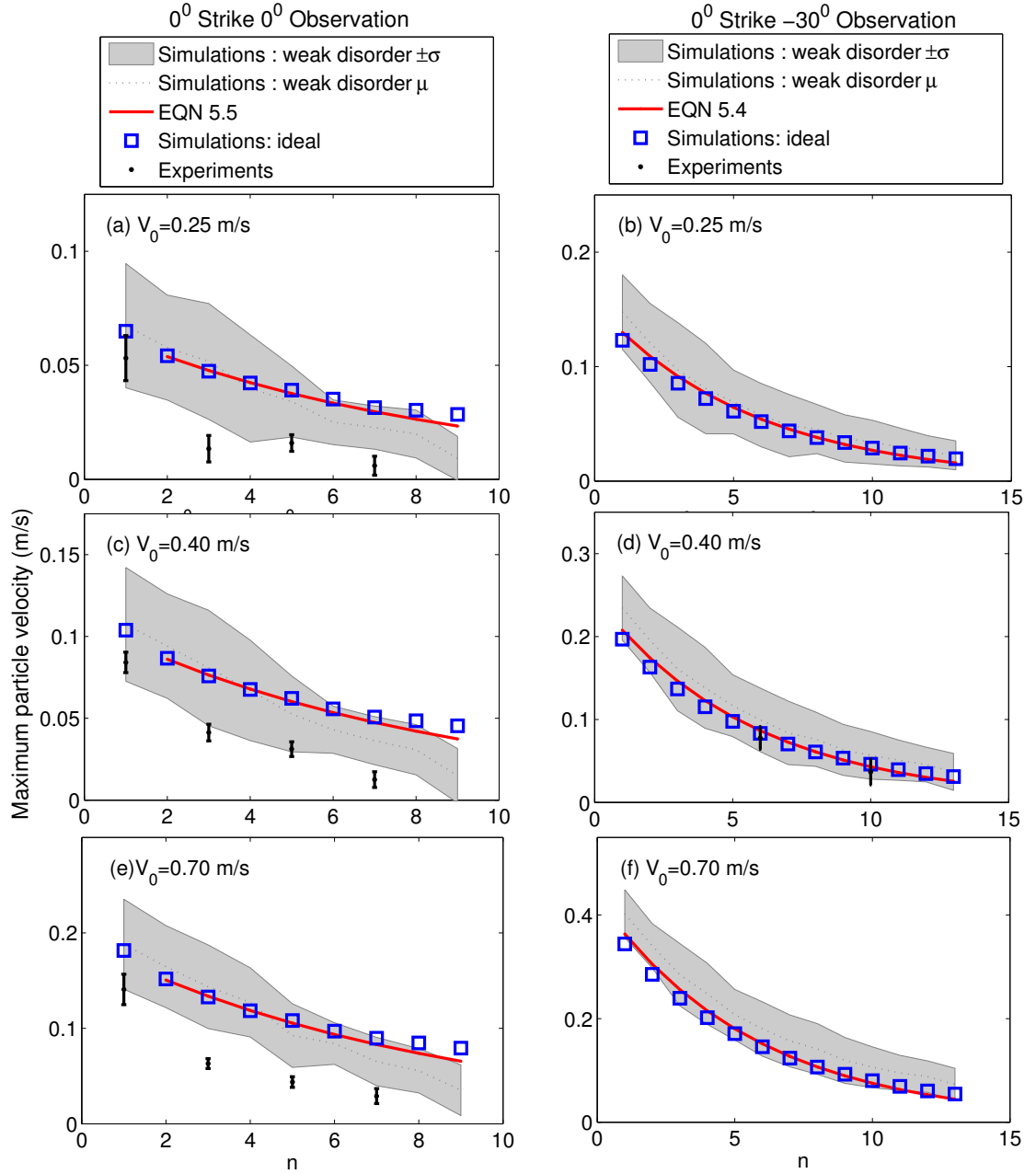


Figure 5.8: Maximum particle velocity with respect to sphere position, n . (a), (c), (e): 0° Strike and 0° Observation. (b), (d), (f): 0° Strike and -30° Observation. Initial velocity: (a), (b) $V_0 = 0.25$ m/s; (c), (d) $V_0 = 0.40$ m/s; and (e), (f) $V_0 = 0.70$ m/s. Shaded grey regions indicate ± 1 standard deviation, σ , and dotted grey lines indicate the average value, μ , from the 20 simulations incorporating weak disorder. The solid red lines represent Equations (5.5) and (5.4). The black dots and error bars represent the mean and standard deviation from experiments ($V_0 = 0.25, 0.40$, and 0.70 m/s for 0° Strike 0° Observation and $V_0 = 0.40$ m/s for 0° Strike 30° Observation).

porate dissipation, thus the time delay is due entirely to the effects of the particle misalignments. The discrepancy between the arrival times in experiments and weakly disordered numerical simulations suggests that the tolerance values used to simulate imperfections in the contact lattice are fairly conservative.

Figure 5.8 compares the wave front amplitude decay along the 0° and -30° observation directions after a 0° strike angle for experiments, ideal numerical simulations, weakly disordered numerical simulations, and the corresponding Eqns (5.5) and (5.4). Overall the trends observed for all approaches are in good agreement. The presence of weak disorder in the numerical simulations results in decreased amplitude transmission along the 0° observation direction and increased amplitude transmission along the -30° observation direction, compared to the ideal simulations. This altered distribution of wave front amplitude can be seen in Fig 5.8, where the mean amplitude from simulations incorporating weak disorder falls above the ideal simulation values along the $\pm 30^\circ$ observation direction and below the ideal simulation values along the 0° observation direction. The 30° observation direction represents a line of spheres directly in contact, while the wave front must travel through a zig-zag of particle contacts along the 0° direction. Therefore, the number of contacts, or possible amplitude scattering points, is greater along the 0° observation direction, which could help physically explain this amplitude redistribution phenomenon. Although the presence of dissipation in experiments results in lower average amplitudes compared to the weakly disordered numerical simulations, which neglect dissipation, we also observe this trend in average experimental amplitude values (Fig. 5.8 and $V_0 = 0.40 \text{ m/s}$).

5.3 Additional Numerical Study: Dimer

In addition to the homogeneous 2D hexagonal array, we also investigate the response of a dimer hexagonal packing. The choice of dimer lattice geometry was based on previously studied of highly nonlinear wave propagation in 1D dimer chains. In 1D, these dimer systems have been shown support solitary waves with the same amplitude-wave speed scaling relation as homogeneous chains, but with a oscillating wavelength

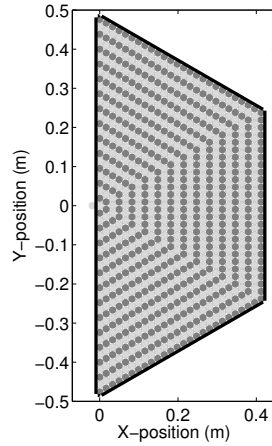


Figure 5.9: Schematic diagram of a 2D dimer hexagonal array. The dark and light grey particles indicate the two different materials composing the dimer array.

that depends on the mass ratio of the dimer pair [52, 53]. In analogous 2D hexagonal geometry is attained by alternating material properties in the radial direction from the excitation (see Figure 5.9). Here we provide only qualitative comparisons between the 1D dimer and 2D hexagonal dimer system. Detailed studies of this dimer systems are left for future work.

The propagating wave structure in a 2D hexagonal dimer system composed of alternating stainless steel (type 316) and aluminum spheres resulting from a localized impact is shown in Figure 5.10. From the numerical simulations, we observe several similarities between this system and the 1D dimer chains, in comparison to their respective homogeneous lattices. A localized wave front is observed similar to the homogenous system, but with an increased effective wavelength and an alternating pulse amplitude. Figure 5.11 shows the leading pulse amplitude decay in both the 0° and 30° observation directions. Along the 30° direction of observation, i.e., the direction of a dimer sphere chain, the alternating leading pulse amplitude is observed. Additionally, Figure 5.12 shows the full width of the leading pulse at half the maximum value (FWHM) along the 30° observation, or dimer, direction. The FWHM values obtained from the force profiles of each n particle, were converted into length (particle diameters) using a locally calculated pulse velocity $\frac{2d}{time_{arrival_{n+1}} - time_{arrival_{n-1}}}$. Similar to [52, 53], we observed that the FWHM values alternate between the two sphere ma-

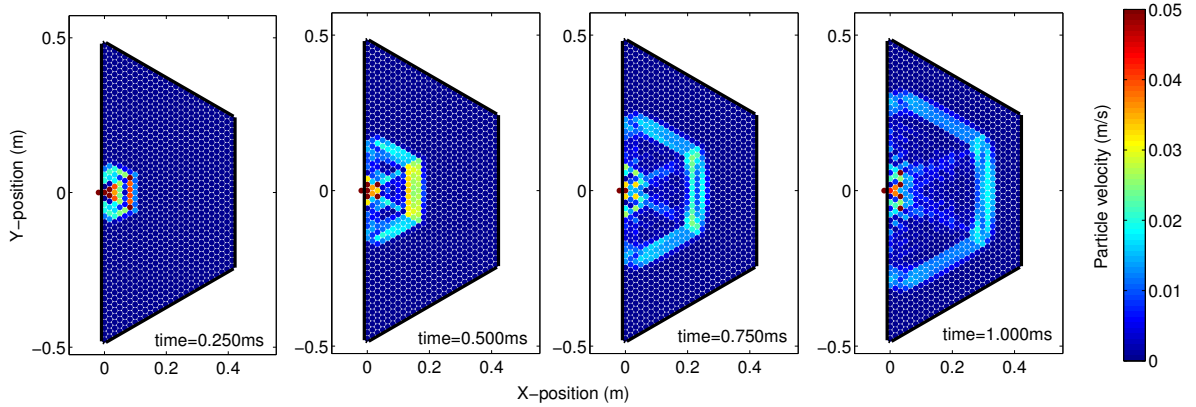


Figure 5.10: Numerical simulation results showing the wave front shape evolution for the dimer system with 26-spheres along the short edges. The sphere materials are aluminum and stainless steel, light and dark grey, respectively, in Fig 5.9. The array was centrally impacted along the edge by an aluminum striker sphere with initial velocity $V_{striker} = 0.50 \text{ m/s}$. The colorbar indicates particle velocity magnitude in m/s .

terials, with an effective dimer leading pulse width that is greater than the monomer one.

5.4 Summary of Results

We presented a systematic study of the dynamic response of a 2D hexagonal, highly nonlinear lattice excited by an impulse. In this 2D hexagonal setting, because of the ever-increasing number of neighbors over which the energy is distributed, no genuine traveling wave excitations, i.e., with constant velocity, have been found to persist. The propagating pulse energy has been found to decay as a power law, both in our numerical computations and in our experimental observations. Detailed expressions were provided to describe these power laws. In a special case (of 30° strike and 30° observation, according to our presented classification), a generalization of the binary collision approximation (dubbed the ternary collision approximation) was presented

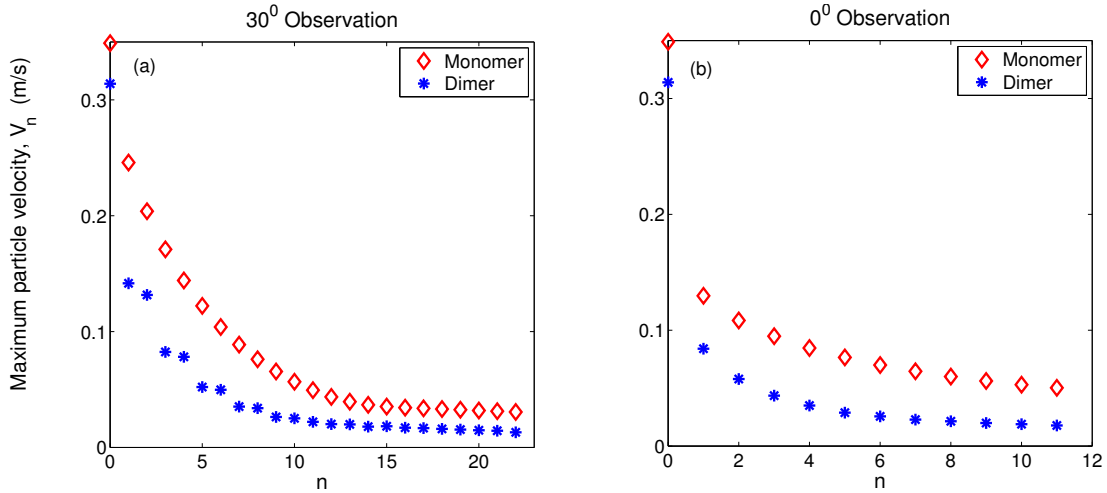


Figure 5.11: Numerical simulation results showing the wave front amplitude decay for a 0° aluminum striker with $V_{striker} = 0.5$ m/s observing at (a) 30° and (b) 0° . The x-axis bead numbering, n , follows the same scheme as described in Figure 5.2. The red diamonds indicate numerical simulations for a hexagonal monomer of aluminum spheres. The blue asterisks indicate numerical simulations for a dimer with steel and aluminum (same as Fig 5.10).

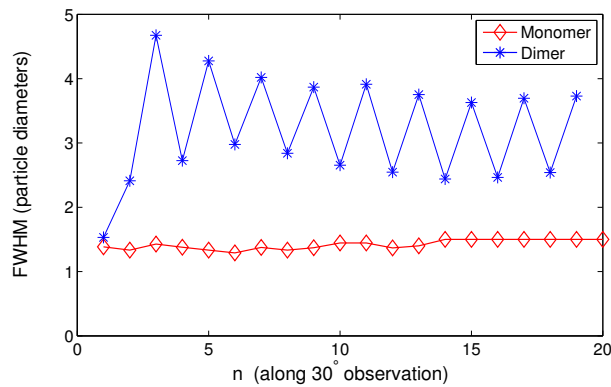


Figure 5.12: Numerical simulation results showing the full width at half max (FWHM) of the leading pulse along the 30° observation direction for the aluminum monomer (red diamonds) and aluminum-steel dimer (blue asterisks).

and utilized to give simple numerical and even approximate analytical expressions for the bead evolution. Lastly, the effects of weak disorder on the propagating wave structure were examined; the average spatial amplitude values from numerical simulations incorporating weak disorder were in good agreement with experimental values as well as the corresponding fitted equations derived from numerical simulations on the ideal hexagonal granular crystal. This agreement reveals that the level of disorder present in experiments does not cause significant deviation of the propagating wave structure from the predicted system response. Lastly, preliminary studies suggest comment on the similarities between the homogenous 1D chain and dimer chain, and the homogeneous and dimer 2D hexagonal array.

Chapter 6

Ordered Granular Network: 2D

We study the propagation of stress waves through ordered 2D networks of granular chains. The quasi-particle continuum theory employed captures the acoustic pulse splitting, bending, and recombination through the network and is used to derive its effective acoustic properties. The strong wave mitigation properties of the network predicted theoretically are confirmed through both numerical simulations and experimental tests. In particular, the leading pulse amplitude propagating through the system is shown to decay exponentially with the propagation distance and the spatial structure of the transmitted wave shows an exponential localization along the direction of the incident wave. The length scales that characterized these exponential decays are studied and determined as a function of the geometrical properties of the network. These results open avenues for the design of efficient impact mitigating structures and provide new insights into the mechanisms of wave propagation in granular matter.

6.1 Problem Description and Approach

The granular network tested in our experiments is comprised of an initial segment that divides into two symmetric branches. Each new branch is then split into two symmetric branches, that can merge with other branches of the network (see Fig. 6.1). This process is repeated N times, in order to produce a network of degree N that consists of $(N+1)$ exit chains where the transmitted wave can be measured. Contrary

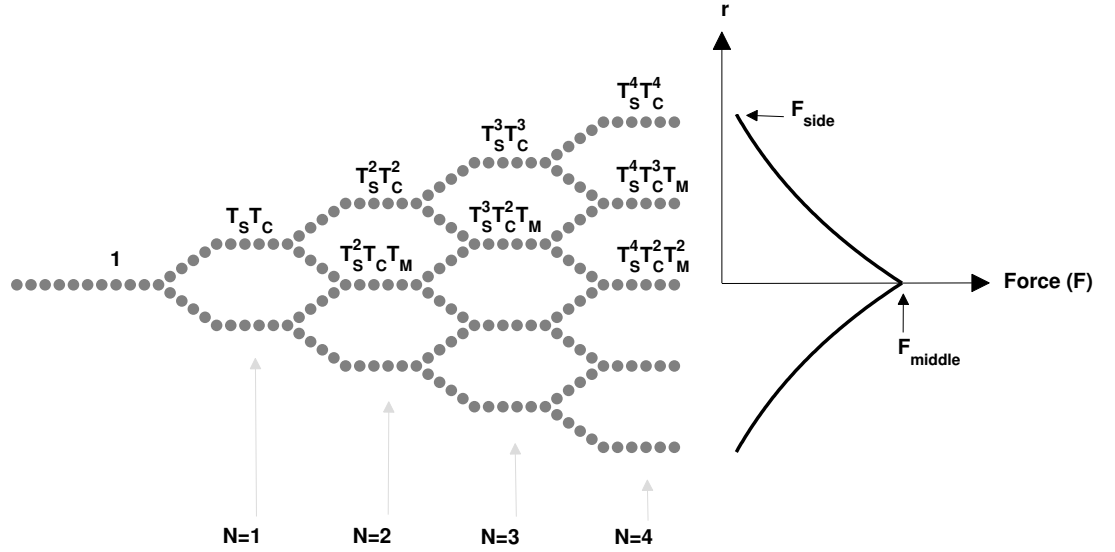


Figure 6.1: Schematic diagram of the granular network investigated in this study. (Left) The wave transmission coefficients at each of the straight segments is given as a function of elementary transmission coefficients, T_S , T_C and T_M , and corresponds to $N=1$ up to $N=4$ levels structures. (Right) The transmitted force F profile as a function of the normalized distance r from the middle of the network.

to “classical” disordered granular media, the deterministic arrangement of granular chains allows for a rigorous description of the wave propagation and scattering within the network from which the effective acoustic response will be predicted (see Section 6.2). The initial segment consists of 10 spheres to allow an incident solitary wave to develop. The branching angle was chosen to minimize losses of the incident wave due to wave reflection, so that wave splitting remains the main mitigation mechanism. As the branch angle α increases, the loss around the corners continues to increase until no force is transmitted for $\alpha = 90^\circ$ (see Section 6.2). However, a lower limit $\alpha = 30^\circ$ exists, at which point the spheres on either side of the branching junctions come into contact. To guarantee clearance between neighboring particles at branch junctions within the assembly, $\alpha = 35^\circ$ was chosen for all experimentally tested networks. In order to minimize dissipative losses along the length of the chains, each

branching segment consisted of 6 spheres, which is sufficient to support the solitary wave length of approximately 5 particle diameters [5]. The tested granular networks consist of spheres (precision ball bearings from [1]) assembled in the supporting channel structures. The spheres are stainless steel (type 440C) with diameter, $d = 9.5$ mm. The supporting channel structures are fabricated using VeroClear material with the Connex 500 3D printing system.

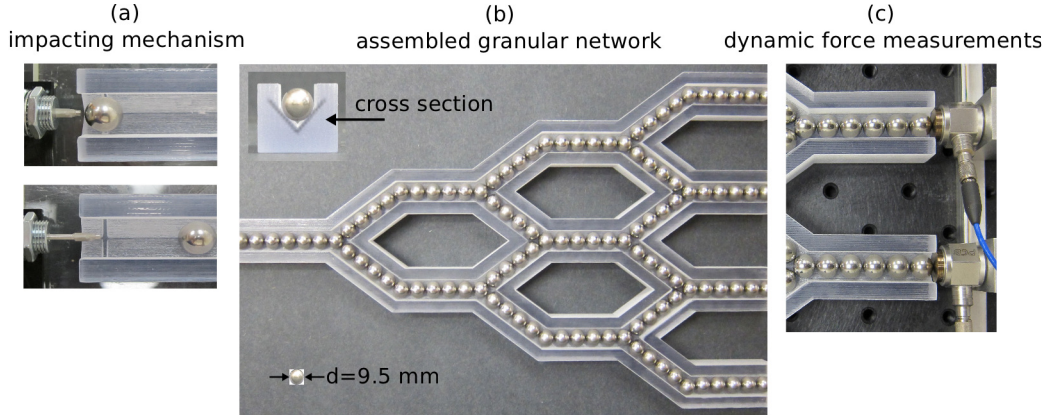


Figure 6.2: Pictures of experimental setup. (a) Solenoid impacting mechanism. (b) Assembled granular network with inset showing the v-shaped cross section of the supporting channel structure. (c) Dynamic force measurements taken at each branch end.

In order to investigate the effect of multiple splittings through a granular network, individual channel structures were printed for networks of various degrees, from $N = 1$ up to $N = 4$. Let us note that the case $N = 1$ corresponding to y-branched granular systems have been investigated in several works [111, 117, 118, 128], providing a detailed description of the wave splitting mechanism. Precise alignment of the spheres in each network is crucial to ensure simultaneous arrival of pulses at branch junctions and observe recombinations of solitary waves in experiments. The supporting channel structures were fabricated with a v-shaped cross section to guarantee particle alignment, as shown in the inset of Fig. 6.2(b). A slight tilt (approximately 2°) was induced on the experimental assembly to promote particle contacts in the network. Force measurements were taken at each of the branch ends (refer to Section 2.2.3). The assembled systems were excited by a single striker sphere, identical to the spheres

in the network. The striker sphere was given an initial velocity with a solenoid mechanism (see Fig. 6.2(a)). To capture the variability between experiments, each network with $N = 1$ to $N = 4$ was disassembled and reassembled five times, with five impacts on each initial assembly. The incident solitary wave amplitude was determined to be $48.7N \pm 2.2N$, based on repeated impacts of an $N = 0$ system consisting of 10 spheres. This average impacting force corresponds to a striker velocity of $v_{\text{striker}} = 0.44$ m/s, based on numerical simulations.

We studied the initial pulse propagation along the excited chains within the network, focusing on the leading, i.e., largest, pulse amplitudes at each exit branch location. Results from the theoretical predictions (Section 6.2), are compared with experiments and numerical simulations (Section 2.3.1).

6.2 Theoretical Approach: Quasi-Particle Theory

The combination of discreteness and nonlinear contacts between particles causes excitations along uncompressed uniform chains of spheres to travel as single solitary waves or trains of solitary waves (refer to Section 1.2.1). Individual solitary waves have specific properties determined by the size and material of the underlying particles, and each pulse travels unchanged along the length of a chain. Due to their nature, each solitary wave traveling through the chains can be modeled as a single particle with an equivalent momentum and kinetic energy. The effective or quasi-particles have a mass m_{eff} and velocity V_{eff} which are related to the mass m of the individual spheres and the velocity V_{SW} of the solitary wave [68, 118] by

$$m_{\text{eff}} = 1.345 m, \quad (6.1)$$

$$V_{\text{eff}} = 1.385 \left(\frac{\sqrt{5}}{2} \right)^4 \left(\frac{\pi \rho (1 - \nu^2)}{2E} \right)^2 V_{\text{sw}}^5. \quad (6.2)$$

Using the quasi-particle approach has practical advantages for the network of granular chains studied here: it greatly simplifies the wave transmission calculations

through bends and junctions by modeling them as a series of hard sphere collisions between quasi-particles, where the incident quasi-particle mass and velocity are always known. The velocity of the impacted quasi-particle is then calculated via conservation of linear momentum and energy, similar to the procedure described in [118]. All particle masses, and thus effective particle masses, are identical for the present study. Utilizing the relationship between the effective quasi-particle velocity, solitary wave speed, and solitary wave force amplitude (leading to $V_{\text{eff}} \propto F_{\text{sw}}^{5/6}$), the transmission coefficients through the granular chain network can be derived.

Wave propagation through the chain network involves three elementary mechanisms that are depicted in Fig. 6.3 (Top): (1) pulse splitting (S) when a chain splits into two symmetric branches, (2) wave propagation through a chain with a corner (C), and (3) pulse recombination when two identical branches merge together (M). Their effect on the wave behavior can be fully described by introducing the transmission coefficients T_S , T_C and T_M , respectively, that provide the ratio of the amplitude of the transmitted over the incident leading pulse through these junctions and corners.

Wave splitting In a previous study, [118] studied experimentally and numerically, the wave transmission along a chain that branches into two new chains. They confirmed the relevance of the quasi-particle approach to characterize wave splitting and showed that for a symmetric branching, as the one involved in our chain networks, the wave amplitude F_{sw}^t in the two new branches is proportional to the incident wave amplitude (F_{sw}^i) and follows

$$T_S = \frac{F_{\text{sw}}^t}{F_{\text{sw}}^i} = \left(\frac{2 \cos \alpha}{2 \cos^2 \alpha + 1} \right)^{6/5}. \quad (6.3)$$

Wave propagation through bend chains The transmitted amplitude through a corner with bend angle α can be described by considering a binary collision between the incident quasi-particle (initial velocity V_{eff}^i , and “post-collision” velocity V_{eff}^r) and the impacted quasi-particle (“post-collision” velocity V_{eff}^t). Assuming complete transfer of linear momentum along an axis parallel to the transmission branch through the

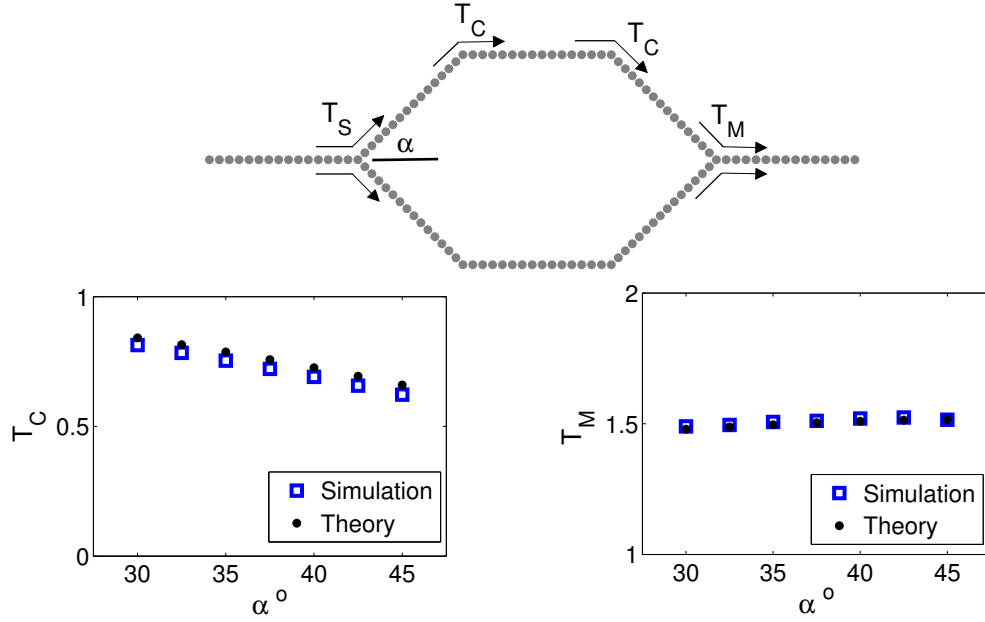


Figure 6.3: (Top) Schematic diagram of a unit cell configuration depicting the splitting transmission coefficient T_S , the corner transmission coefficient T_C and the recombination transmission coefficient T_M . (Bottom) Comparison of numerical simulations and theoretical predictions for T_C (Left) and T_M (Right) for branch angles α between 30 and 45 degrees. In numerical simulations, the incident and transmitted amplitudes were calculated using the average maximum force from particles 7 through 11 along each segment.

bend, we obtain the following expression: $m_{\text{eff}} V_{\text{eff}}^i \cos \alpha = m_{\text{eff}} V_{\text{eff}}^t$. Solving for $\frac{V_{\text{eff}}^t}{V_{\text{eff}}^i}$ and relating the effective quasi-particle velocity to the solitary wave force amplitude using $\frac{V_{\text{eff}}^t}{V_{\text{eff}}^i} = \left(\frac{F_{\text{sw}}^t}{F_{\text{sw}}^i} \right)^{5/6}$, the resulting transmission coefficient through a corner is:

$$T_C = \frac{F_{\text{sw}}^t}{F_{\text{sw}}^i} = (\cos \alpha)^{6/5}. \quad (6.4)$$

Under this assumption, the energy lost by the leading pulse through a corner is related to the component of the incident particle velocity perpendicular to the transmission branch, before and after the binary quasi-particle collision, given by $V_{\text{eff}}^i \sin \alpha$. As a result, this energy lost through branch bends is $\frac{1}{2} m_{\text{eff}} (V_{\text{eff}}^i \sin \alpha)^2$, leading to a ratio of energy lost by the leading pulse over the incident energy $\frac{E_d}{E^i} = \sin^2 \alpha$.

Wave recombination The recombination junctions are modeled as two incident quasi-particles symmetrically impacting a single transmission quasi-particle. It is assumed that the incident, or impacting spheres, travel after the collision with a reflected velocity coincident with the impact velocity, a physical constraint imposed by the supporting channel system. Momentum along y is conserved by symmetry, and conservation of momentum along x gives the following relation between the effective velocity V_{eff}^i of the incident quasi-particles, the reflected velocity V_{eff}^r of the incident quasi-particles, and the transmitted velocity V_{eff}^t of the impacted quasi-particle, leading to $2m_{\text{eff}}V_{\text{eff}}^i \cos \alpha = 2m_{\text{eff}}V_{\text{eff}}^r \cos \alpha + m_{\text{eff}}V_{\text{eff}}^t$. Conservation of energy during the collision between the three particles is expressed as $2\frac{1}{2}m_{\text{eff}}(V_{\text{eff}}^i)^2 = 2\frac{1}{2}m_{\text{eff}}(V_{\text{eff}}^r)^2 + \frac{1}{2}m_{\text{eff}}(V_{\text{eff}}^t)^2$. Using $\frac{V_{\text{eff}}^t}{V_{\text{eff}}^i} = \left(\frac{F_{\text{sw}}^t}{F_{\text{sw}}^i}\right)^{5/6}$, the transmission coefficient when pulse recombination is involved is

$$T_M = \frac{F_{\text{sw}}^t}{F_{\text{sw}}^i} = \left(\frac{4 \cos \alpha}{2 \cos^2 \alpha + 1}\right)^{6/5}. \quad (6.5)$$

In order for pulses to recombine, the incident pulses in the upper and lower branches must have identical wave structures and arrive at a chain junction simultaneously. At some chain merging locations, the leading pulses traveling in the upper and lower incident branches will arrive with unequal amplitudes (and at separate times) as a result of differing propagation path histories within the granular chain network. Therefore, not all chain merging locations result in pulse recombination. To describe the leading pulse amplitude transmission, chain merging junctions are modeled either as recombination junctions or as corners, depending on the incident upper and lower branch wave structure, as detailed on Fig. 6.4.

For $\alpha < 45^\circ$, we observed a reflected wave at the splitting junctions, but not at the corner nor the recombination junctions. For both the theoretical quasi-particle predictions and numerical simulations, the incident hard spheres at recombination junctions were observed to possess a forward velocity after the collision, relative to the direction of their initial velocity. The continued forward momentum of the impacting effective particles produced a secondary solitary wave train [67, 68] in the recombination transmission branch. The amplitude of the secondary transmitted

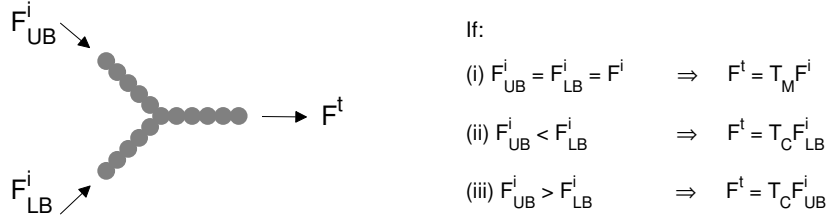


Figure 6.4: Schematic diagram describing the choice of transmission coefficient used to model the transmitted leading pulse amplitude F^t at junctions where two granular chains merge together. F_{LB}^i and F_{UB}^i denote the incident force amplitudes in the lower and upper branch, respectively.

solitary wave decreases with increasing α . The amplitude of the secondary wave train is small with respect to the leading pulse, and we will focus on the latter in the remainder of this study. The theoretical predictions for T_C and T_M are in excellent agreement with those obtained from numerical simulations for branch angles between 30° and 45° , as shown in Fig. 6.3. The expressions for the transmission coefficients given by Eqs. (6.3), (6.4) and (6.5) serve now as elementary bricks to predict the overall acoustic behavior of the networks of granular chains.

6.3 Wave Propagation Path

Experiments and numerical simulations are performed for each of the $N = 1$ up to $N = 4$ granular networks described in Section 6.2 (also pictured in Fig. 6.5 (Left)). In numerical simulations, the last branch segments were extended by five particles, to obtain an average transmitted amplitude through the exit channel corresponding to the end particle in experiments. While exact force profiles varied slightly between the five experiments on each N network due to slightly different arrangements of particles within the channels, the general features including the number of pulses arriving at the branch ends and the relative amplitudes of each pulse were consistent over all experiments. Figure 6.5 depicts the normalized force profiles at each of the $N + 1$ exit branches in both numerical simulations (middle panel) and a single experiment

(right panel) randomly chosen among the five assemblies and the five impacts for each of the $N = 1 - 4$ networks. The small trailing oscillations observable in the $N = 1$ and 2 experiments are the result of the last sphere-sensor interaction, and are not an inherent feature of the network structure.¹ Overall, experiments and simulations are in good qualitative agreement for all of the experimentally tested networks.

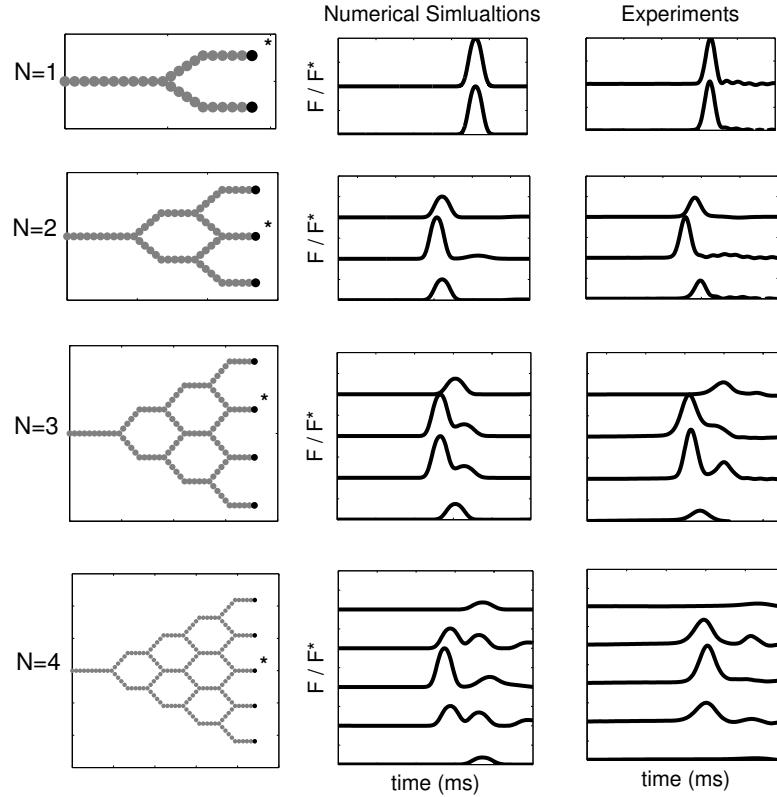


Figure 6.5: Numerical simulations and experimental results of the force profiles at each branch end for the tested $N=1$ through $N=4$ networks. (Left) Schematic diagram of the branch network for each level. The force profiles correspond to particles denoted in black. For each level, the amplitude was normalized by the amplitude of particle*. (Middle) Numerical simulations and (Right) a single experimental test for each of the tested networks ($N=1-4$). The force profiles of each branch end are offset by 1 N for visual clarity. Y-ticks denote 0.5 N and x-ticks denote 0.1 ms.

¹The larger amplitude pulses that cross the $N = 1$ and 2 networks correspond to shorter temporal wavelengths, resulting in higher frequency waves which slightly resonate with the sensors.

6.3.1 Central, Largest Leading Pulse

Experiments and numerical simulations are compared more quantitatively on the left panel of Fig. 6.6 where the transmitted wave amplitude $F_{\text{middle}}^{\text{t}}$ in the middle branch is represented as a function of the network level N . For N even networks, the force is directly measured on the central branch (marked by a star sign on the left panel of Fig. 6.5), while for N odd, this value is extrapolated from the transmitted amplitude measured in the other exit chains according to a procedure described below. For experiments and numerical simulations, an exponential law can be used to describe the decay of the transmitted wave amplitude in the central branch as a function of the level N of the network:

$$F_{\text{middle}}^{\text{t}} = F^{\text{i}} e^{-\frac{N}{N_0}} \quad (6.6)$$

where the actual value of N_0 is obtained from the exponential fit of the data shown in Fig. 6.6 and listed in Table 6.1. Here, F^{i} is the force amplitude of the incident wave generated by the impact of the striker. This behavior means that granular chain networks are very efficient for mitigating waves, and systems of size $N \gg N_0$ will be preferentially chosen for designing strongly mitigating metamaterials. In experiments, the effects of dissipation in isolated chains is evident and results in wave amplitude decay through each chain, and consequently a lower value of N_0 compared to the conservative simulations. However, the description of $F_{\text{middle}}^{\text{t}}$ by an exponential decay remains fairly good.

To understand such a property of the chain network, we use the theoretical description proposed in Section 6.2 to predict the effective acoustic behavior of the network. As illustrated in Fig. 6.1, one can predict the property of the transmitted wave by following its path through the network from the initial chain until the central exit chain. Since the wave velocity decays with its amplitude, only some of the various paths linking the entry to the exit of the network will contribute to the central leading pulse. Here, the largest pulses will result from the propagation through the central chains of the network. For example, for $N = 2$, the central transmitted pulse is the result of two wave splitting processes, the propagation of the wave through

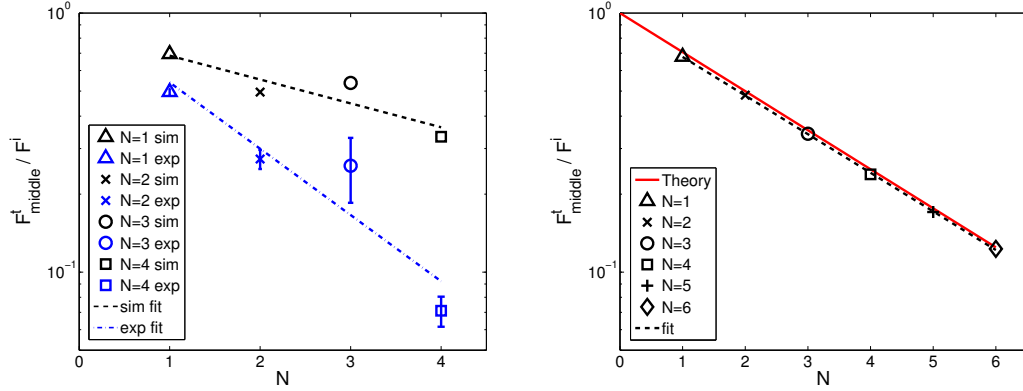


Figure 6.6: F_{middle}^t (normalized by the input force, F^i) as a function of branch levels, N . (Left) Numerical simulations are represented in black markers and experimental results in blue markers for $N = 1 - 4$ for the tested network with six particles per chain. The linear fit through the simulation data is represented by a dotted black line and the linear fit through the experimental data by a dot-dashed blue line. (Right) Numerical simulations are represented in black markers for $N = 1 - 6$ for the network with 16 particles per chain. The linear fit through the simulation data is represented by a dotted black line and the theoretical predictions by a solid red line.

one corner, and one wave recombination, leading to $F_{\text{max}}^{t-\text{theory}}(N = 2) = F^i T_S^2 T_C T_M$. To move from $N = 2$ to $N = 4$ – as from any network of level N to another one of level $N + 2$ – the wave will go through the same four processes again, leading to the predictions

$$\begin{cases} F_{\text{max}}^{t-\text{theory}}(N) = F^i (T_S)^N (T_C)^{N/2} (T_M)^{N/2} & \text{for } N \text{ even networks} \\ F_{\text{max}}^{t-\text{theory}}(N) = F^i (T_S)^N (T_C)^{\frac{N+1}{2}} (T_M)^{\frac{N-1}{2}} & \text{for } N \text{ odd networks} \end{cases} \quad (6.7)$$

For N even, $F_{\text{max}} = F_{\text{middle}}$. Rearranging Eq. (6.7) and using the expressions of the transmission coefficients T_S , T_C and T_M given in Section 6.2, one can predict the amplitude of the largest transmitted pulse for a chain network with even N

$$F_{\text{middle}}^{t-\text{theory}}(N) = F^i e^{-\frac{N}{N_0^{\text{th}}}} \quad \text{with} \quad N_0^{\text{th}} = \frac{5}{12 \log \left(\frac{(1+2 \cos^2 \alpha)^{3/4}}{2 \cos \alpha} \right)} \quad (6.8)$$

For N odd, extrapolating F_{middle} from the spatial repartition of leading pulse amplitudes, result in the same expression for N_0 (see below).

Our theoretical approach captures the exponential behavior of the central leading pulse observed in the granular chain network, suggesting that wave splitting in the network is here the dominant mechanism. However, the theoretical value of $N_0^{\text{th}} = 2.88$ for the branching angle $\alpha = 35^\circ$ used in the experimental and numerical networks, with 6 particle chain lengths, compares rather poorly with the measured decay rate N_0 given in Table 6.1. This discrepancy comes from the limited number of particles in each chain, while our theory assumes long chains. For long chains, pulses of different amplitudes propagating in the granular network will have sufficient propagation distance to separate and arrive at different times at the next junction since the solitary wave velocity is a slowly increasing function of its amplitude, with $V_{SW} \propto F_{SW}^{1/6}$. For the six particle chains used in both the experiments and the numerical simulations, the arrival time of waves at chain merging junctions is not sufficiently different to avoid some overlap between the primary pulse and trailing pulses. The pulse overlapping is most clearly seen in the pulse structure reaching the central exit branches in the $N = 3$ network shown in Fig. 6.5. As a result, the transmitted amplitude is slightly underestimated in our model, and the measured value for N_0 is larger than the predicted one.

To test this idea, we simulated wave propagation in a network with a larger number of particles in each chain. The amplitude of the central transmitted pulse is shown in the right panel of Fig. 6.6 as a function of the system size, for network degrees up to $N = 6$ and individual chains consisting of 16 particles. Our observations for these numerical simulations of long branch network ($N_0 = 2.9$) are in excellent agreement with the theoretical exponential decay ($N_0^{\text{th}} = 2.88$).

6.3.2 Spatial Repartition of Transmitted Leading Pulses

We now go beyond the wave transmission in the middle exit chain, and study the full distribution of transmitted wave amplitudes as a function of the normalized distance r to the middle axis of the network (see Fig. 6.1). Here, $r = 0$ corresponds to the middle exit chain while $r = 0.5$ and $r = -0.5$ correspond to the side exit chains.

For symmetry reasons, we will focus only on the values of the transmitted amplitude $F^t(r)$ for positive values of r . The spatial repartition of the leading pulses are shown in the inset of Fig. 6.7(left) for various network sizes N for both simulations and experiments. After normalizing the ordinate by the central (largest) leading pulse amplitude F_{middle}^t and multiplying the abscissa by the network degree N , all data collapse onto two master curves: (1) experiments and (2) simulations, as shown on the main panel of Fig. 6.7(left). The linear variation in this semi-logarithmic representation suggests

$$F^t(r) = F_{\text{middle}}^t e^{-\frac{Nr}{\xi_0}} \quad (6.9)$$

The values of ξ_0 obtained from the fit of the data by an exponential spatial distribution of transmitted amplitudes are given in Table 6.1. Our numerical model captures reasonably well the spatial distribution observed in experiments as well as the value of ξ_0 , despite the important role played by dissipation, as illustrated by the mitigation of the largest pulse through the network shown in Fig. 6.6. The normalization by F_{middle}^t significantly reduces the effect of dissipation present in the experiments. The network structure not only leads to an efficient mitigation of the incident wave along $r = 0$, but also to a rapid decrease of the wave amplitude along an axis perpendicular to the line of impact. Taking now $y = Nr$ as the actual distance of the exit chain to the central one, the spatial distribution of the leading pulses $F^t(y) = F_{\text{middle}}^t e^{-\frac{y}{\xi_0}}$ indicates that the acoustic energy decreases exponentially rapidly as one moves away from the center of the network.

To understand such a strong directionality, we count the number of wave splittings, recombinations and corners along the path followed by the leading pulse reaching the branch at distance r from the middle chain (see Fig. 6.1), and describe the wave propagation using the three transmission coefficients introduced in Section 6.2. For chains with either even or odd levels N , one obtains

$$F^{\text{t-theory}}(r) = F^i \left[T_S (T_C)^{\frac{1}{2}+r} (T_M)^{\frac{1}{2}-r} \right]^N \quad (6.10)$$

Let us note that r takes a finite number of values, with $r \in \{0, \frac{1}{N}, \dots, \frac{1}{2}\}$ and $r \in \{\frac{1}{2N}, \frac{3}{2N}, \dots, \frac{1}{2}\}$ for even and odd network degrees, respectively. Using the expressions of the different transmission coefficients as a function of the branch angle α given in Eqs. (6.3), (6.4) and (6.5), the spatial distribution of the transmitted wave can be expressed as

$$F^{\text{t-theory}}(r) = F_{\text{middle}}^{\text{t-theory}} e^{-\frac{y}{\xi_0^{\text{th}}}} \quad \text{with} \quad \xi_0^{\text{th}} = \frac{5}{12 \log\left(\frac{2}{\sqrt{1+2\cos^2\alpha}}\right)} \quad (6.11)$$

Let us note that $\frac{3}{2}$ provides a rough estimate of the decreasing length scale of the wave spatial structure since $1.2 < \xi_0^{\text{th}} < 1.8$ for the range of admissible angles $30^\circ \leq \alpha \leq 45^\circ$.

The predicted value $\xi_0^{\text{th}} = 1.57$ for the angle used in the simulations and experiments overestimates the observed values given in Table 6.1. Here again, overlap of primary and trailing pulses occur at chain merging junctions with different amplitude waves in the upper and lower branches for the short (6 particles) branch networks. This overlap is not accounted for in our theoretical model which simplifies these unsymmetrical chain junctions as corners (Fig. 6.4), resulting in an underestimation of the transmitted amplitude at several exit branches within the network. The neglected pulse overlapping is more prevalent for central exit branches, i.e., for small values of r . In order to obtain a better comparison with the theoretical predictions, we performed simulations of wave propagation for long branches networks, which allow sufficient time for waves taking different and non-equivalent paths to separate and avoid solitary wave overlapping. Spatial distributions of transmitted amplitudes for the 16 particle chain networks with $N = 1$ up to $N = 6$ are represented on the right panel of Fig. 6.7. Once renormalized by $F_{\text{middle}}^{\text{t}}$, and plotted as a function of the actual distance $y = rN$, the numerical results compare well with the predicted spatial distribution given in (Eq. 6.11). Table 6.1 summarizes the values of ξ_0 and N_0 obtained from experiments and numerical simulations of the short branch tested networks, as well as the numerical simulations performed for the long branch

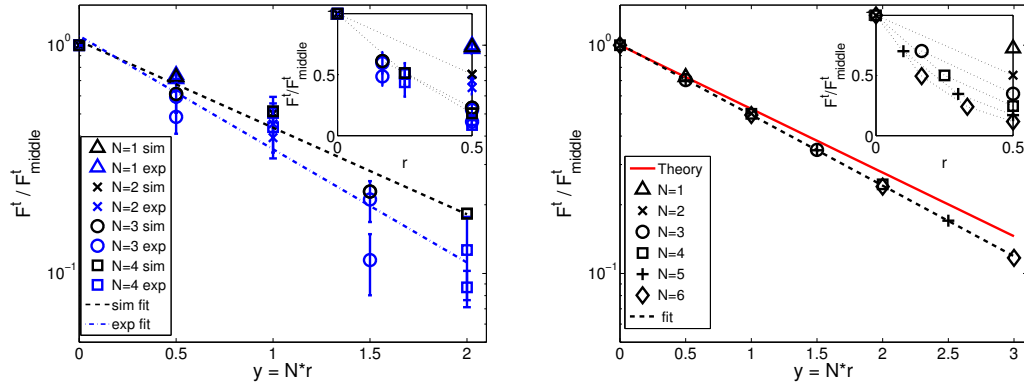


Figure 6.7: Spatial repartition of the normalized transmitted force F^t/F^t_{middle} as a function of the distance $y = Nr$ to the middle axis of the network. The insets show the force spatial distribution F^t/F^t_{middle} as a function of the normalized distance r . (Left) Numerical simulations are represented in black markers and experimental results in blue markers for $N = 1 - 4$ for networks with six particles per chain. The linear fit through the simulation data is represented by a dotted black line and the linear fit through the experimental data by a dot-dashed blue line. (Right) Numerical simulations are represented in black markers for $N = 1 - 6$ for networks with 16 particles per chain. The linear fit through the simulation data is represented by a dotted black line and the theoretical predictions by a solid red line.

networks. For $N > 1$ odd, the F^t_{middle} value was obtained through linear regression of the spatial distribution of transmitted amplitudes on the $\log(F^t)$ vs r data. For experiments, the linear regression is performed for both sides ($\pm r$) of the network in order to achieve a better precision on ξ_0 and estimate the error bar. For $N = 1$, we use the theoretical expression of ξ_0^{th} of Eq. (6.11) to get an extrapolated value of $F^t_{\text{middle}} = \exp(\log(F^t(N=1)) - 1/2 * (-1/\xi_0^{\text{th}}))$. The decay rates ξ_0 and N_0 were obtained excluding the values for $N = 1$ networks, and it was observed that this omission had a small effect on the fit of the data.

6.4 Discussion

The main mechanism of wave mitigation in the granular chain networks is rather clear: for each additional degree added to the network, the leading pulse splits into two new pulses, so the acoustic energy of the leading pulse after N branchings decays

Table 6.1: Comparison of the decay length scales N_0 and ξ_0 for theoretical predictions, long branch network (16 particles per branch) numerical simulations and short branch network (6 particles per branch) experiments and numerical simulations

	Theory	Long Branch Simulation	Short Branch Simulation	Short Branch Experiment
N_0	2.88	2.9	4.7	1.7
ξ_0	1.57	1.4	1.1	0.9

as

$$E^t(N) = (T^E)^N E^i = E^i e^{-\frac{N}{N_0}}, \quad (6.12)$$

where we introduce here the transmission coefficient $T^E < 1$ in terms of transferred acoustic energy through one stage of the granular chain network. Using the relationship between energy and force amplitude of solitary waves $E \sim F^{5/3}$, the transmission coefficients derived in Section 6.2 can be expressed in terms of energy, $T_K^E = (T_K)^{5/3}$ where $K \in \{S, C, M\}$. A rough description of the granular chain network would be to assume that the acoustic energy divides into two equal parts at each new level, resulting in $T^E = 1/2$ and $E^t(N) = \frac{E^i}{2^N}$. This would capture only qualitatively the overall behavior of the metamaterial designed here since wave recombinations as well as wave reflections can occur at branches and corners. As a result, the actual value of the effective transmission coefficient depends on the exit chain considered, and for the middle chain where the transmitted wave has the highest energy, one obtains

$$T_{\text{middle}}^E = \left(T_S \sqrt{T_C T_M} \right)^{5/3} = \frac{16 \cos^4 \alpha}{(1 + 2 \cos^2 \alpha)^3} \quad (6.13)$$

with $1/2 \leq T_{\text{middle}}^E < 0.58$ for the range of admissible branching angles $30^\circ \leq \alpha \leq 45^\circ$. This energy transmission coefficient is related to the rate N_0 of the exponential decay by the relation $N_0 = \frac{-5}{3 \log(T_{\text{middle}}^E)}$.² Considering now the exit chains located on the very side of the network (see Fig. 6.1), one can show that the overall transmission coefficient that results from the propagation of the wave through the side branches

²We need to use here the relation between both types of transmission coefficient $T_{\text{middle}}^E = (T_{\text{middle}})^{5/3}$ and observe from Eq. (6.8) that $N_0 = -\frac{1}{\log(T_{\text{middle}})}$ where $T_{\text{middle}} = T_S \sqrt{T_C T_M}$ is the transmission coefficient through one stage of the network in terms of wave amplitude.

of the network follows

$$T_{\text{side}}^E = (T_S T_C)^{5/3} = \frac{4 \cos^4 \alpha}{(1 + 2 \cos^2 \alpha)^2} \quad (6.14)$$

and is comprised within $1/4 \leq T_{\text{side}}^E < 0.36$ for the range of admissible branching angles. Transmission coefficients for both middle and side branches are represented in Fig. 6.8 as a function of the branching angle together with the results of simulations. In numerical simulations, T_{middle}^E and T_{side}^E were calculated from the fitted N_0^{middle} and N_0^{side} values obtained for long branch networks with $N = 1$ though $N = 6$ with α varying between 30° and 45° , using the relation $N_0 = \frac{-5}{3 \log(T^E)}$. The agreement between the numerical simulations and the theoretical predictions of both T_{middle}^E and T_{side}^E is quite good.

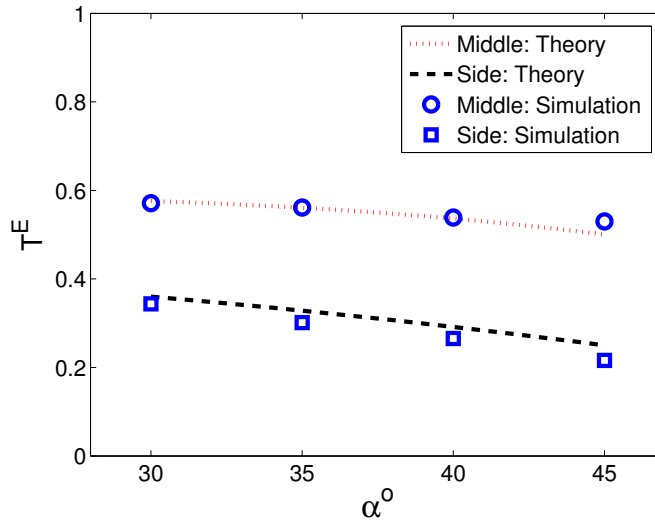


Figure 6.8: Variations of the transmission coefficient T^E in terms of transferred acoustic energy through one stage of the granular chain network for the middle and side exit chains for both theoretical predictions (see Eq. (6.13) and (6.14)) and numerical simulations of the long branch (16 spheres per segment) networks with variable branching angles α . The overall transmitted acoustic energy follows $E^t = E^i (T^E)^N$.

The remarkable ability of granular chain networks to efficiently mitigate the acoustic energy of the largest wave in the system emerges from their branched structure. Due to the underlying branched structure, the spatial distribution of acoustic en-

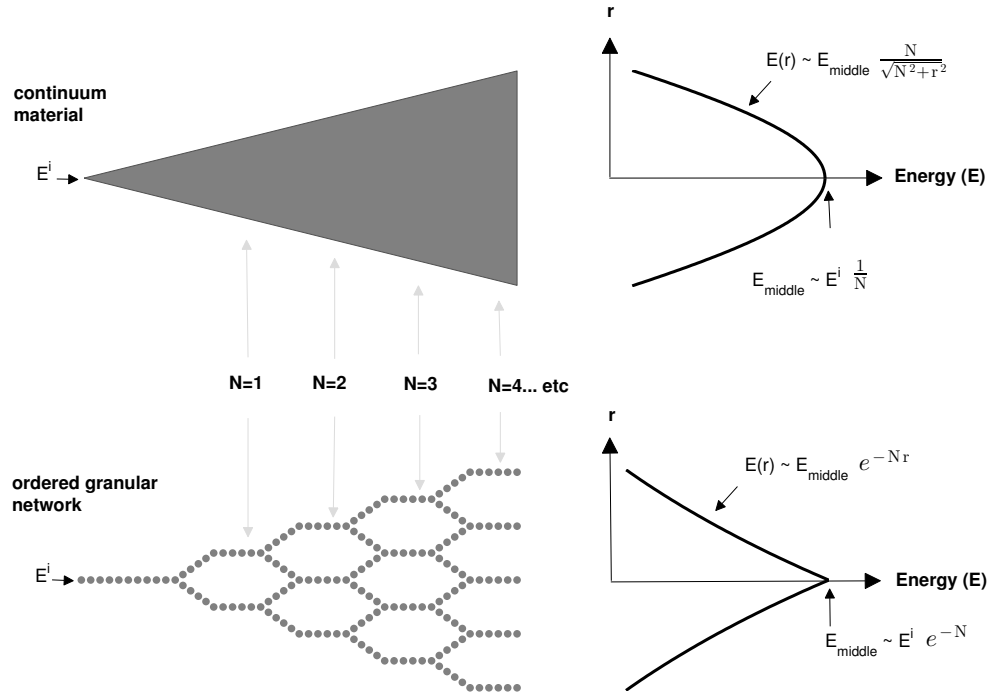


Figure 6.9: (Top) Spatial distribution of the energy of a harmonic wave transmitted through a conventional 2D continuum material. (Bottom) Spatial distribution of acoustic energy in ordered granular networks (granular acoustic metamaterial).

ergy is also fundamentally different than the wave front energy distribution through a conventional continuum material (see Fig. 6.9). In a non-dissipative 2D elastic medium, the elastic energy density of a harmonic wave is shown to decay as $1/N$ with the distance N from a localized excitation, invoking energy conservation. More generally, a power-law decay of the elastic energy is expected for either linear or non-linear acoustic media. Similarly, the wave spatial structure at a distance N follows a power-law behavior, as shown in Fig. 6.9 (Top). Conversely, the granular chain network exhibits a drastically faster decay of the energy carried in the leading pulse: exponential decay of both the central leading pulse with propagation distance and the spatial repartition of the transmitted wave with the distance to the central axis (Fig. 6.9 (Bottom)). The theoretical predictions also indicate that the exponential

decay occurs over relatively short length scales. Specifically, the values of the decay length scales N_0 and ξ_0 suggest that the $N = 3$ network is already a highly effective acoustic wave mitigating structure. An additional benefit of the granular networks is the low effective density compared to a conventional bulk material. While ordered networks of homogeneous granular chains are proven to be an effective wave mitigating structure, even more efficient granular acoustic metamaterials could be designed. For example, chains of different materials could be introduced within the network to tune the wave velocity and prevent pulse recombinations and to increase the ratio of reflected to transmitted wave amplitudes. Additionally, a honeycomb structure could be designed to produce mitigating behavior when the system is excited from either the left or right side.

Beyond these interests for engineering applications, our model system also provides new insights into wave propagation in disordered granular media. The dynamic behavior of granular materials is not well understood, yet it plays an important role in many areas of industry and research ranging from agriculture and construction to modeling earthquakes and avalanches. In tightly packed granular media, several previous studies showed that the dynamic force transmission occurs along force chains, following preferred loading paths within the contact network (refer to Section 1.3). Our system contains all the relevant ingredients to capture the physics of wave propagation through force chain networks: wave splitting, bending, and recombination. As a result, we expect the ordered granular network presented here to qualitatively capture the behavior of disordered granular media. In terms of effective acoustic response, the exponential mitigation of the wave amplitude identified in this study for ordered granular packings is also observed in disordered packings [148]. In addition, the spatio-temporal structure of the wave transmitted through ordered and disordered granular media shares qualitatively many common features: after a dominant leading pulse that has been the main focus of our study, we also observe a train of smaller solitary waves resulting from wave propagation through alternative and less direct paths (see [158] for similar observations in random packings). Interestingly, due to pulse recombinations, it is not impossible to observe that the largest transmitted

pulse is actually not the leading one for some special network configurations, as also reported for random networks. Let us note that dissipation present in real systems will affect the actual rate of mitigation. Comparing our dissipative experiments with the conservative numerical simulations, we observed that the rate of mitigation due to wave splitting and dissipation are of the same order for the short branch networks. This ingredient should also be included in a realistic model of wave propagation in natural granular materials.

6.5 Summary of Results

We studied the transmission of elastic waves through ordered granular chain networks with variable branch angles. We identified three main physical mechanisms involved during this process: wave splitting, wave bending through corners, and wave recombination at merging junctions. Solitary wave splitting was previously observed [117, 118, 128], however, we present the first observation and theoretical description of two identical solitary waves combining. The quasi-particle theory was used to describe these mechanisms, and derive the effective acoustic properties of the granular acoustic metamaterial from the geometrical properties of the network and the bead properties. Numerical simulations for long branch networks up to branching level $N = 6$ are in good quantitative agreement with our theoretical approach for both the exponential decay of the central leading pulse with propagation distance and the spatial repartition of the transmitted wave with the distance to the central axis. Experiments and numerical simulations of a short branch system for N up to 4 are also in good qualitative agreement with the predicted exponential decay of the leading central pulse amplitude and the spatial repartition of the leading pulses along r . However, the short branch system does not always provide a long enough propagation distance for leading and trailing pulses to separate, and pulses overlapping results in an increased wave amplitude compared to the quasi-particle predictions which only account for the leading pulses. Additionally, the effects of dissipation present in experiments reduce the leading pulse amplitude faster than in our theoret-

ical model. Overall, the exponential decay of leading pulse amplitudes through the ordered granular network makes these systems ideally suited for wave mitigation applications. Furthermore, the exponential decay of wave amplitude with propagation distance in our ordered granular network compares well with the wave propagation features along force chains in disordered granular media [148]. This ordered version of natural granular materials offers the possibility to understand in all its details the acoustic behavior of a granular medium and (i) relate microstructural characteristics with effective acoustic properties in this type of materials and (ii) choose adequately the material microstructure to achieve desired acoustic response like a high mitigation rate.

Chapter 7

Ordered Granular Network: 3D

We study the pulse propagation through an ordered 3D network of interconnected granular chains. This study is a direct extension of the ordered 2D networks presented in Chapter 6, into a fully 3D geometry. The quasi-particle model is extended to describe the pulse splitting, bending, and combing mechanisms through the engineered 3D waveguide network of granular chains. The granular network geometry allows for spatial and temporal redistribution of the acoustic waves from an impact. Similar to the 2D network, the nonlinear waves supported by the structure of the bead chains combined with the hierarchal branching geometry results in an exponentially rapid decay of the leading pulse amplitudes. These systems not only exhibit reversible deformation and effectively function over all frequencies, but also have the added benefit of a low relative density. The excellent agreement between experiments and theoretical predictions (and numerical simulations) validates the wave guiding capabilities of these 3D networks and opens a wide range of possibilities for the realization of increasingly complex structured granular material design.

7.1 Problem Description and Approach

The relatively simple 3D network geometry, i.e., symmetric branching and identical branch segment properties, was chosen to simplify the response of the system while still capturing all fundamental physical mechanisms relevant for a general 3D network structure: pulse splitting, bending, and combining. The constructed gran-

ular networks are composed of chains of stainless steel spheres held in place by a polymer supporting channel structure. The supporting channel structures are 3D printed in a modular fashion: separate sections for straight segments, bends (or 2-channel junctions), 3- and 4-channel junctions, which can then be assembled into networks of variable size N (see Figure 7.1a and b). For the present study, we tested 3D network geometries $N = 1$ up to $N = 3$. The minimum physical branch angle, $\alpha_{min} = \arcsin 1/\sqrt{3} \approx 35.3^\circ$, in the 3D network occurs when the first particle in the three transmission branches come into contact. The experimental branch angle was chosen to maximize the transmitted forces (see below) while maintaining experimental feasibility by allowing for a small gap between branching particles, thus experiments were performed for network geometries with a branch angle $\alpha = 40^\circ$. The chain lengths in experiments were chosen to be 6 particles in order to minimize the effects of dissipation while still allowing for full support of the traveling solitary waves (recall $\lambda_{sw} \approx 5d$). The spheres used in experiments are stainless steel (type 440C) with diameter $d = 9.5$ mm. The supporting channel structures are fabricated using VeroClear material with the Connex 500 3D printing system, with a circular inner cross section large enough to allow free motion of the sphere chains, while small enough to maintain the desired particle alignment.

To excite the network, each granular system was impacted with a single striker sphere, identical to those composing the network, at the entrance chain. The striker impact velocities were calculated from the measured striker sphere drop height. To capture the variability between experiments, each network with $N = 1$ up to $N = 3$ was disassembled and reassembled 7 times, with 10 impacts on each initial assembly. For the $N = 1, 2$ and 3 networks, the average impact velocity was $V_{striker} = 0.39, 0.55$ and 0.88 m/s , respectively. The impact force was increased with system size N in order to transmit measurable signals at each of the branch ends, where the force measurements were obtained with piezoelectric dynamic force sensors (refer to Section 2.2.3). We studied the pulse propagation along the excited chains within the network, focusing on the leading, i.e., largest, pulse amplitudes at each exit branch location. Results from the theoretical predictions (Section 7.2), are compared with experiments

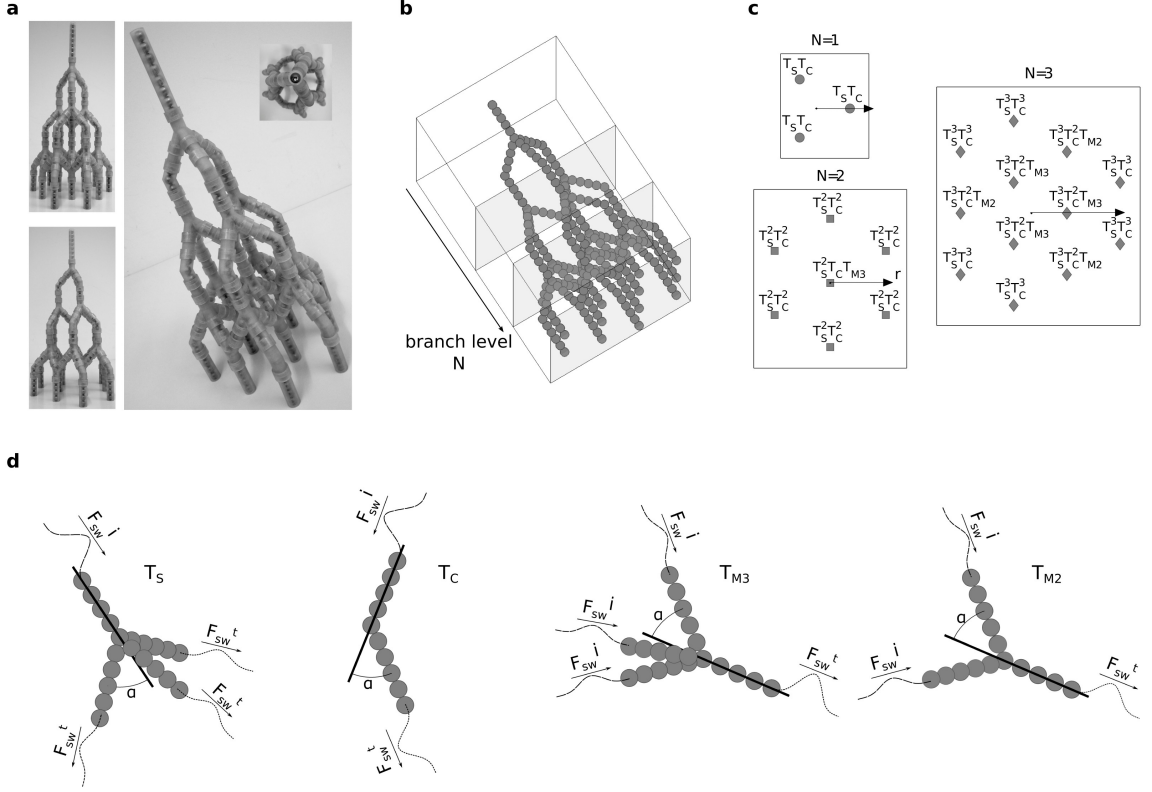


Figure 7.1: (a) Pictures of the $N = 3$ experimental setup. (b) Schematic diagram of granular network geometry, and definition of branch level, N . (c) Transmission coefficients at each of the branch ends for networks with branching level $N = 1, 2$, and 3. (d) Schematic diagram describing the four different transmission coefficients: T_S wave splitting, T_C bending, T_{M3} 3 identical incident pulses combining, and T_{M2} 2 identical pulses combining at incident angle α

and numerical simulations (refer to Section 2.3.1).

7.2 Theoretical Approach: Quasi-Particle Theory

In this section, we use the quasi-particle model to derive the relevant transmission coefficients through the presented 3D granular network geometry. Since the procedure is similar to that described in Section 6.2, where detailed derivations were provided, here we present only the required assumptions and main results.

Tracking an initial pulse through the present granular network, we find that the transmitted pulse amplitudes at each branch end can be described by variable combi-

nations of 4 transmission coefficients: (i) T_S , incident pulse splitting into 3 equivalent transmitted pulses along branches at angle α , (ii) T_C , incident pulse bending at corners with angle α , (iii) T_{M3} , 3 identical incident pulses combining into a single transmitted pulse at angle α , and (iv) T_{M2} , 2 identical incident pulses combining into a single transmitted pulse at angle α . The schematic diagram in Figure 7.1d illustrates the four transmission coefficients within the network geometry. The transmission coefficients were first derived in terms of the incident and transmitted effective particle velocities $V_{\text{eff}}^t/V_{\text{eff}}^i$, or pre- and post-“collision” quasi-particle velocities, from conservation of kinetic energy and linear momentum. To compare with experiments, the transmission coefficients were converted to force amplitude, based on the known relationships $V_{\text{eff}} \propto V_{\text{sw}}^5$ and $V_{\text{sw}} \propto F_{\text{sw}}^{1/6}$.

The splitting transmission coefficient was derived analogously to the 2D case (Equation (6.3)). A single pulse splitting into 3 identical branches with branching angle α can be described by:

$$T_S = \frac{F_{\text{sw}}^t}{F_{\text{sw}}^i} = \left(\frac{2 \cos \alpha}{1 + 3 \cos^2 \alpha} \right)^{6/5}. \quad (7.1)$$

The corner transmission coefficient is identical to the 2D geometry (Equation (6.4)):

$$T_C = \frac{F_{\text{sw}}^t}{F_{\text{sw}}^i} = (\cos \alpha)^{6/5}. \quad (7.2)$$

For chain merging locations, we have three choices of transmission coefficients, depending on the relative amplitude (and therefore arrival time) of the incident pulses. For 3 identical pulses simultaneously combining into a single transmitted pulse, the transmission coefficient T_{M3} is derived similarly to Equation (6.5). Assuming the incident pulses travel at the same branching angle α before and after the merging (a physical constraint imposed by the walls), we derive the following:

$$T_{M3} = \frac{F_{\text{sw}}^t}{F_{\text{sw}}^i} = \left(\frac{6 \cos \alpha}{1 + 2 \cos^2 \alpha} \right)^{6/5}. \quad (7.3)$$

In some cases, along the outer edge of the network, only two incident branches will

merge into a transmission branch. To derive the transmission coefficient for this scenario, we follow the same procedure used to derive the merging of 2 chains in the 2D network geometry and keep only the component of the transmitted quasi-particle velocity along the direction of the transmission branch. From the 3D network geometry, we can see that the angle between two incident branches at chain merging locations, in terms of the 3D branching angle α , is $\beta = \arcsin\left(\frac{\sqrt{3}}{2} \sin \alpha\right)$. So, replacing α in Equation (6.5) with β , and multiplying by $\cos \phi$, where $\phi = \arctan\left(\frac{\tan \alpha}{2}\right)$ is the angle between the plane of the two merging branches and the transmission branch, leads to:

$$T_{M2} = \frac{F_{sw}^t}{F_{sw}^i} = \left(\frac{8\sqrt{4 - 3\sin^2 \alpha}}{3(2 - \sin^2 \alpha)\sqrt{4 + \tan^2 \alpha}} \right)^{6/5} \quad (7.4)$$

for the 3-junction merging transmission coefficient, i.e., 2 incident pulses merging into a single transmitted pulse. For network geometries with increasing size N , there will be instances where the incident pulses in 2 of the 3 interior merging chains will be equal and larger (i.e., arrive sooner), than the leading pulse in the 3rd merging chain. In this case, we also use the T_{M2} transmission coefficient along with the larger incident pulse amplitudes to describe the leading transmitted pulse amplitude. Additionally, the scenario could arise where the incident pulse in 1 of the 3 merging branches is largest (and thus arrives sooner) than the pulses in either of the 2 other merging branches. In this case, we assume that the leading transmitted pulse amplitude is effectively captured with the corner transmission coefficient, T_C , similar to the 2D network case (refer to Figure 6.4).

Numerical simulations performed for a unit cell network showed excellent agreement with all transmission coefficients T_S , T_C , T_{M3} , and T_{M2} for $\alpha_{min} < \alpha \leq 45^\circ$. For $\alpha > 45^\circ$, the presence of the confining walls in the numerical simulations slightly reduces the transmitted amplitude T_{M2} and T_{M3} at merging junctions compared to the quasi-particle predictions. A comparison of the quasi-particle transmission coefficients with the transmitted amplitudes obtained from numerical simulations is shown in Figure 7.2.

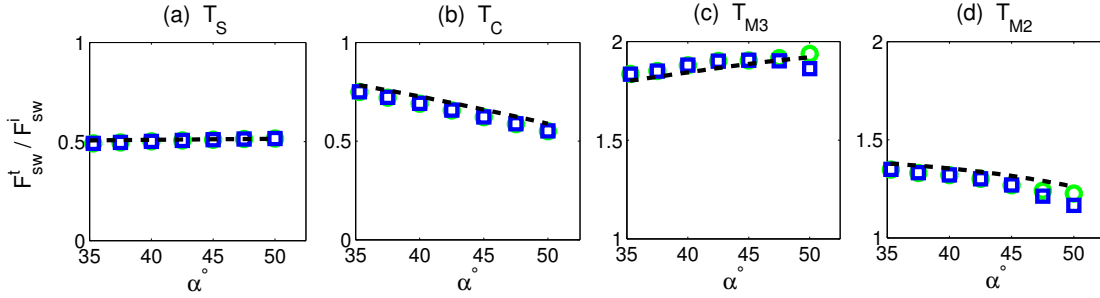


Figure 7.2: Comparison of numerical simulations and theoretical predictions for (a) T_S , (b) T_C , (c) T_{M3} and, (d) T_{M2} for branch angles α between α_{min} and 50 degrees. The dashed black line represents the quasi-particle predictions (Equations (7.1) - (7.4)). The blue squares represent the transmission coefficients calculated from numerical simulations including wall particles and the green circles from simulation without walls.

7.3 Wave Propagation Path

The initial pulse propagation through the $N = 1 - 3$ 3D granular networks results in a series of transmitted pulses reaching each of the branch ends. To describe the pulse distribution, we define r as the radial distance from the line of impact in the plane perpendicular to the branch ends, where $r = 1$ is the branch end furthest from the line of impact for any branching level N (see Fig 7.1). The largest transmitted pulse F_{max} will be observed at the at the branch ends closest to $r = 0$. For increasing system size N , the interior branch ends transmit a number of pulses of decreasing amplitude, while the edge branches always transmit only a single pulse. Figure 7.3 compares the pulse profiles from experiments and numerical simulations at each branch end for networks $N = 1 - 3$. The number and relative amplitude of pulses observed at each branch end in experiments is in good agreement with the pulse profiles predicted by the numerical simulations. The relative leading pulse amplitudes confirms the occurrences of even pulse splitting and simultaneous pulse combinations in experiments. This also suggests that any impurities in the granular network particle alignment were not significant enough to break the symmetry of the system, which would have prevented pulse recombination.

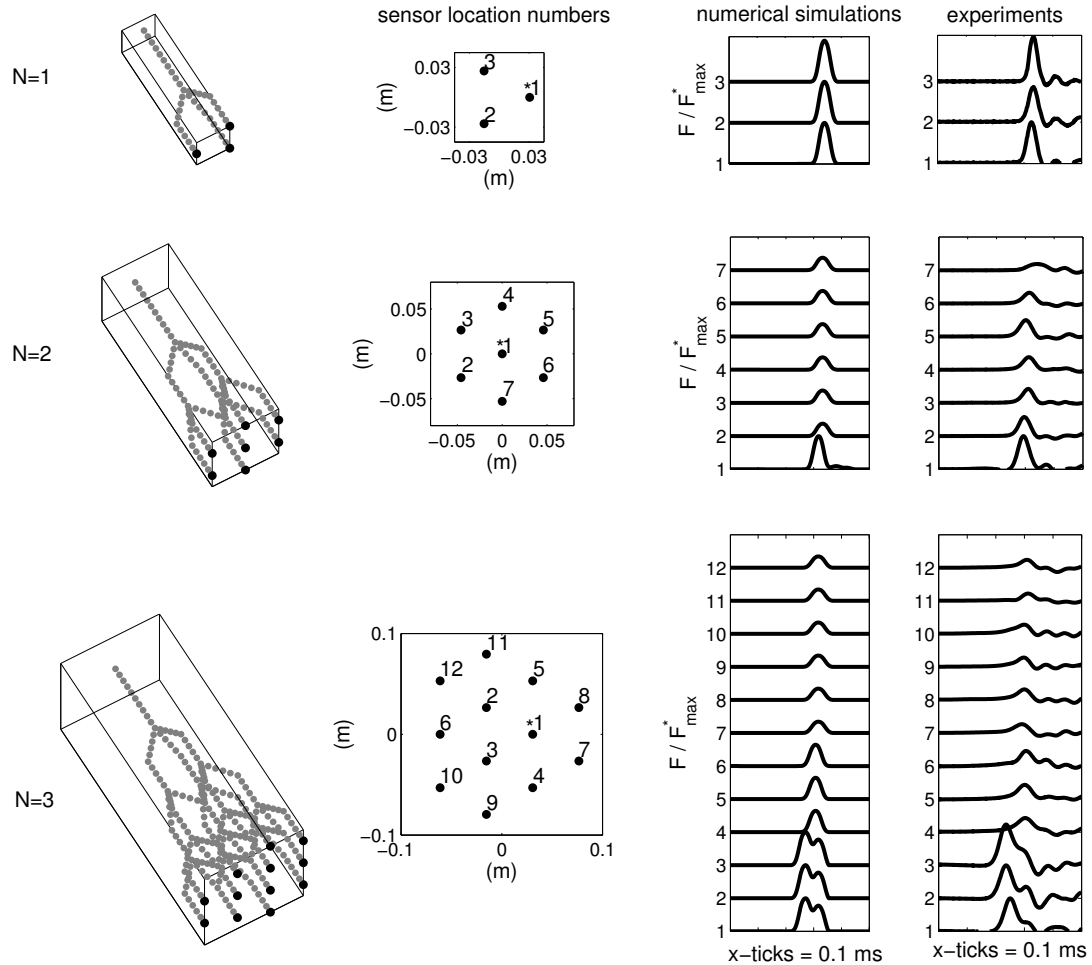


Figure 7.3: Numerical simulations and experimental results of the force profiles at each branch end for the tested $N=1$ through $N=3$ networks. (Left) Schematic diagram of the branch network for each level. The force profiles correspond to particles denoted in black. For each level, the amplitude was normalized by the amplitude of particle*. (Middle) Numerical simulations and (Right) a single experimental test for each of the tested networks ($N=1-3$). The force profiles of each branch end are offset by 1 N for visual clarity. Y-ticks denote 0.5 N and x-ticks denote 0.1 ms

7.3.1 Distribution of Leading Pulse Amplitudes: Effective Network Properties

For the simpler 2-D network previously studied (CH 6), the equal spacing of branch ends easily allowed for an exact description of both the central pulse amplitude with increasing N , and the spatial repartition of leading pulse amplitudes at a given branch level. For the chosen 3D network geometry, however, the branch end spatial distribution is significantly more complex. We follow a similar approach to Sections 6.3.1 and 6.3.2 to derive expressions for F_{middle} and F_r , which are no longer exact, but closely approximate the exact branch end amplitudes obtained by the quasi-particle transmission coefficients.

In the case of N even, $F_{\text{max}} = F_{r=0} = F_{\text{middle}}$. For N even, the F_{middle}/F_i values exactly follow the relation $(T_S\sqrt{T_C T_{M3}})^N$, where F_i is the initial or input pulse amplitude. For N odd, F_{max} occurs at some $r > 0$, and F_{middle} can be obtained from a linear regression of the spatial distribution quasi-particle transmission coefficients $\log F_r$ vs r at each branch level N . As shown in Figure 7.4a, the expression:

$$F_{\text{middle}} = F_i e^{-N/N_0} \quad \text{with} \quad N_0 = \frac{-1}{\log T_S\sqrt{T_C T_{M3}}} \quad (7.5)$$

derived for N even, also fits N odd values quite well.

The spatial repartition of the leading pulses was derived using the expressions $F_{\text{middle}}/F_i = (T_S\sqrt{T_C T_{M3}})^N$ (exact for N even) and $F_{\text{side}}/F_i = (T_S T_C)^N$ (exact for all N), along with the relationship $\xi_{\text{side}} = Nr\sqrt{3}/2$ (exact for N even and a very close approximation for N odd), where r is again defined as varying from 0 to 1 at each branch level N . The resulting expression

$$F_r = F_{\text{middle}} e^{-\xi/\xi_0} \quad \text{with} \quad \xi_0 = \frac{-\sqrt{3}}{2 \log \sqrt{T_{M3}/T_C}} \quad \text{and} \quad \xi = \frac{Nr\sqrt{3}}{2} \quad (7.6)$$

is compared with the quasi-particle transmission coefficients in the inset of Figure 7.4a, for branching levels $N = 2 - 6$.

As the branch angle α increases, the transmitted solitary wave amplitude slightly

increases at splitting junctions, decreases at corners, and slightly increases (decreases) for and 3- (2-) chain merging junctions. The net effect is a decreasing central $\sim T_S^2 T_C T_{M3}$ and edge $\sim T_S T_C$ amplitude transmission with increasing α .

The F_{middle} values for N even experiments were directly obtained from the central branch end ($r = 0$). For N odd, F_{middle} was obtained from a linear regression on the experimental $\log F_r$ vs r data, except for $N = 1$, where F_{middle} had to be directly extrapolated from the theoretical prediction: $F_{\text{middle}}^{N=1} = e^{\log(F_{r=1})+1/\xi_0}$. Figure 7.4b compares the computed F_{middle} from experiments with those from numerical simulations and theoretical predictions. The experimental force amplitudes at each branch end F_r were normalized by the corresponding F_{middle} values and the comparison with numerical simulations and theoretical predictions are shown in Figure 7.4c. The full system response is most clearly seen after normalization of the primary pulse amplitudes by the impacting force F_i , as shown in Figure 7.4d. Here the effects of dissipation in experiments are more evident when compared to the conservative numerical simulations and theoretical predictions. Overall, the agreement between the experiments, numerical simulations, and theoretical predictions are quite good, confirming both the exponential decay of the central F_{middle} amplitude with increasing N as well as the exponential decay in spatial repartition of pulses along r at a given branch level N . Similar to the 2D network, the comparison with quasi-particle predictions is expected to improve with increasing branch length, which allows primary and trailing pulses sufficient time to fully separate. For the $\alpha = 40^\circ$ network, the values $N_0 = 1.8$ and $\xi_0 = 1.9$, suggest that the $N = 2$ granular network already results in a high wave amplitude mitigation.

7.4 Summary of Results

We extended the previous study on of the pulse transmission through a 2D network (Chapter 6), into a fully 3D network geometry. The quasi-particle model was used to define transmission coefficients, T_S , T_C , T_{M3} , and T_{M2} , or pulse splitting, pulse bending, 3-pulse merging, and 2-pulse merging within the described network geometry. We

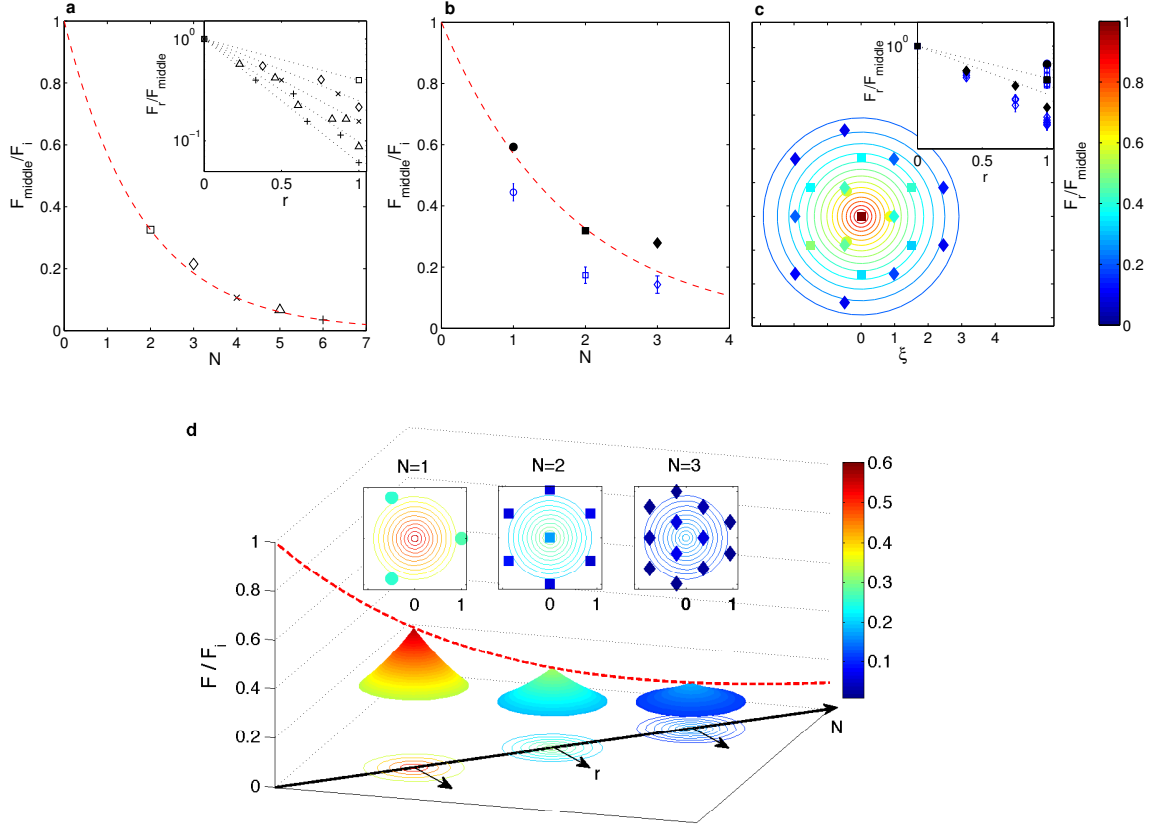


Figure 7.4: Distribution of leading pulse amplitudes. The marker shapes indicate the branch level: $N1$ =circle, $N2$ =square, $N3$ =diamond, $N4$ =cross, $N5$ =triangle, and $N6$ =plus. **(a)** Theoretical distribution of pulse amplitudes. The normalized amplitudes based on quasi-particle transmission coefficients are represented with black marker outlines, and Equation (7.5) is shown in the dashed red lines and dotted black lines in the inset. **(b)** Normalized central pulse amplitude F_{middle}/F_i with increasing branch level N : theory, experiments, and simulations. The dotted red line represents Equation (7.6), the solid black markers indicate numerical simulations, and the blue dots and error bars represent experiments. The error bars for $N = 1$ and 2 represent 2σ , where σ was calculated from the set of 7 initial experimental configurations. The error bars for $N=3$ represent the 95% confidence intervals for the normalized F_{middle} obtained from a linear regression of $\log F_r$ vs r . **(c)** Spatial repartition of leading pulse amplitudes: theory, experiments, and simulations. The colored contour levels of F_r/F_{middle} represent Equation (7.6), and the markers represent the average values from experiments. The inset shows the data before normalization with ξ . The blue markers and error bars represent the mean and standard deviation from experiments, and the solid black markers represent the numerical simulations. **(d)** Total system response. The color bar indicates the transmitted primary pulse amplitudes normalized by the impact force F/F_i . The three insets compare the theoretical predictions, contours, with average values from experiments, markers.

observed excellent agreement between the quasi-particle transmission coefficients and numerical simulations for a range of branching angles α . Additionally, experiments for $N = 1 - 3$ systems sizes with $\alpha = 40^\circ$ were in good agreement with numerical simulations in terms of the relative force profiles at each branch end. We presented descriptions of the leading pulse amplitude distributions, based on the quasi-particle model. Similar to the 2D network, the theoretical predictions lead to an exponential decay of both the central pulse amplitude with increasing system size N , as well as in the distribution of leading pulses with distance from the line of impact at each branch level, and suggest a minimum systems size $N = 2$ for effective wave mitigation. Experiments and numerical simulations confirm the predicted exponential decay in both spatial directions.

Chapter 8

Conclusions & Future Work

8.1 Conclusions

In this thesis, we created engineered granular systems, varying the granular structure, i.e., individual particle size, shape, material property, and location, to study the effects of particle arrangement on the wave propagation. In particular, we focused on the highly nonlinear transient wave propagation through densely packed 2D granular crystals as well as 2D and 3D ordered networks of interconnected particle chains. We performed experiments for variable granular crystal/network geometries and compared the obtained results with the predicted responses from numerical simulations, based on a conservative discrete particle model, and theory, where available.

In Chapters 3 through 5 we studied the stress wave propagation due to a localized impulsive loading for three different 2D particle lattices: square, centered square, and hexagonal granular crystals. In the simplest case of a 2D square packing, we observed a highly directional response, with pulses traveling only along initially excited chains. These traveling waves were observed to possess similar properties to the well-studied 1D solitary waves. The addition of “intruder” particles within the interior spaces of the square array gives way to the centered square lattice geometry. The additional contact points between particles allows for lateral energy redistribution, transforming the system response from quasi-1D to a fully 2D response. For the centered square packing, we showed that systematic variations in the mass and stiffness ratios of the intruders and particles composing the outer square array lead to large variations in

the propagation wave characteristics. We experimentally verified wave front shapes predicted by numerical simulations ranging from a highly directional response, in line with the impact, to a triangular and circular one, and finally to a squared wave front, where a significant portion of the impact energy was redirected away from the line of impact. Studies of the 2D hexagonal crystal allowed for a more rigorous description of the propagation wave structure, compared to other 2D geometries. In this case, we observed a distinct pulse traveling through the particle bed and described the decaying velocity profile along different radial directions from the impact. Additionally, the effects of weak disorder, inevitably present in real granular systems, were investigated for the mentioned granular crystal structures. While variations can arise between experiments on individual contact lattices, the characteristic wave structures inherent to each inter-particle contact lattice remained prominent for the investigated granular crystal geometries.

In Chapters 6 and 7, we focused on the pulse propagation through ordered networks of interconnected granular sphere chains. The network geometry allows for selective placement of the waveguiding chains to control the transmission of acoustic waves, significantly reducing the effective density compared to the tightly packed granular crystals. Additionally, the use of 1D granular chains as the building block for these structures allowed for theoretical predictions of the transmitted pulse amplitudes via the quasi-particle approach. The quasi-particle continuum theory was used to derive transmission coefficients for the pulse splitting, bending, and combining, allowing us to describe the effective acoustic properties of the network structures. For both 2D and 3D granular networks, we observed an exponential decay in the leading pulse amplitudes, both with distance from the impact and in the distribution of leading pulses perpendicular to the line of impact. The rapid amplitude decay exhibited by these granular networks makes them highly attractive for impact mitigation applications. Additionally, we noted similarities between the observed exponential decay in our engineered granular networks and the force transmission through disordered granular media.

Overall, the excellent agreement between experiments, numerical simulations, and

applicable theoretical predictions validates the wave guiding capabilities of these engineered granular crystals and networks and opens a wide range of possibilities for the realization of increasingly complex granular material design.

8.2 Future Directions

In this thesis, we studied several of the simplest 2D granular crystal lattices. The present work is intended as a first step in understanding the fundamental wave characteristics within a general 2D or 3D granular crystal framework. Future experimental and numerical studies on variable contact lattices, incorporating multiple materials and particle geometries, will be helpful to develop a general knowledge of the waves supported by these systems. Additionally, while several theoretical approaches exist for predicting the highly nonlinear wave propagation in ordered 1D granular crystals, there is no analogous theory to predict the highly nonlinear wave properties in higher-dimensional systems. We hope the work presented in this thesis will pave the way for future theoretical efforts to analytically describe the highly nonlinear wave propagation supported by variable 2D (and 3D) granular lattice structures.

The granular crystal and network geometries studied in this thesis are intended to serve as a basis for the design of engineered granular waveguide systems, and future work should be done in order to design optimal application specific structures. In this thesis, we developed means for spatial wave mitigation, in which we validated the ability to methodically alter the propagating wave front pathway and rapidly decrease the leading pulse amplitude. However, more efficient impact attenuation could be achieved by combining this spatial wave mitigation with temporal wave mitigation techniques used in the design of 1D granular protectors. Additionally, future work could be done to engineer these waveguide systems in the opposite sense, engineering the particle to structure to focus instead of disperse acoustic energy.

The focus of the present work was on the highly nonlinear, or uncompressed, response of these granular crystals. However, interesting dynamic properties are also expected in the weakly nonlinear or linear regime. Studying the linearized dynamic

response of 2D and 3D granular crystals will add an additional level of tunability within the 2D and 3D granular framework, and could result in the design of multifunctional engineered structures.

While designing optimal granular arrangements is one future challenge, another will be assembling them in way that the material could be implemented in real applications. In this light, future experimental studies on the effects of a matrix will be needed to determine the composite structure response and develop predictive models. Additionally, to more accurately capture and predict the real system response in numerical simulations, future work should be done to better understand the sources of dissipation and how to appropriately incorporate these effects in the discrete particle framework.

The ability to tune material properties based on the underlying structure of these complex materials relies on the ability to construct highly ordered material systems with minimal imperfections. However, some variability, or measure of defects, is inevitable in real material systems. In this thesis, we studied the effects of weak disorder in the tightly packed 2D granular crystals. A natural extension of this work will be to study the effects of increasing disorder in particle size, shape, material properties, etc., to determine whether a transition regime can be defined, where the granular material essential behaves as a disordered granular media, and no longer retains the engineered or desired predefined response.

Finally, since the granular chain system was perfectly ordered, we could investigate its properties analytically, and relate its property at the microstructure scale (branching angle and particle geometry and material) with its macroscopic acoustic behavior (N_0 and ξ_0). Future studies involving branched systems that incorporate random orientations and chain lengths would help to improve our understanding of the acoustic transmission through disordered force chain networks and identify the main differences with ordered networks. Perhaps an effective chain length and branching angle can be established, based on the level of disorder, which could then be used to describe an effective acoustic behavior of disordered networks using a similar theoretical approach as for the ordered network. Such future studies would help elucidate

the role of disorder in the wave mitigation capabilities of granular media.

Bibliography

- [1] www.mcmaster.com, 2013.
- [2] www.efunda.com, 2013.
- [3] www.matprop.com, 2013.
- [4] <http://objet.com/>, 2013.
- [5] V. F. Nesterenko, *Dynamics of heterogeneous materials*. Springer-Verlag New York, Inc., Jan 2001.
- [6] J. Seto, H. S. Gupta, P. Zaslansky, H. D. Wagner, and P. Fratzl, “Tough lessons from bone: Extreme mechanical anisotropy at the mesoscale,” *Advanced Functional Materials*, vol. 18, no. 13, pp. 1905–1911, 2008.
- [7] G. W. Milton, *The Theory of Composites*. Cambridge University Press, 2002.
- [8] M. Lapine and S. Tretyakov, “Contemporary notes on metamaterials,” *Microwaves, Antennas Propagation, IET*, vol. 1, no. 1, pp. 3–11, 2007.
- [9] J. B. Pendry, “Negative refraction makes a perfect lens,” *Phys. Rev. Lett.*, vol. 85, pp. 3966–3969, Oct 2000.
- [10] J.-H. Lee, J. P. Singer, and E. L. Thomas, “Micro-/nanostructured mechanical metamaterials,” *Advanced Materials*, vol. 24, no. 36, pp. 4782–4810, 2012.
- [11] G. W. Milton and A. V. Cherkaev, “Which elasticity tensors are realizable,” *J. Eng. Mater. Technol.*, vol. 4, pp. 843–493, Oct 1995.

- [12] M. Kadic, T. Buckmann, N. Stenger, M. Thiel, and M. Wegener, “On the practicability of pentamode mechanical metamaterials,” *Applied Physics Letters*, vol. 100, no. 19, p. 191901, 2012.
- [13] R. Lakes, “Foam structures with a negative Poisson’s ratio,” *Science*, vol. 235, no. 4792, pp. 1038–1040, 1987.
- [14] W. Yang, Z.-M. Li, W. Shi, B.-H. Xie, and M.-B. Yang, “Review on auxetic materials,” *Journal of Materials Science*, vol. 39, pp. 3269–3279, 2004.
- [15] T. Jaglinski, D. Kochmann, D. Stone, and R. S. Lakes, “Composite materials with viscoelastic stiffness greater than diamond,” *Science*, vol. 315, no. 5812, pp. 620–622, 2007.
- [16] T. A. Schaedler, A. J. Jacobsen, A. Torrents, A. E. Sorensen, J. Lian, J. R. Greer, L. Valdevit, and W. B. Carter, “Ultralight metallic microlattices,” *Science*, vol. 334, no. 6058, pp. 962–965, 2011.
- [17] J. Shim, C. Perdigou, E. R. Chen, K. Bertoldi, and P. M. Reis, “Buckling-induced encapsulation of structured elastic shells under pressure,” *Proceedings of the National Academy of Sciences*, vol. 109, no. 16, pp. 5978–5983, 2012.
- [18] Z. Liu, X. Zhang, Y. Mao, Y. Y. Zhu, Z. Yang, C. T. Chan, and P. Sheng, “Locally resonant sonic materials,” *Science*, vol. 289, no. 5485, pp. 1734–1736, 2000.
- [19] J. Li and C. T. Chan, “Double-negative acoustic metamaterial,” *Phys. Rev. E*, vol. 70, p. 055602, Nov 2004.
- [20] H. H. Huang and C. T. Sun, “Wave attenuation mechanism in an acoustic metamaterial with negative effective mass density,” *New Journal of Physics*, vol. 11, no. 1, p. 013003, 2009.

- [21] J. Mei, G. Ma, M. Yang, Z. Yang, W. Wen, and P. Sheng, “Dark acoustic metamaterials as super absorbers for low-frequency sound,” *Nat Commun*, vol. 3, p. 756, March 2012.
- [22] B.-I. Popa and S. A. Cummer, “Design and characterization of broadband acoustic composite metamaterials,” *Phys. Rev. B*, vol. 80, p. 174303, Nov 2009.
- [23] S. A. Cummer and D. Schurig, “One path to acoustic cloaking,” *New Journal of Physics*, vol. 9, no. 3, p. 45, 2007.
- [24] L. J. Gibson and M. F. Ashby, *Cellular solids: structure and properties*. Cambridge university press, 1999.
- [25] R. S. Lakes, “High damping composite materials: Effect of structural hierarchy,” *Journal of Composite Materials*, vol. 36, no. 3, pp. 287–297, 2002.
- [26] K. Johnson, *Contact mechanics*. The Press Syndicate of the University of Cambridge, The Pitt Building, Jan 1987.
- [27] P. G. de Gennes, “Granular matter: a tentative view,” *Rev. Mod. Phys.*, vol. 71, pp. S374–S382, Mar 1999.
- [28] H. M. Jaeger, S. R. Nagel, and R. P. Behringer, “Granular solids, liquids, and gases,” *Reviews of Modern Physics*, vol. 68, pp. 1259–1273, 1996.
- [29] V. Tournat and V. Gusev, “Acoustics of unconsolidated model granular media: An overview of recent results and several open problems,” *Acta Acustica united with Acustica*, vol. 96, no. 2, pp. 208–224, 2010.
- [30] V. Nesterenko, “Propagation of nonlinear compression pulses in granular media,” *J. Appl. Mech. Tech. Phys.*, vol. 24, no. 5, pp. 733–743, 1983.
- [31] A. Lazaridi and V. Nesterenko, “Observation of a new type of solitary waves in a one-dimensional granular medium,” *Journal of Applied Mechanics and Technical Physics*, vol. 26, no. 3, pp. 405–408, 1985.

- [32] C. Coste, E. Falcon, and S. Fauve, “Solitary waves in a chain of beads under Hertz contact,” *Phys. Rev. E*, vol. 56, no. 5, pp. 6104–6117, 1997.
- [33] R. MacKay, “Solitary waves in a chain of beads under Hertz contact,” *Physics Letters A*, vol. 251, no. 3, pp. 191–192, 1999.
- [34] A. Chatterjee, “Asymptotic solution for solitary waves in a chain of elastic spheres,” *Phys. Rev. E*, vol. 59, no. 5, pp. 5912–5919, 1999.
- [35] C. Coste and B. Gilles, “On the validity of Hertz contact law for granular material acoustics,” *The European Physical Journal B-Condensed Matter and Complex Systems*, vol. 7, no. 1, pp. 155–168, 1999.
- [36] E. Hinch and S. Saint-Jean, “The fragmentation of a line of balls by an impact,” *Proceedings: Mathematical, Physical and Engineering Sciences*, vol. 455, no. 1989, pp. 3201–3220, 1999.
- [37] S. Sen, M. Manciu, R. S. Sinkovits, and A. J. Hurd, “Nonlinear acoustics in granular assemblies,” *Granular Matter*, vol. 3, pp. 33–39, 2001.
- [38] C. Daraio, V. Nesterenko, E. Herbold, and S. Jin, “Strongly nonlinear waves in a chain of Teflon beads,” *Phys. Rev. E*, vol. 72, p. 016603, Jul 2005.
- [39] C. Daraio, V. Nesterenko, E. Herbold, and S. Jin, “Tunability of solitary wave properties in one-dimensional strongly nonlinear phononic crystals,” *Phys. Rev. E*, vol. 73, p. 026610, Feb 2006.
- [40] V. F. Nesterenko, A. N. Lazaridi, and E. B. Sibiriyakov, “The decay of soliton at the contact of two “acoustic vacuums”,” *Journal of Applied Mechanics and Technical Physics*, vol. 36, no. 2, pp. 166–168, 1995.
- [41] D. Sun and S. Sen, “Nonlinear grain-grain forces and the width of the solitary wave in granular chains: a numerical study,” *Granular Matter*, pp. 1–5, 2013.
- [42] A. Rosas and K. Lindenberg, “Pulse dynamics in a chain of granules with friction,” *Phys. Rev. E*, vol. 68, p. 041304, Oct 2003.

- [43] A. Rosas and K. Lindenberg, “Pulse velocity in a granular chain,” *Phys. Rev. E*, vol. 69, p. 037601, Mar 2004.
- [44] A. Rosas and K. Lindenberg, “Pulse propagation in chains with nonlinear interactions,” *Phys. Rev. E*, vol. 69, p. 016615, Jan 2004.
- [45] U. Harbola, A. Rosas, M. Esposito, and K. Lindenberg, “Pulse propagation in tapered granular chains: An analytic study,” *Phys. Rev. E*, vol. 80, p. 031303, Sep 2009.
- [46] K. Lindenberg, U. Harbola, H. Romero, and A. Rosas, “Pulse propagation in granular chains,” *AIP Conference Proceedings*, vol. 1339, no. 1, pp. 97–110, 2011.
- [47] A. Shukla, M. Sadd, R. Singh, Q. Tai, and S. Vishwanathan, “Role of particle shape and contact profile on the dynamic response of particulate materials,” *Optics and Lasers in Engineering*, vol. 19, no. 1-3, pp. 99–119, 1993.
- [48] D. Ngo, D. Khatri, and C. Daraio, “Highly nonlinear solitary waves in chains of ellipsoidal particles,” *Phys. Rev. E*, vol. 84, p. 026610, Aug 2011.
- [49] D. Khatri, D. Ngo, and C. Daraio, “Highly nonlinear solitary waves in chains of cylindrical particles,” *Granular Matter*, vol. 14, pp. 63–69, 2012.
- [50] D. Ngo, S. Griffiths, D. Khatri, and C. Daraio, “Highly nonlinear solitary waves in chains of hollow spherical particles,” *Granular Matter*, pp. 1–7, 2013.
- [51] I. L. D. Pinto, A. Rosas, A. H. Romero, and K. Lindenberg, “Pulse propagation in a chain of o-rings with and without precompression,” *Phys. Rev. E*, vol. 82, p. 031308, Sep 2010.
- [52] M. A. Porter, C. Daraio, E. B. Herbold, I. Szelengowicz, and P. G. Kevrekidis, “Highly nonlinear solitary waves in periodic dimer granular chains,” *Phys. Rev. E*, vol. 77, p. 015601, Jan 2008.

- [53] M. A. Porter, C. Daraio, I. Szelengowicz, E. B. Herbold, and P. Kevrekidis, “Highly nonlinear solitary waves in heterogeneous periodic granular media,” *Physica D: Nonlinear Phenomena*, vol. 238, no. 6, pp. 666–676, 2009.
- [54] K. R. Jayaprakash, Y. Starosvetsky, and A. F. Vakakis, “New family of solitary waves in granular dimer chains with no precompression,” *Phys. Rev. E*, vol. 83, p. 036606, Mar 2011.
- [55] M. Manciu, S. Sen, and A. Hurd, “Crossing of identical solitary waves in a chain of elastic beads,” *Phys. Rev. E*, vol. 63, p. 016614, Dec 2000.
- [56] F. S. Manciu and S. Sen, “Secondary solitary wave formation in systems with generalized Hertz interactions,” *Phys. Rev. E*, vol. 66, p. 016616, Jul 2002.
- [57] W. Zhen-Ying, W. Shun-Jin, Z. Xiu-Ming, and L. Lei, “Solitary wave interactions in granular media,” *Chinese Physics Letters*, vol. 24, no. 10, p. 2887, 2007.
- [58] E. Ávalos and S. Sen, “How solitary waves collide in discrete granular alignments,” *Phys. Rev. E*, vol. 79, p. 046607, Apr 2009.
- [59] F. Santibanez, R. Munoz, A. Caussarieu, S. Job, and F. Melo, “Experimental evidence of solitary wave interaction in Hertzian chains,” *Phys. Rev. E*, vol. 84, p. 026604, Aug 2011.
- [60] R. Singh, A. Shukla, and H. Zervas, “Explosively generated pulse propagation through particles containing natural cracks,” *Mechanics of Materials*, vol. 23, no. 4, pp. 255–270, 1996.
- [61] S. Job, F. Santibanez, F. Tapia, and F. Melo, “Wave localization in strongly nonlinear Hertzian chains with mass defect,” *Phys. Rev. E*, vol. 80, no. 2, p. 25602, 2009.
- [62] L. Vergara, “Scattering of solitary waves from interfaces in granular media,” *Phys. Rev. Lett.*, vol. 95, p. 108002, Sep 2005.

- [63] V. F. Nesterenko, C. Daraio, E. Herbold, and S. Jin, “Anomalous wave reflection at the interface of two strongly nonlinear granular media,” *Phys. Rev. Lett.*, vol. 95, p. 158702, Oct 2005.
- [64] S. Job, F. Melo, A. Sokolow, and S. Sen, “How Hertzian solitary waves interact with boundaries in a 1d granular medium,” *Phys. Rev. Lett.*, vol. 94, p. 178002, May 2005.
- [65] E. Hascoët, H. Herrmann, and V. Loreto, “Shock propagation in a granular chain,” *Phys. Rev. E*, vol. 59, no. 3, pp. 3202–3206, 1999.
- [66] S. Sen, F. Manciu, and M. Manciu, “Thermalizing an impulse,” *Physica A: Statistical Mechanics and its Applications*, vol. 299, no. 3-4, pp. 551–558, 2001.
- [67] A. Sokolow, E. Bittle, and S. Sen, “Solitary wave train formation in Hertzian chains,” *EPL (Europhysics Letters)*, vol. 77, p. 24002, 2007.
- [68] S. Job, F. Melo, A. Sokolow, and S. Sen, “Solitary wave trains in granular chains: experiments, theory and simulations,” *Granular Matter*, vol. 10, pp. 13–20, 2007.
- [69] E. B. Herbold and V. F. Nesterenko, “Shock wave structure in a strongly nonlinear lattice with viscous dissipation,” *Phys. Rev. E*, vol. 75, p. 021304, Feb 2007.
- [70] M. Remoissenet, *Waves Called Solitons*. Springer, Heidelberg, 1999.
- [71] C. Daraio, V. Nesterenko, E. Herbold, and S. Jin, “Energy trapping and shock disintegration in a composite granular medium,” *Phys. Rev. Lett.*, vol. 96, p. 058002, Feb 2006.
- [72] R. Doney and S. Sen, “Decorated, tapered, and highly nonlinear granular chain,” *Phys. Rev. Lett.*, vol. 97, p. 155502, Oct 2006.

- [73] D. T. Wu, “Conservation principles in solitary impulse propagation through granular chains,” *Physica A: Statistical Mechanics and its Applications*, vol. 315, pp. 194–202, 2002.
- [74] M. Nakagawa, J. Agui, D. Wu, and D. Extramiana, “Impulse dispersion in a tapered granular chain,” *Granular Matter*, vol. 4, no. 4, pp. 167–174, 2003.
- [75] J. Hong, “Universal power-law decay of the impulse energy in granular protectors,” *Phys. Rev. Lett.*, vol. 94, p. 108001, Mar 2005.
- [76] A. Sokolow, J. M. M. Pfannes, R. L. Doney, M. Nakagawa, J. H. Agui, and S. Sen, “Absorption of short duration pulses by small, scalable, tapered granular chains,” *Applied Physics Letters*, vol. 87, no. 25, p. 254104, 2005.
- [77] R. L. Doney and S. Sen, “Impulse absorption by tapered horizontal alignments of elastic spheres,” *Phys. Rev. E*, vol. 72, p. 041304, Oct 2005.
- [78] F. Melo, S. Job, F. Santibanez, and F. Tapia, “Experimental evidence of shock mitigation in a Hertzian tapered chain,” *Phys. Rev. E*, vol. 73, p. 041305, Apr 2006.
- [79] L. Vergara, “Delayed scattering of solitary waves from interfaces in a granular container,” *Phys. Rev. E*, vol. 73, p. 066623, Jun 2006.
- [80] E. B. Herbold and V. F. Nesterenko, “Solitary and shock waves in discrete strongly nonlinear double power-law materials,” *Applied Physics Letters*, vol. 90, no. 26, p. 261902, 2007.
- [81] P. J. Wang, Y. D. Li, J. H. Xia, and C. S. Liu, “Characterization of reflection intermittency in a composite granular chain,” *Phys. Rev. E*, vol. 77, p. 060301, Jun 2008.
- [82] F. Fraternali, M. Porter, and C. Daraio, “Optimal design of composite granular protectors,” *Mechanics of Advanced Materials and Structures*, vol. 17, no. 1, pp. 1–19, 2010.

- [83] J. Hong and A. Xu, “Nondestructive identification of impurities in granular medium,” *Applied Physics Letters*, vol. 81, no. 25, pp. 4868–4870, 2002.
- [84] J. Yang, C. Silvestro, S. N. Sangiorgio, S. L. Borkowski, E. Ebrahimzadeh, L. D. Nardo, and C. Daraio, “Nondestructive evaluation of orthopaedic implant stability in THA using highly nonlinear solitary waves,” *Smart Materials and Structures*, vol. 21, no. 1, p. 012002, 2012.
- [85] J. Yang, S. Sangiorgio, S. Borkowski, C. Silvestro, L. De Nardo, C. Daraio, and E. Ebrahimzadeh, “Site-specific quantification of bone quality using highly nonlinear solitary waves,” *Journal of Biomechanical Engineering*, 2012.
- [86] A. Spadoni and C. Daraio, “Generation and control of sound bullets with a nonlinear acoustic lens,” *Proceedings of the National Academy of Sciences*, vol. 107, no. 16, pp. 7230–7234, 2010.
- [87] J. Yang, S. Dunatunga, and C. Daraio, “Amplitude-dependent attenuation of compressive waves in curved granular crystals constrained by elastic guides,” *Acta Mechanica*, vol. 223, pp. 549–562, 2012.
- [88] J. Yang and C. Daraio, “Frequency- and amplitude-dependent transmission of stress waves in curved one-dimensional granular crystals composed of diatomic particles,” *Experimental Mechanics*, vol. 53, pp. 469–483, 2013.
- [89] D. Khatri, C. Daraio, and P. Rizzo, “Coupling of highly nonlinear waves with linear elastic media,” *SPIE 7292, Sensors and Smart Structures Technologies for Civil, Mechanical, and Aerospace Systems*, pp. 72920P–72920P–9, March 2009.
- [90] M. de Billy, “Experimental study of sound propagation in a chain of spherical beads,” *The Journal of the Acoustical Society of America*, vol. 108, no. 4, pp. 1486–1495, 2000.

- [91] E. Herbold, J. Kim, V. Nesterenko, S. Wang, and C. Daraio, “Pulse propagation in a linear and nonlinear diatomic periodic chain: effects of acoustic frequency band-gap,” *Acta Mechanica*, vol. 205, pp. 85–103, 2009.
- [92] N. Boechler, J. Yang, G. Theocharis, P. G. Kevrekidis, and C. Daraio, “Tunable vibrational band gaps in one-dimensional diatomic granular crystals with three-particle unit cells,” *Journal of Applied Physics*, vol. 109, no. 7, p. 074906, 2011.
- [93] G. Theocharis, N. Boechler, P. G. Kevrekidis, S. Job, M. A. Porter, and C. Daraio, “Intrinsic energy localization through discrete gap breathers in one-dimensional diatomic granular crystals,” *Phys. Rev. E*, vol. 82, p. 056604, Nov 2010.
- [94] N. Boechler, G. Theocharis, and C. Daraio, “Bifurcation-based acoustic switching and rectification,” *Nat Mater*, vol. 10, pp. 665–668, Sep 2011.
- [95] B. Gilles and C. Coste, “Low-frequency behavior of beads constrained on a lattice,” *Phys. Rev. Lett.*, vol. 90, p. 174302, May 2003.
- [96] J. Anfosso and V. Gibiat, “Elastic wave propagation in a three-dimensional periodic granular medium,” *EPL (Europhysics Letters)*, vol. 67, no. 3, p. 376, 2004.
- [97] E. Somfai, J.-N. Roux, J. H. Snoeijer, M. van Hecke, and W. van Saarloos, “Elastic wave propagation in confined granular systems,” *Phys. Rev. E*, vol. 72, p. 021301, Aug 2005.
- [98] C. Coste and B. Gilles, “Sound propagation in a constrained lattice of beads: High-frequency behavior and dispersion relation,” *Phys. Rev. E*, vol. 77, no. 2, p. 21302, 2008.
- [99] O. Mouraille, W. A. Mulder, and S. Luding, “Sound wave acceleration in granular materials,” *Journal of Statistical Mechanics: Theory and Experiment*, vol. 2006, no. 07, p. P07023, 2006.

- [100] O. Mouraille and S. Luding, “Sound wave propagation in weakly polydisperse granular materials,” *Ultrasonics*, vol. 48, pp. 498–505, 2008.
- [101] A. Merkel, V. Tournat, and V. Gusev, “Elastic waves in noncohesive frictionless granular crystals,” *Ultrasonics*, vol. 50, pp. 133–138, Feb 2010.
- [102] A. Merkel, V. Tournat, and V. Gusev, “Experimental evidence of rotational elastic waves in granular phononic crystals,” *Phys. Rev. Lett.*, vol. 107, p. 225502, Nov 2011.
- [103] B. Velický and C. Caroli, “Pressure dependence of the sound velocity in a two-dimensional lattice of Hertz-Mindlin balls: Mean-field description,” *Phys. Rev. E*, vol. 65, p. 021307, Jan 2002.
- [104] M. Abd-Elhady, S. Abd-Elhady, C. Rindt, and A. van Steenhoven, “Force propagation speed in a bed of particles due to an incident particle impact,” *Advanced Powder Technology*, vol. 21, no. 2, pp. 150–164, 2010.
- [105] J. Geng, D. Howell, E. Longhi, R. Behringer, G. Reydellet, L. Vanel, E. Clément, and S. Luding, “Footprints in sand: The response of a granular material to local perturbations,” *Phys. Rev. Lett.*, vol. 87, p. 035506, Jul 2001.
- [106] N. Mueggenburg, H. Jaeger, and S. Nagel, “Stress transmission through three-dimensional ordered granular arrays,” *Phys. Rev. E*, vol. 66, p. 031304, Sep 2002.
- [107] L. Breton, P. Claudin, É. Clément, and J. Zucker, “Stress response function of a two-dimensional ordered packing of frictional beads,” *EPL (Europhysics Letters)*, vol. 60, p. 813, 2002.
- [108] J. Geng, G. Reydellet, E. Clément, and R. Behringer, “Green’s function measurements of force transmission in 2d granular materials,” *Physica D: Nonlinear Phenomena*, vol. 182, no. 3-4, pp. 274–303, 2003.

- [109] H. Rossmannith and A. Shukla, “Photoelastic investigation of dynamic load transfer in granular media,” *Acta Mechanica*, vol. 42, pp. 211–225, 1982.
- [110] A. Shukla and C. Damania, “Experimental investigation of wave velocity and dynamic contact stresses in an assembly of disks,” *Experimental Mechanics*, vol. 27, pp. 268–281, 1987.
- [111] A. Shukla, C. Zhu, and M. Sadd, “Angular dependence of dynamic load transfer due to explosive loading in granular aggregate chains,” *The Journal of Strain Analysis for Engineering Design*, vol. 23, no. 3, pp. 121–127, 1988.
- [112] A. Shukla, “Dynamic photoelastic studies of wave propagation in granular media,” *Optics and Lasers in Engineering*, vol. 14, no. 3, pp. 165–184, 1991.
- [113] M. H. Sadd, Q. Tai, and A. Shukla, “Contact law effects on wave propagation in particulate materials using distinct element modeling,” *International Journal of Non-Linear Mechanics*, vol. 28, no. 2, pp. 251–265, 1993.
- [114] Y. Zhu, A. Shukla, and M. H. Sadd, “The effect of microstructural fabric on dynamic load transfer in two-dimensional assemblies of elliptical particles,” *Journal of the Mechanics and Physics of Solids*, vol. 44, no. 8, pp. 1283–1303, 1996.
- [115] Q. Tai and M. H. Sadd, “A discrete element study of the relationship of fabric to wave propagational behaviours in granular materials,” *International Journal for Numerical and Analytical Methods in Geomechanics*, vol. 21, no. 5, pp. 295–311, 1997.
- [116] A. Leonard, F. Fraternali, and C. Daraio, “Directional wave propagation in a highly nonlinear square packing of spheres,” *Experimental Mechanics*, vol. 53, pp. 327–337, 2013.
- [117] C. Daraio, D. Ngo, V. F. Nesterenko, and F. Fraternali, “Highly nonlinear pulse splitting and recombination in a two-dimensional granular network,” *Phys. Rev. E*, vol. 82, p. 036603, Sep 2010.

- [118] D. Ngo, F. Fraternali, and C. Daraio, “Highly nonlinear solitary wave propagation in y-shaped granular crystals with variable branch angles,” *Phys. Rev. E*, vol. 85, p. 036602, Mar 2012.
- [119] A. Leonard and C. Daraio, “Stress wave anisotropy in centered square highly nonlinear granular systems,” *Phys. Rev. Lett.*, vol. 108, p. 214301, May 2012.
- [120] A. P. Awasthi, K. J. Smith, P. H. Geubelle, and J. Lambros, “Propagation of solitary waves in 2d granular media: A numerical study,” *Mechanics of Materials*, vol. 54, no. 0, pp. 100–112, 2012.
- [121] M. Sadd, J. Gao, and A. Shukla, “Numerical analysis of wave propagation through assemblies of elliptical particles,” *Computers and Geotechnics*, vol. 20, no. 3–4, pp. 323–343, 1997.
- [122] M. H. Sadd, G. Adhikari, and F. Cardoso, “Dem simulation of wave propagation in granular materials,” *Powder Technology*, vol. 109, pp. 222–233, 2000.
- [123] M. Nishida, K. Tanaka, and T. Ishida, “Dem simulation of wave propagation in two-dimensional ordered array of particles,” in *Shock Waves* (K. Hannemann and F. Seiler, eds.), pp. 815–820, Springer Berlin Heidelberg, 2009.
- [124] M. Nishida and Y. Tanaka, “Dem simulations and experiments for projectile impacting two-dimensional particle packings including dissimilar material layers,” *Granular Matter*, vol. 12, pp. 357–368, Jul 2010.
- [125] I. Szelengowicz, P. G. Kevrekidis, and C. Daraio, “Wave propagation in square granular crystals with spherical interstitial intruders,” *Phys. Rev. E*, vol. 86, p. 061306, Dec 2012.
- [126] I. Szelengowicz, M. A. Hasan, Y. Starosvetsky, A. Vakakis, and C. Daraio, “Energy equipartition in two-dimensional granular systems with spherical intruders,” *Phys. Rev. E*, vol. 87, p. 032204, Mar 2013.

- [127] D. Ngo, F. Fraternali, and C. Daraio, “Angular dependence of highly nonlinear pulse splitting in a two-dimensional granular network,” *Proceedings of the ASME 2010 International Mechanical Engineering Congress & Exposition, IMECE2010-39699, Vancouver Canada*, November 2010.
- [128] C. Qiong, Y. Xian-Qing, Z. Xin-Yin, W. Zhen-Hui, and Z. Yue-Min, “Binary collision approximation for solitary waves in a y-shaped granular chain,” *Chinese Physics B*, vol. 22, no. 1, p. 014501, 2013.
- [129] J. Goddard, “Nonlinear elasticity and pressure-dependent wave speeds in granular media,” *Proceedings of the Royal Society of London. Series A, Mathematical and Physical Sciences*, vol. 430, no. 1878, pp. 105–131, 1990.
- [130] L. Ponson, N. Boechler, Y. M. Lai, M. A. Porter, P. G. Kevrekidis, and C. Daraio, “Nonlinear waves in disordered diatomic granular chains,” *Phys. Rev. E*, vol. 82, p. 021301, Aug 2010.
- [131] M. Manjunath, A. P. Awasthi, and P. H. Geubelle, “Wave propagation in random granular chains,” *Phys. Rev. E*, vol. 85, p. 031308, Mar 2012.
- [132] S. Sen and R. Sinkovits, “Sound propagation in impure granular columns,” *Phys. Rev. E*, vol. 54, no. 6, pp. 6857–6865, 1996.
- [133] E. Hascoët and H. Herrmann, “Shocks in non-loaded bead chains with impurities,” *The European Physical Journal B-Condensed Matter and Complex Systems*, vol. 14, no. 1, pp. 183–190, 2000.
- [134] T. Travers, M. Ammi, D. Bideau, A. Gervois, J. C. Messenger, and J. P. Troadec, “Uniaxial compression of 2d packings of cylinders. effects of weak disorder,” *EPL (Europhysics Letters)*, vol. 4, no. 3, p. 329, 1987.
- [135] C. h. Liu, S. R. Nagel, D. A. Schecter, S. N. Coppersmith, S. Majumdar, O. Narayan, and T. A. Witten, “Force fluctuations in bead packs,” *Science*, vol. 269, no. 5223, pp. 513–515, 1995.

- [136] S. N. Coppersmith, C. h. Liu, S. Majumdar, O. Narayan, and T. A. Witten, “Model for force fluctuations in bead packs,” *Phys. Rev. E*, vol. 53, pp. 4673–4685, May 1996.
- [137] F. Radjai, M. Jean, J.-J. Moreau, and S. Roux, “Force distributions in dense two-dimensional granular systems,” *Phys. Rev. Lett.*, vol. 77, pp. 274–277, Jul 1996.
- [138] J. N. Roux, “Contact disorder and nonlinear elasticity of granular packings: A simple model,” *Powders & Grains, Behringer & Jenkins (eds.)*, 1997 Belkema, Rotterdam ISBN 90 5410 884 3.
- [139] D. M. Mueth, H. M. Jaeger, and S. R. Nagel, “Force distribution in a granular medium,” *Phys. Rev. E*, vol. 57, pp. 3164–3169, Mar 1998.
- [140] F. Radjai, S. Roux, and J. J. Moreau, “Contact forces in a granular packing,” *Chaos: An Interdisciplinary Journal of Nonlinear Science*, vol. 9, no. 3, pp. 544–550, 1999.
- [141] D. Howell, R. P. Behringer, and C. Veje, “Stress fluctuations in a 2d granular couette experiment: A continuous transition,” *Phys. Rev. Lett.*, vol. 82, pp. 5241–5244, Jun 1999.
- [142] H. A. Makse, D. L. Johnson, and L. M. Schwartz, “Packing of compressible granular materials,” *Phys. Rev. Lett.*, vol. 84, pp. 4160–4163, May 2000.
- [143] J.-P. Bouchaud, P. Claudin, D. Levine, and M. Otto, “Force chain splitting in granular materials: A mechanism for large-scale pseudo-elastic behaviour,” *The European Physical Journal E*, vol. 4, pp. 451–457, 2001.
- [144] C. Goldenberg and I. Goldhirsch, “Force chains, microelasticity, and macroelasticity,” *Phys. Rev. Lett.*, vol. 89, p. 084302, Aug 2002.

- [145] T. S. Majmudar and R. P. Behringer, “Contact force measurements and stress-induced anisotropy in granular materials,” *Nature*, vol. 435, pp. 1079–1082, Jun 2005.
- [146] D. L. Blair, N. W. Mueggenburg, A. H. Marshall, H. M. Jaeger, and S. R. Nagel, “Force distributions in three-dimensional granular assemblies: Effects of packing order and interparticle friction,” *Phys. Rev. E*, vol. 63, p. 041304, Mar 2001.
- [147] S. G. Bardenhagen and J. U. Brackbill, “Dynamic stress bridging in granular material,” *Journal of Applied Physics*, vol. 83, pp. 5732–5740, Jun 1998.
- [148] E. T. Owens and K. E. Daniels, “Sound propagation and force chains in granular materials,” *Eur. Phys. Lett.*, vol. 94, p. 54005, 2011.
- [149] K. Roessig, J. Foster, and S. Bardenhagen, “Dynamic stress chain formation in a two-dimensional particle bed,” *Experimental Mechanics*, vol. 42, pp. 329–337, 2002.
- [150] F. Bourrier, F. Nicot, and F. Darve, “Physical processes within a 2d granular layer during an impact,” *Granular Matter*, vol. 10, pp. 415–437, 2008.
- [151] L. Kondic, X. Fang, W. Losert, C. S. O’Hern, and R. P. Behringer, “Microstructure evolution during impact on granular matter,” *Phys. Rev. E*, vol. 85, p. 011305, Jan 2012.
- [152] D. S. Bassett, E. T. Owens, K. E. Daniels, and M. A. Porter, “Influence of network topology on sound propagation in granular materials,” *Phys. Rev. E*, vol. 86, p. 041306, Oct 2012.
- [153] C.-h. Liu and S. R. Nagel, “Sound in sand,” *Phys. Rev. Lett.*, vol. 68, pp. 2301–2304, Apr 1992.
- [154] C.-h. Liu and S. R. Nagel, “Sound in a granular material: Disorder and nonlinearity,” *Phys. Rev. B*, vol. 48, pp. 15646–15650, Dec 1993.

- [155] R. Sinkovits and S. Sen, “Nonlinear dynamics in granular columns,” *Phys. Rev. Lett.*, vol. 74, no. 14, pp. 2686–2689, 1995.
- [156] H. A. Makse, N. Gland, D. L. Johnson, and L. M. Schwartz, “Why effective medium theory fails in granular materials,” *Phys. Rev. Lett.*, vol. 83, pp. 5070–5073, Dec 1999.
- [157] X. Jia, C. Caroli, and B. Velicky, “Ultrasound propagation in externally stressed granular media,” *Phys. Rev. Lett.*, vol. 82, pp. 1863–1866, Mar 1999.
- [158] X. Jia, “Codalike multiple scattering of elastic waves in dense granular media,” *Phys. Rev. Lett.*, vol. 93, p. 154303, 2004.
- [159] V. Tournat, V. Zaitsev, V. Gusev, V. Nazarov, P. Béquin, and B. Castagnède, “Probing weak forces in granular media through nonlinear dynamic dilatancy: Clapping contacts and polarization anisotropy,” *Phys. Rev. Lett.*, vol. 92, p. 085502, Feb 2004.
- [160] V. Tournat and V. E. Gusev, “Nonlinear effects for coda-type elastic waves in stressed granular media,” *Phys. Rev. E*, vol. 80, p. 011306, Jul 2009.
- [161] M. J. Puttock and E. G. Thwaite, *Elastic compression of spheres and cylinders at point and line contact*. Melbourne, Australia: Commonwealth Scientific and Industrial Research Organization, 1969.
- [162] P. A. Cundall and O. D. L. Strack, “A discrete numerical model for granular assemblies,” *Geotechnique*, vol. 29, pp. 47–65, 1979.
- [163] S. Sen, J. Hong, J. Bang, E. Avalos, and R. Doney, “Solitary waves in the granular chain,” *Physics Reports*, vol. 462, no. 2, pp. 21–66, 2008.
- [164] J. Hong and A. Xu, “Effects of gravity and nonlinearity on the waves in the granular chain,” *Phys. Rev. E*, vol. 63, p. 061310, May 2001.
- [165] R. D. Mindlin, “Compliance of elastic bodies in contact,” *J. of Appl. Mech.*, vol. 71, pp. 259–268, Sep 1949.

- [166] R. D. Mindlin and H. Deresiewicz, “Elastic spheres in contact under varying oblique forces,” *J. of Appl. Mech.*, vol. 75, pp. 327–344, Sep 1953.
- [167] O. R. Walton and R. L. Braun, “Viscosity, granular-temperature, and stress calculations for shearing assemblies of inelastic, frictional disks,” *Journal of Rheology*, vol. 30, no. 5, pp. 949–980, 1986.
- [168] V. Tournat, V. E. Gusev, V. Y. Zaitsev, and B. Castagnède, “Acoustic second-harmonic generation with shear to longitudinal mode conversion in granular media,” *EPL (Europhysics Letters)*, vol. 66, no. 6, p. 798, 2004.
- [169] A. Rosas, A. Romero, V. Nesterenko, and K. Lindenberg, “Observation of two-wave structure in strongly nonlinear dissipative granular chains,” *Phys. Rev. Lett.*, vol. 98, p. 164301, Apr 2007.
- [170] R. Carretero-González, D. Khatri, M. Porter, P. Kevrekidis, and C. Daraio, “Dissipative solitary waves in granular crystals,” *Phys. Rev. Lett.*, vol. 102, p. 024102, Jan 2009.
- [171] E. B. Herbold and V. F. Nesterenko, “The role of dissipation on wave shape and attenuation in granular chains,” *Physics Procedia*, vol. 3, no. 1, pp. 465 – 471, 2010.
- [172] L. Vergara, “Model for dissipative highly nonlinear waves in dry granular systems,” *Phys. Rev. Lett.*, vol. 104, p. 118001, Mar 2010.
- [173] Y. Zhu, F. Sienkiewicz, A. Shukla, and M. Sadd, “Propagation of explosive pulses in assemblies of disks and spheres,” *Journal of Engineering Mechanics*, vol. 123, no. 10, pp. 1050–1059, 1997.
- [174] M. Gonzalez, J. Yang, C. Daraio, and M. Ortiz, “Mesoscopic approach to granular crystal dynamics,” *Phys. Rev. E*, vol. 85, p. 016604, Jan 2012.

- [175] C. Thornton, “Coefficient of restitution for collinear collisions of elastic-perfectly plastic spheres,” *Journal of Applied Mechanics*, vol. 6, no. 2, pp. 383–386, 1997.
- [176] E. Wang, T. On, and J. Lambros, “An experimental study of the dynamic elastoplastic contact behavior of dimer metallic granules,” *Experimental Mechanics*, pp. 1–10, 2012.
- [177] K. Chase and W. Greenwood, “Design issues in mechanical tolerance analysis,” *Manufacturing Review, ASME*, vol. 1, no. 1, pp. 50–59, 1988.
- [178] http://lammps.sandia.gov/doc/pair_gran.html, 2013.
- [179] S. Plimpton, “Fast parallel algorithms for short-range molecular-dynamics,” *Journal of Computational Physics*, vol. 117, no. 1, pp. 1–19, 1995.
- [180] A. Leonard, C. Daraio, A. Awasthi, and P. Geubelle, “Effects of weak disorder on stress-wave anisotropy in centered square nonlinear granular crystals,” *Phys. Rev. E*, vol. 86, p. 031305, Sep 2012.

Appendix A

TCA Model (and Corresponding Numerical Study)

Ternary Collision Approximation

The ternary collision approximation was derived by collaborators Christopher Chong and Panos Kevrekidis at the Department of Mathematics and Statistics, University of Massachusetts, Amherst, MA 01003-4515, USA.

A.1 Model

We consider an ordered homogeneous lattice of uncompressed spherical beads arranged in a hexagonal configuration, neglecting, at least for the purposes of considerations herein, dissipative effects. The Hamiltonian of such a system has the form,

$$H = \sum_{m,n} \frac{1}{2} M p_{m,n}^2 + V(|de_1 + q_{m+2,n} - q_{m,n}|) + V(|de_2 + q_{m+1,n+1} - q_{m,n}|) + V(|de_3 + q_{m+1,n-1} - q_{m,n}|) \quad (\text{A.1})$$

where $q_{m,n} \in \mathbb{R}^2$ is the displacement of the $\{m, n\}$ bead from its initial position, d is the bead diameter, M is the bead mass, $e_1 = [2, 0]^T$, $e_2 = [1, \sqrt{3}]^T$, $e_3 = [1, -\sqrt{3}]^T$

and

$$V(r) = A \frac{2}{5} [d - r]_+^{5/2} \quad (\text{A.2})$$

where A is a material parameter depending on the elastic properties of the material and the geometric characteristics of the beads [5], and the bracket is defined by $[r]_+ = \max(0, r)$. All parameters can be rescaled to unity using the transformation,

$$\tilde{q}_{m,n} = d q_{m,n}, \quad \tilde{t} = \sqrt{\frac{M}{A d^{1/2}}} t \quad (\text{A.3})$$

where the variables with the tilde represent the solutions in the physical scaling (i.e., the dimensional ones). We define $q_{m,n} = [x_{m,n}, y_{m,n}]^T$ and $\dot{q}_{m,n} = p_{m,n} = [u_{m,n}, v_{m,n}]^T$. In these variables, the equations of motion have the form,

$$\left. \begin{aligned} \dot{x}_{m,n} &= u_{m,n} \\ \dot{y}_{m,n} &= v_{m,n} \\ \dot{u}_{m,n} &= \frac{V'(r_1) r_1^x}{r_1} + \frac{V'(r_2) r_2^x}{r_2} - \frac{V'(r_3) r_3^x}{r_3} - \frac{V'(r_4) r_4^x}{r_4} - \frac{V'(r_5) r_5^x}{r_5} + \frac{V'(r_6) r_6^x}{r_6} \\ \dot{v}_{m,n} &= \frac{V'(r_1) r_1^y}{r_1} + \frac{V'(r_2) r_2^y}{r_2} - \frac{V'(r_3) r_3^y}{r_3} - \frac{V'(r_4) r_4^y}{r_4} - \frac{V'(r_5) r_5^y}{r_5} + \frac{V'(r_6) r_6^y}{r_6} \end{aligned} \right\} \quad (\text{A.4})$$

where $r_j = \sqrt{(r_j^x)^2 + (r_j^y)^2}$ for $j = 1..6$ and

$$\begin{aligned} r_1^x &= \cos(0) + x_{m+2,n} - x_{m,n} & r_1^y &= \sin(0) + y_{m+2,n} - y_{m,n} \\ r_2^x &= \cos(\pi/3) + x_{m+1,n+1} - x_{m,n} & r_2^y &= \sin(\pi/3) + y_{m+1,n+1} - y_{m,n} \\ r_3^x &= \cos(-\pi/3) - x_{m-1,n+1} + x_{m,n} & r_3^y &= \sin(-\pi/3) - y_{m-1,n+1} + y_{m,n} \\ r_4^x &= \cos(0) - x_{m-2,n} + x_{m,n} & r_4^y &= \sin(0) - y_{m-2,n} + y_{m,n} \\ r_5^x &= \cos(\pi/3) - x_{m-1,n-1} + x_{m,n} & r_5^y &= \sin(\pi/3) - y_{m-1,n-1} + y_{m,n} \\ r_6^x &= \cos(-\pi/3) + x_{m+1,n-1} - x_{m,n} & r_6^y &= \sin(-\pi/3) + y_{m+1,n-1} - y_{m,n} \end{aligned}$$

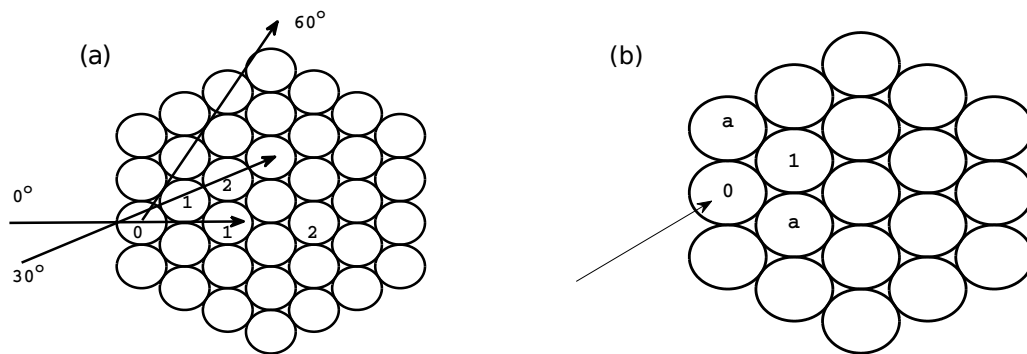


Figure A.1: (a) Orientation of the hexagonal lattice and possible striking and observation angles. The numeric labels correspond to the counting conventions used along the respective observation angles. (b) Labeling convention for the ternary collision approximation

A.2 Ternary Collision Approximation: A Theoretical Approach for 30° Angle of Observation

To help reduce the complexity of the system we consider a setting which is amenable to a semi-analytical description. More specifically, we turn to an analog of the BCA that has been developed for 1D chains [42–46]. We first assume that the beads travel approximately along fixed angles upon impact, based on symmetry considerations. From a theoretical point of view, it is more straightforward to develop the theory for a striking and observation angle of 30° since the pattern does not alternate along this line of observation, in contrast to what is the case for a 0° striking, see Fig. A.1. Considering the time scale where only the beads adjacent to the struck bead are affected results in a so-called ternary collision approximation (TCA). Actually, there are four beads involved in the distribution of the energy at each collisional step, yet we use the symmetry to reduce the number of degrees of freedom to three. In the renormalized system, we have the following TCA for the system of the right panel of

Fig. A.1,

$$\begin{aligned}\ddot{x}_0 &= -[x_0 - x_1]_+^{3/2} - 2 \cos(\theta)[\cos(\theta)x_0 - x_a]_+^{3/2} \\ \ddot{x}_1 &= [x_0 - x_1]_+^{3/2} \\ \ddot{x}_a &= [\cos(\theta)x_0 - x_a]_+^{3/2}\end{aligned}$$

where x_0 is the displacement along the impact direction, x_1 is the displacement along that same direction of the bead adjacent to the impacted bead, and x_a is the displacement of the bead adjacent to the impacted bead at the angle θ . By symmetry, the bead adjacent along the $-\theta$ line will have the same contribution as the x_a bead. Now define $z = x_0 - x_1$ and $y = \cos(\theta)x_0 - x_a$. We have then

$$\left. \begin{aligned}\ddot{z} &= -2[z]_+^{3/2} - [y]_+^{3/2} \\ \ddot{y} &= -[z]_+^{3/2}/2 - 3[y]_+^{3/2}/2\end{aligned} \right\}, \quad (\text{A.5})$$

where we used $\theta = \pi/3$, which corresponds to a hexagonal packing. Although System (A.5) is remarkably simpler than the original System (A.4), it only lends itself to an exact (analytically obtainable) solution in the case where $y(t) = \omega z(t)$, where $\omega \in \mathbb{R}$. However, note that this prescription requires also that the initial conditions satisfy the same scaling. The definition of z and y necessitate (from the corresponding initial conditions) that $\omega = 1/2$. However, using the above ansatz in System (A.5) yields $\ddot{z} = -(2 + \omega^{3/2})[z]_+^{3/2}$, as well as the ‘‘compatibility condition’’ $2 + \omega^{3/2} = (1/2 + 3/2\omega^{3/2})/\omega$, whose sole real solution is $\omega \approx 0.382$. From the above, it is clear that the compatible solution is close to (although not exactly) satisfying the initial conditions. In that light, we will also use for comparison the exact analytical solution of the form:

$$t = {}_2F_1\left(\left[\frac{2}{5}, \frac{1}{2}\right], \left[\frac{7}{5}\right], \frac{2\sqrt{2 + \omega^{3/2}}z^{5/2}}{5E}\right) \frac{z}{\sqrt{2E}}, \quad (\text{A.6})$$

where E in the relevant hypergeometric function expression stands for the constant ‘‘energy’’ of the oscillation associated with $z(t)$ and can be computed as $E = v^2/2$,

where v is the initial velocity of the bead x_0 .

As explained in [46], the main purpose of the BCA is to offer an approximation of the velocity of the traveling wave that propagates through the chain. In order to compute this “pulse velocity” one needs to define the time T_n the pulse resides on bead n . Let $t = 0$ be the time when the velocities of beads $n - 1$ and n become equal. Then T_n is the time when the velocities of beads n and $n + 1$ become equal and the pulse velocity observed at the n th bead is $c_n = 1/T_n$.

In order to approximate the residence time T_n , the BCA combines two points of view. First, it is assumed that the interaction is not instantaneous, such that the velocity of the impacted bead will gradually decrease. However, the BCA is only valid if two beads are involved in the dynamics, which is clearly not the case over the entire residence time T_n . Thus, strictly in terms of the BCA, it is not clear at all how to initialize the next step in the iteration. To circumvent this issue, it is supposed that the interaction is instantaneous such that the conservation of kinetic energy and momentum can be used to compute the velocity that bead n will emerge with after the collision with bead $n - 1$. For example, for a heterogeneous 1D chain, these conservations yield $V_n = 2V_{n-1}/(1 + m_n/m_{n-1})$, where m_n is the mass of bead n [46]. Applying this relationship recursively yields

$$V_n = V_0 \prod_{j=1}^n \frac{2}{1 + m_j/m_{j-1}}. \quad (\text{A.7})$$

Thus, the reduced equations in the BCA setting at the n th step are initialized with $z(0) = 0, \dot{z}(0) = V_n$. Although it appears somewhat awkward to adopt these two viewpoints in order to make the approximation work, the results in 1D chains have been surprisingly good [42–46]. For this reason we carry out a similar procedure to compute the pulse velocity of the traveling wave in the hexagonal lattice.

Due to the complexity of the hexagonal system there is no clear way to obtain an analog of relationship (A.7) using conservation of kinetic energy and momentum. However, in both the 1D BCA and 2D TCA setting, we can compute the time it takes for the initially impacted bead to obtain a velocity equal to its adjacent partner. For

a homogeneous 1D chain, the BCA predicts this to occur for a velocity equal to 50% of the initial velocity. Thus, to understand what contribution the additional beads in the hexagonal configuration will absorb, we use the reduced equations (A.5) to compute when the velocities of beads 0 and 1 are equal (see Fig. A.1 for the labeling convention). The ratio of the velocity at this time compared to the 1D case is one way to quantify the fraction of momentum that is absorbed by the additional beads. Call this value c . For example, suppose the velocity at the time of intersection was predicted to be 0.45 in the TCA and 0.5 in the BCA. Then $c = 0.9$, since the bead only reached 90% of the value it would have in the absence of the additional beads. If in addition, we assume that this ratio remains constant as the traveling structure propagates through the lattice, we expect that bead n emerges with the velocity $V_n = cV_{n-1}$ after collision with bead $n - 1$. Applying this relationship recursively yields,

$$V_n = V_0 c^n, \quad (\text{A.8})$$

where V_0 is the impact velocity. Equation (A.8) will now play the role of (A.7) for the hexagonal system. In the rescaled system we found $c \approx 0.8452$.

Given the repetition of the fundamental building block of the right panel of Fig. A.1, we now simply solve the TCA System (A.5) with initial values defined through (A.8) and compute the intersection time. Doing this for several bead locations yields a discrete set of approximations for the pulse velocity observed at those bead locations. See the left panel of Fig. A.2 for an example with $V_0 = 0.1$. There, it can be seen that such an approximation of this average pulse velocity favorably compares with the full numerical results for the hexagonal lattice.

To amend the TCA to a 0° strike (but still observing along the 30° line) we need to understand how the energy is transferred among the first two beads that are in contact with the impact bead (see Fig. A.1). Due to symmetry considerations, it is reasonable to conjecture that the velocity contribution along the 30° (resp. -30°) will be half of the impact velocity. This would be the case if kinetic energy and momentum were conserved. This relation was observed to be fairly accurate (see the right panel

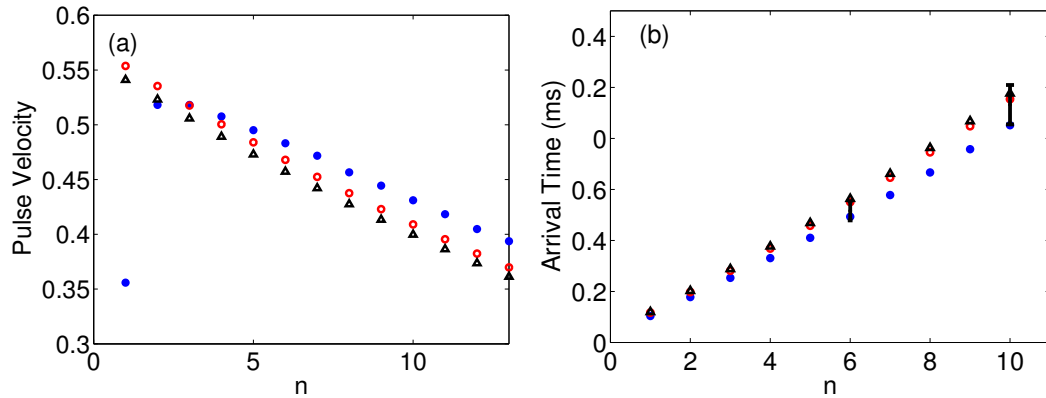


Figure A.2: (a) Observed pulse velocity of the propagating structure in the ideal parameter case at various bead numbers n for a 30° strike and 30° observation angle. The pulse velocity is defined as $c_n = 1/T_n$ where T_n is the n th residence time. The blue dots represent the calculated time based on numerical simulations and the red circles are the prediction based on the TCA. The black triangles denote the exact analytical solution to the TCA system (which, however, is only approximate). The initial strike velocity was $V_0 = 0.1$. (b) The arrival time of the pulse for the experimental parameter values at a 0° strike and 30° observation angle with $V_0 = 0.4$ m/s. The blue dots represent numerical simulations, the red circles are the TCA, the black triangles denote the exact analytical solution to the TCA, and the points with error bars at $n = 6$ and $n = 10$ are the experimental values.

of Fig. A.4). At the 0° strike and 30° observation angle we have experimental data available for comparison, see the right panel of Fig. A.2. Due to the limited number of sensors available, we simply present the arrival time data (which is the sum of the relevant residence times). We should also note that the experiments use the arrival time at the first sensor position in Fig. 5.1 to define $t = 0$. Thus, in order to compare the experimental values to the TCA and numerical simulations we estimate the arrival time at the first sensor using the numerical simulation.

A.3 Numerical Study: Velocity Decay Rate for Variable Striking/Observation Angle Combinations

The TCA, although simple enough to afford analytical approximations, ignores the (weak) dependence of the decay rate c on V_0 and is restricted to an observation angle of 30° . We wish to have a more accurate and robust description of the velocity decay rate and thus we now turn to a (strictly) numerical study of other combinations of striking/observation angles.

A.3.1 30° Strike:

In panel (a) of Fig. A.3, the magnitude of the velocity of each bead along the 30° line is shown against time. Notice how the maximum velocity obtained for each bead decreases as we move further from the impact point, as expected. We fit these maximum points with a function of the form $V_1 c^{n-1}$ where c is a decay parameter that will now depend on the initial strike velocity V_0 (in contrast to the situation above which had c independent of V_0). We start the fit at V_1 since the initial impact will only have a velocity component, and thus the dynamics of the collision of the $n = 0$ and $n = 1$ bead are inherently different than the dynamics of the n and $n + 1$ beads for $n > 0$. In the latter case, the bead will have a velocity and position component.

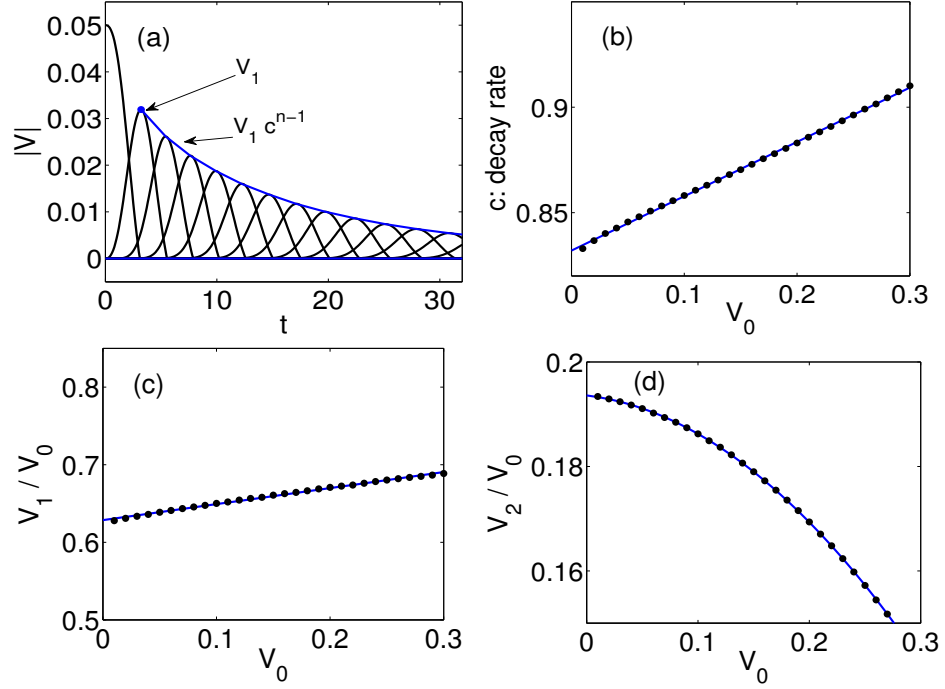


Figure A.3: Illustration of the procedure to obtain the scaling law for the decay of the velocity profile. This example is for strike and observation on the 30° line. (a) Magnitude of velocity of beads 0 – 12 versus time in the ideal parameter case with $V_0 = 0.05$. The maxima are fit with a function of the form $V_1 c^{n-1}$, where V_1 is the maximum velocity of the first bead (labeled in the plot). This process is repeated for several values of V_0 to obtain a sequence of decay rates $c(V_0)$. (b) The sequence of decay rates $c(V_0)$ are fairly accurately fit with a linear function (see the text). (c) The relationship between V_0 and V_1 is computed, and can be either linear (like in this case) or quadratic. Finally, putting these relationships together yields a formula for the maximum velocity at a given bead, see, e.g., Eq. (A.9). (d) For a 0° observation, the fitting begins at bead 2, where the relationship between the initial striking velocity V_0 and V_2 is quadratic.

In panel (b) of Fig. A.3 we fit the decay rates $c = c(V_0)$ with a linear function $mV_0 + b$ with two free parameters m, b . We found that $m \approx 0.257$ and $b \approx 0.832$. In panel (c) of Fig. A.3 we obtain the relationship between V_0 and V_1 , which has the form $V_1 = \alpha V_0^2 + \beta V_0$. We found $\alpha \approx 0.206$ and $\beta \approx 0.629$, such that the decay between V_0 and V_1 is greater than that between V_n and V_{n+1} for $n > 0$. We have then that,

$$V_n = V_0 (\alpha V_0 + \beta)(mV_0 + b)^{n-1}, \quad n > 0 \quad (\text{A.9})$$

where V_n is maximum velocity of the bead lying n beads away from the strike point on the 30° line. Clearly this description of the velocity decay is more accurate than (A.8) since the dependence on the initial impact velocity is taken into account. Nevertheless, we still observe that a power-law decay of the maximum velocity of each bead provides an accurate description of the dynamics along the 30° observation angle in the hexagonal chain.

When observing along the zero degree line it turns out that the fitting is more accurate when starting at bead 2, see Fig. A.1 for the labeling convention. Panel (a) of Fig. A.4 shows a relevant example where the velocity fitting starts at bead 2, but for a 0° strike (which is analyzed in Sec. A.3.2). Since the relationship between V_1 and V_0 was linear, it is natural to suppose that the relationship between V_2 and V_0 is quadratic, i.e., $V_2 \approx \alpha V_0^2 + \beta V_0 + \gamma$ (see panel (d) of Fig. A.3, for example). We have then that,

$$V_n = V_0 (\alpha V_0^2 + \beta V_0 + \gamma)(mV_0 + b)^{n-2}, \quad n > 1 \quad (\text{A.10})$$

where V_n is the magnitude of the maximum velocity of the n th bead from the strike point on the 0° line. Our fitting yielded $m \approx .3039$, $b \approx .8756$ and $\alpha \approx -0.4788$, $\beta \approx -0.0256$, $\gamma \approx 0.1936$.

A.3.2 0° Strike:

Finally, we carry out the procedure for the case of striking at a 0° angle. As mentioned above for a zero degree observation, the first bead behaves somewhat differently (see

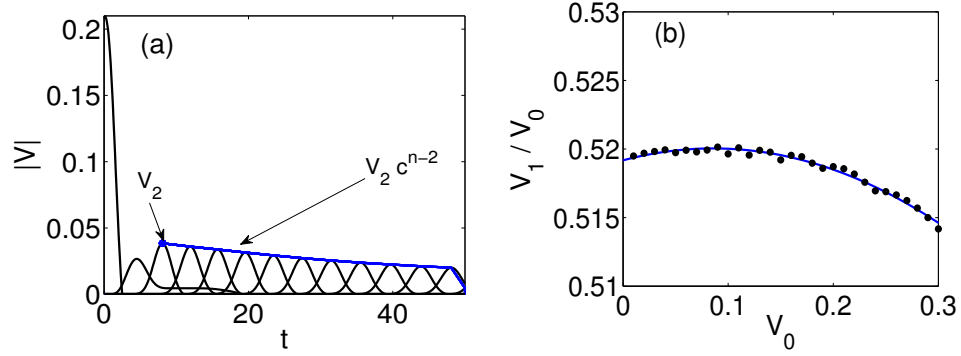


Figure A.4: (a) magnitude of the velocity of beads 0 – 12 along the 0° line upon being struck at a 0° angle. In this case, the fitting is more accurate starting at the second peak V_2 . (b) The relationship between the initial striking velocity V_0 and V_1 for a 0° strike and 30° observation is quadratic. For this particular case, we see that $V_1 \approx V_0/2$.

panel (a) of Fig. A.4), and therefore we start the fitting again at bead 2. We found that our scaling relations continue to be valid for a 0° strike, but now with $m \approx 0.1766$, $b \approx 0.8878$ and $\alpha \approx -0.2643$, $\beta \approx -0.0969$, $\gamma \approx .2152$. The optimal scaling along the 0° observation angle has the same form as (A.10).

When observing at a 30° angle, the formula that yielded the best fit had the form,

$$V_n = V_0 (\alpha V_0^2 + \beta V_0 + \gamma)(mV_0 + b)^{n-1}, \quad n > 0 \quad (\text{A.11})$$

with $m \approx 0.1484$, $b \approx 0.8393$ and $\alpha \approx -0.1182$, $\beta \approx 0.0203$, $\gamma \approx 0.5192$. However, for the range of initial velocities used, the relationship between V_1 and V_0 is approximately $V_1 = V_0/2$ (see panel (b) of Fig. A.4) which yields the simplified formula,

$$V_n = \frac{V_0}{2}(mV_0 + b)^{n-1}, \quad n > 0. \quad (\text{A.12})$$

Note, in order to obtain the scaling law for arbitrary parameter values, one simply replaces each occurrence of V with $V\sqrt{M/A}/d^{5/4}$.